



HAL
open science

Stellar chemical clocks in the Gaia era

Anastasia Titarenko

► **To cite this version:**

Anastasia Titarenko. Stellar chemical clocks in the Gaia era. Solar and Stellar Astrophysics [astro-ph.SR]. COMUE Université Côte d'Azur (2015 - 2019), 2018. English. NNT: 2018AZUR4065. tel-01923867

HAL Id: tel-01923867

<https://theses.hal.science/tel-01923867>

Submitted on 15 Nov 2018

HAL is a multi-disciplinary open access archive for the deposit and dissemination of scientific research documents, whether they are published or not. The documents may come from teaching and research institutions in France or abroad, or from public or private research centers.

L'archive ouverte pluridisciplinaire **HAL**, est destinée au dépôt et à la diffusion de documents scientifiques de niveau recherche, publiés ou non, émanant des établissements d'enseignement et de recherche français ou étrangers, des laboratoires publics ou privés.



THÈSE DE DOCTORAT

INDICATEURS CHIMIQUES D'ÂGE STELLAIRE À L'ÈRE DE GAIA

Anastasia TITARENKO

Laboratoire J-L. Lagrange - Observatoire de la Côte d'Azur

Présentée en vue de l'obtention du grade de docteur
en Sciences de la Planète et de l'Univers
de l'Université Côte d'Azur

Thèse dirigée par: Alejandra RECIO-BLANCO

Soutenue le: 21 Septembre 2018

M.	Carlos ABIA	Professeur	Rapporteur
Mme.	Elisa DELGADO MENA	Chercheur	Rapporteur
M.	Mathias SCHULTHEIS	Astronome	Président, Examineur
Mme.	Alejandra RECIO-BLANCO	Directeur de Recherches	Directeur de thèse

INDICATEURS CHIMIQUES D'ÂGE STELLAIRE

À L'ÈRE DE GAIA

Jury

Président du jury et Examineur:

Mathias SCHULTHEIS Astronome Observatoire de la Côte d'Azur

Rapporteurs:

Carlos ABIA Professeur Université de Granada

Elisa DELGADO MENA Chercheur Centre Astrophysique de l'Université de Porto

Résumé

Les étoiles enregistrent le passé dans leurs âges, leurs compositions chimiques et leur cinématique. Elles peuvent fournir des contraintes détaillées sur les premières époques de la formation des galaxies, jusqu'aux redshifts supérieurs à deux (un recul d'environ 10 milliards d'années). En particulier, les âges stellaires sont essentiels pour la compréhension de l'histoire de la Voie Lactée et pour la comparaison avec les modèles d'évolution galactique.

L'avènement de la mission spatiale Gaia ouvre la voie à l'estimation de l'âge pour de grands échantillons d'étoiles. En particulier, les méthodes basées sur l'ajustement d'isochrones peuvent être utilisées. En plus, les distances précises mesurées par Gaia permettent de développer les estimateurs d'âge indirects basés sur l'horloge d'évolution de la population stellaire. En fait, les schémas d'abondance chimie, imprimés sur les atmosphères stellaires, représentent les conditions du gaz au moment de la formation des étoiles à des redshifts supérieurs à deux. Les produits d'évolution chimie de différents canaux nucléosynthétiques peuvent donc fournir une approximation temporelle, qui, après l'étalonnage, peut être utilisé comme un estimateur d'âge.

Cette thèse est centrée sur l'utilisation d'horloge chimie particulière: l'abondance $[Y/Mg]$. À cette fin, les premières données astrométriques de la mission Gaia ont été combinées avec des données spectroscopiques à haute résolution du catalogue AMBRE HARPS. Tout d'abord, l'identification des objets d'AMBRE a été améliorée grâce à la correspondance avec le catalogue 2MASS et la Gaia DR1. Au total, 6776 étoiles ont été identifiées.

Deuxièmement, afin d'obtenir des estimations précises du rapport d'abondance $[Y/Mg]$ pour les étoiles du disque galactique, l'outil automatisé GAUGUIN, intégré à la chaîne Gaia DPAC APSIS, a été optimisé et testé. En particulier, les capacités d'estimation d'abondances chimiques ont été améliorées pour des grilles de spectres synthétiques irrégulières, couvrant une large gamme de paramètres atmosphériques stellaires.

Troisièmement, le ratio $[Y/Mg]$ a été estimé pour environ 2000 étoiles à partir des données spectroscopiques d'AMBRE HARPS. Les erreurs internes et externes des abondances ont été soigneusement analysées. Les étoiles étudiées appartiennent principalement aux disques mince et épais galactique, dans la gamme de métallicité allant de $-1,0$ dex à $0,5$ dex.

Quatrièmement, grâce à l'estimation d'âge basée sur l'adaptation des isochrones pour 342 "turn-off" étoiles d'échantillon, la sensibilité à l'âge du rapport $[Y/Mg]$ a été étudié. L'analyse révèle une corrélation claire entre $[Y/Mg]$ et l'âge pour les étoiles du disque mince de différentes métallicités. Cela correspond aux études antérieures sur les étoiles de type solaire. De plus, aucune dépendance à la métallicité avec l'âge stellaire n'est détectée, donc le ratio $[Y/Mg]$ peut être utilisé comme un indicateur fiable d'âge.

Enfin, la relation $[Y/Mg]$ versus l'âge présente une discontinuité entre les étoiles du disque épais autour de 9–10 Gyrs. Pour ces étoiles, la corrélation est différente et a une tendance probablement plus forte avec l'âge. Cela reflète la différence dans les histoires d'évolution chimie pour les deux composantes du disque.

Keywords— étoiles: âges - étoiles: abondances - étoiles: évolution - étoiles: paramètres fondamentaux - Galaxie: disque - Galaxie: évolution

Abstract

Stars record the past in their ages, chemical compositions and kinematics. They can provide unprecedented detailed constraints on the early epochs of galaxy formation, back to redshifts greater than two (a look-back time of around 10 billion years). In particular, stellar ages are crucial to the understanding of the Milky Way history and for comparison with galactic evolution models.

The advent of the Gaia space mission has opened the path to stellar age estimations for large samples of stars, in particular, based on isochrone fitting methods. In addition, Gaia precise distances allow to develop indirect age estimations based on the stellar population chemical evolution clock. In fact, the chemical abundance patterns imprinted on stellar atmospheres represent the gas conditions at the time of the stars' formation back to redshifts greater than two. The chemical evolution products of different nucleosynthetic channels can therefore provide a time proxy. After calibration, it can be used as an age estimator.

This thesis is focussed on the use of a particular chemical clock, the $[Y/Mg]$ abundance. To this purpose, the astrometric Gaia mission data from the first data release was combined with high resolution spectroscopic data from the AMBRE-HARPS catalogue. First of all, the object identification of the AMBRE archival data was improved, thanks to a cross match with the 2MASS catalog, and later the Gaia DR1. In total, 6776 different stars have been identified.

Secondly, in order to obtain precise estimations of the $[Y/Mg]$ abundance ratio for galactic disc stars, the automated GAUGUIN tool integrated in the Gaia DPAC APSIS chain, has been optimized and tested. In particular, the abundance estimation capabilities of the APSIS GAUGUIN tool have been improved for irregularly distributed synthetic spectra grids, spanning a large range in stellar atmospheric parameters.

Thirdly, the $[Y/Mg]$ abundance ratio has been estimated for about 2000 stars from the AMBRE HARPS spectroscopic data. In addition, the internal and external errors of the abundances were carefully analysed. The studied stars belong mainly to the galactic thin and thick disc, in the metallicity range from -1.0 dex to 0.5 dex.

Fourth, thanks to the isochrone fitting age estimations of 342 turn-off stars of the sample, the age sensitivity of the $[Y/Mg]$ ratio has been studied. The analysis reveals a clear correlation between $[Y/Mg]$ and age for thin disk stars of different metallicities, in synergy with previous studies of Solar type stars. In addition, no metallicity dependence with stellar age is detected, allowing to use the $[Y/Mg]$ ratio as a reliable age proxy.

Finally, the $[Y/Mg]$ vs. age relation presents a discontinuity between thin and thick disk stars around 9–10 Gyrs. For thick disk stars, the correlation has a different zero point and probably a steeper trend with age, reflecting the different chemical evolution histories of the two disk components.

Keywords— stars: ages – stars: abundances – stars: evolution – stars: fundamental parameters – Galaxy: disk – Galaxy: evolution

Remerciements

Au cours de ces 10 dernières années j'ai étudié la physique stellaire; cette thèse marque maintenant la fin de ma vie étudiante. Je voudrais remercier tous les enseignants qui ont partagé leur expérience avec moi et, en premier lieu la directrice de cette thèse, **Alejandra Recio-Blanco**, pour m'avoir guidée et apporté son savoir.

Je suis reconnaissante à **Thierry Lanz**, **Philippe Stee** et le groupe administratif, en particulier **Betty Bonhomme**, **Joël Bealu**, **Christine Delobelle**, **Sophie Rousset** et **Catherine Blanc**, pour leur aide avec les problèmes administratifs apparus pendant ces années.

Merci à **Mathias Schultheis**, **Patrick de Laverny** et **Vanessa Hill** pour leur disponibilité à discuter sur divers sujets scientifiques. J'exprime mes remerciements à **Cristoph Ordenovic** pour sa patience pour notre travail sur la version Java de la méthode GAUGUIN. Je remercie les membres d'équipe **GAG** et **séminaires Lagrange** pour les rencontres pertinentes et intéressantes, pour rester au courant des nouvelles astrophysiques.

Mes remerciements à **Elena Lega** et **Chiara Ferrari** pour leur aide et leurs conseils.

Merci au groupe de support technique, **Daniel Kamm**, **Ghibaud Jean-Philippe** et **Marie-Laure Miniussi**, pour leurs réponses rapides et efficaces en cas de problème.

Je voudrais remercier mes collègues du bureau, **Edouard Bernard** et **Michael Hayden**, pour leur patience et leur courage de s'engager dans les dialogues parfois très étranges. Merci à tous mes frères-en-thèse (**Francesco**, **Govind**, **Camemberto**, **Pablo**, **Michael II**, **Emma**, **Sophia**, **Emmanuele**, **Marina**, **Rémi**, **Brynna**, **Ximena**, **Alvaro**, **Gabriele**, **Clément**, **Tobias**, **João**, **Michael**, **Raphael**, **Elena**, **Vitaly**, **Go**) pour la joie de ces années.

Avec un grand plaisir je mentionne ici **Laurent Galluccio**, pas seulement parce qu'il m'a demandé plusieurs fois de le mettre dans la liste de remerciements, mais surtout pour son aimabilité et sa gentillesse. Un grand merci à **Bernard Pichon**, **Serge Bonhomme**, **Dominique Triboire** et les amis d'**Ateliers et Services Techniques** pour leur humour.

Je mentionne ici le groupe de la cantine, **Khaled**, **Karima** et **Dominique**, qui rend notre vie plus heureuse. J'apprécie Khaled pour toutes les choses qu'il m'a lancées à la tête, mais heureusement ratée.

Merci à **Nathalie Nergeault** et **Seyna n'Diaye** pour nos moments divertissants et leur aide pour certaines questions du quotidien.

Merci **Eric Fossat**, **Michèle Pascaud**, **Farrokh Vakhili** et **Lionel Bigot** pour les beaux jours passés ensemble dans les montages.

Merci à **Sylvie** de la part de la bichette pour le temps qu'on a passé ensemble.

Merci à toi, **Aymeric**, d'être avec moi dans les situations heureuses et moins heureuses.

Merci à toi, **Gilles**, pour nos dialogues constructifs et pour tout ce que tu fais pour moi.

Enfin, j'aimerais remercier **ma famille** pour son soutien et son aide dans toutes les situations qui se présentent dans ma vie.

Acknowledgements

During the past 10 years I have studied stellar physics, and this thesis marks the end of my student life. I would like to acknowledge all the teachers who have shared their experience with me during these years, and first of all, the director of this PhD-project **Alejandra Recio-Blanco** for her guidance and mentorship during my PhD.

I am thankful to **Thierry Lanz, Philippe Stee** and those in administration, especially **Betty Bonhomme, Joël Bealu, Christine Delobelle, Sophie Rousset** and **Catherine Blanc**, for their help with diverse administrative problems, that have appeared during these years.

Thanks to **Mathias Schultheis, Patrick de Laverny** and **Vanessa Hill** for their availability to discuss any scientific problems. In particular, I would like to express my thanks to **Cristoph Ordenovic** for your patience in our work on java-version of the GAUGUIN method. With a pleasure I thanks all the members of **GAG group** and **Lagrange seminars** for useful and interesting meetings, that allow to stay in the flow of modern ideas of astrophysics.

My respectable thanks to you, **Elena Lega** and **Chiara Ferrari**, for your help and advice.

Thanks to technical support group, **Daniel Kamm, Ghibaud Jean-Philippe** and **Marie-Laure Miniussi**, for their rapid answers in the case of technical issues.

I would like to thank my office mates, **Edouard Bernard** and **Michael Hayden**, for their patience and interesting conversations, of varying levels of strangeness. Thanks to all of my brothers and sisters-in-PhD (**Francesco, Govind, Camemberto, Pablo, Michael II, Emma, Sophia, Emmanuele, Marina, Rémi, Brynna, Ximena, Alvaro, Gabriele, Clément, Tobias, João, Michael, Raphael, Elena, Vitaly, Go**) for the fun and joy of these years.

With a pleasure I mention **Laurent Galluccio** here, not just because he asked many times to put his name in the acknowledgement list, but for his kind and gentle nature. Thank you **Bernard Pichon, Serge Bonhomme, Dominique Triboire** and friends from **Workshops And Technical Services** for your humour.

I can not skip the group from the canteen, **Khaled, Karima** and **Dominique**, that makes our daily lives more happy and fulfilled. I appreciate Khaled for all the things that he had thrown at me, but fortunately did not really reach the target.

Thanks to **Nathalie Nergeault** and **Seyna n'Diaye** for your help in some daily questions.

Thank you, **Eric Fossat, Michéle Pascaud, Farrokh Vakhili** and **Lionel Bigot**, for some sunny days that we have spent out together in the mountains.

A lot of kisses I send to **Sylvie** from "la bichette".

Thank you, **Aymeric**, for being with me in happy and not really moments.

Thank you, **Gilles**, for our constructive dialogues and for that you are doing for me.

Last but not least, I would like to thank **my family** for their support and understanding in different situations of my life.

Contents

1	Introduction	1
1.1	Historical aspects and present day context	2
1.2	Stellar components of the Galaxy	3
1.2.1	<i>The thin and the thick disks</i>	5
1.3	Stellar Ages	6
1.3.1	<i>Asteroseismology</i>	6
1.3.2	<i>Nuclear cosmochronology</i>	7
1.3.3	<i>Isochrone fitting methods</i>	7
1.3.4	<i>Indirect chemical proxies</i>	7
1.4	Spectroscopy of stellar atmospheres	10
1.4.1	<i>Continuous spectra</i>	10
1.4.2	<i>Spectral lines</i>	10
1.5	The models of stellar atmospheres	13
2	The Gaia mission as a new observational era	15
2.1	Gaia instruments	16
2.1.1	<i>Astrometry: ASTRO</i>	16
2.1.2	<i>Photometry: BP/RP</i>	16
2.1.3	<i>Spectroscopy: RVS</i>	17
2.2	Data Processing and Analysis Consortium	18
2.3	CU8 and GSP-Spec	20
2.4	The Gaia data releases	21
2.4.1	<i>First data release DR1</i>	21
2.4.2	<i>Second data release DR2</i>	22
2.4.3	<i>Future DR3+</i>	23
2.5	Summary	23
3	Building up the AMBRE-TGAS catalogue	25
3.1	The AMBRE project	26
3.2	Procedures	26
3.2.1	<i>Object identification: search radius</i>	27
3.2.2	<i>Object identification: estimated photometric temperatures</i>	27
3.2.3	<i>Object identification: comparison of object names</i>	27
3.2.4	<i>Object identification: quality labels</i>	28
3.2.5	<i>Additional flags for post-cross-match validation</i>	28
3.3	AMBRE HARPS	29
3.4	AMBRE UVES	33

3.5	AMBRE FEROS	36
3.6	Summarizing different instruments: the total AMBRE catalogue	40
3.7	The AMBRE – TGAS catalogue	43
4	The GAUGUIN – automatic method of stellar abundance determination: optimization and tests	45
4.1	The models of stellar atmospheres	46
4.2	Overview of stellar abundance determination – methods "on the fly"	46
4.2.1	<i>Automatic methods using synthetic profile fitting</i>	46
4.2.2	<i>Automatic methods using equivalent width fitting</i>	47
4.3	Pre-calculated grid – the GAUGUIN method	47
4.4	Interpolation on the parameter grid	49
4.5	Normalization of the spectra	52
4.6	Visualisation	54
4.7	Summary	55
5	Abundances of Mg and Y	57
5.1	Observations and synthetic grid	57
5.2	Spectroscopic sample: selection of Mg and Y lines	58
5.3	Methodology of the chemical abundance estimation	59
5.4	Abundance error estimation	60
5.5	Summarizing Mg and Y stellar abundances	62
6	[Y/Mg] correlation with Age	65
6.1	Age estimations	65
6.2	Exploring the age dependence of the Y, Mg and Fe abundance	66
6.3	Exploring the age dependence of the [Y/Mg]	68
6.4	The chemical clock: inverting the [Y/Mg]-Age relation	70
6.5	Differences between the thin and the thick disk	71
6.6	Summary	72
7	General conclusions	73
7.1	Summary	73
8	Tycho and HIPPARCOS	77
9	Problems with non-adapted GAUGUIN-java version	79
	Bibliography	89

CHAPTER 1
Introduction

Contents

1.1	Historical aspects and present day context	2
1.2	Stellar components of the Galaxy	3
1.2.1	<i>The thin and the thick disks</i>	5
1.3	Stellar Ages	6
1.3.1	<i>Asteroseismology</i>	6
1.3.2	<i>Nuclear cosmochronology</i>	7
1.3.3	<i>Isochrone fitting methods</i>	7
1.3.4	<i>Indirect chemical proxies</i>	7
1.4	Spectroscopy of stellar atmospheres	10
1.4.1	<i>Continuous spectra</i>	10
1.4.2	<i>Spectral lines</i>	10
1.5	The models of stellar atmospheres	13

1.1 Historical aspects and present day context



Figure 1.1: The ESO 3.6-metre telescope at La Silla, during observations. Credit: ESO / S. Brunier

The sky plenty of stars excited humans eye from a very early epoch. The first traces of astronomical observations come from VI-IV BC, and the first names of some celestial bodies were found in a religious monument, the Pyramids, created in XXV-XXIII BC. We can find astronomical tables and lunar calendars from Babylon in II BC. In the Ancient Egypt, lunar calendars with metonic cycles appear. Careful observations of celestial bodies and eclipses, dated by court astronomers in China in III-II BC, are reported. The tight relations of observational astronomy, religion and daily life were exceptional for the Inca Empire (XI-XVI) and the Maya civilization (II BC - X). In addition, astronomy had a wide use in the Ancient Greece, where some cosmogonist models of the origins of our Universe were proposed.

These ancient astronomical remains amaze today by their precision and flair to explain the astronomical surrounding thanks only to a few basic observations. A long way has been made since then, arriving nowadays, through the progressive development of observational instruments and fundamental physics, to the modern view of the Universe.

Obviously, many important questions remain to be solved and, among them, the formation of our galaxy, the Milky Way, is of the most fundamental ones. Galactic Archaeology aims at unveiling the history of the Milky Way by analysing stars, just as the history of life was deduced from examining rocks. Stars record the past in their ages, compositions and kinematics and can provide unprecedented detailed constraints on the early phases of galaxy formation, back to redshifts greater than two (a look-back time of 10 billion years). In particular, in some cases the chemical abundance patterns imprinted on stellar atmospheres could

reflect the gas conditions at the time of the stars formation. In general the continuous producing of different chemical elements due to thermonuclear burning should be taken into account. The "chemical tagging" approach (Freeman and Bland-Hawthorn, 2002) opens the way to the temporal sequencing of a large fraction of stars.

This thesis research is precisely dedicated to stellar dating through the analysis of the stars chemical abundances. Since the advent of stellar astrophysics, the estimation of stellar ages has been a crucial challenge with many fundamental implications. Starting with the historical debate around the age of our Sun, stellar ages have been recognized as clocks of the evolving Universe that we wish to understand. They are the basis of stellar evolution studies, of the stellar properties coded in chemical evolution analysis, and more generally, a key piece of information of our understanding of any stellar population. Numerous dating methods have been developed, based on different physical processes and models. Nuclear cosmochronology (Hoyle and Fowler (1960), Bland-Hawthorn and Freeman (2014)), isochrone fitting (first discovered by Schaltenbrand (1974), Luri et al. (1992), Valls-Gabaud (2014)), asteroseismology techniques (Pesnell (1987), Guzik et al. (2000)) and more indirect chemical proxies of stellar age have been used and applied to very different samples of stars. In particular, for Galactic Archaeology studies, dating techniques applicable to large numbers of objects are crucial. In this framework, secondary clocks, like chemical abundance age proxies ([Y/Mg] one was used in this work) are important to extend the possibility of stellar dating i) outside the sphere of precise distance estimations and ii) to stars in different stellar evolutionary stages.

1.2 Stellar components of the Galaxy

In the current cosmogony paradigm, a Λ -Cold Dark Matter (Λ CDM) cosmology, dark matter and dark energy shape the large-scale expansion of the Universe, while on smaller scales, tiny initial fluctuations grow into large dark matter halos, where galaxies like ours form. Galaxies grow through a sequence of merger and accretion events and, inside galaxies, baryon matter aggregates to form stars. However, the interplay between gas, stars, black holes, dark matter and dark energy has only started to be understood.

The historical vision of the galactic stellar populations in galaxies was introduced by Baade (1946). He defined three main categories, based on the physical distribution of the stars in space, their position in the Hertzsprung-Russell diagram (Fig. 1.4), and the stellar motion about the galaxy. Population I contains stars in the galactic disk. It is a young population having a high rotation velocity, small velocity dispersion of their velocities (around 10-15 km/s), and high abundance of metals. Population II is composed of old stars (like globular clusters in the halo), having low rotational velocity, high velocity dispersion (around 75 km/s) and low metal abundances. Population III is theoretically predicted to be composed of first stars that were generated after the Big Bang, basically consisted of hydrogen (p-p chain). They are predicted to be very massive and thus quickly exploded. The modern view

on stellar populations is much complex that a simple separation in three categories.

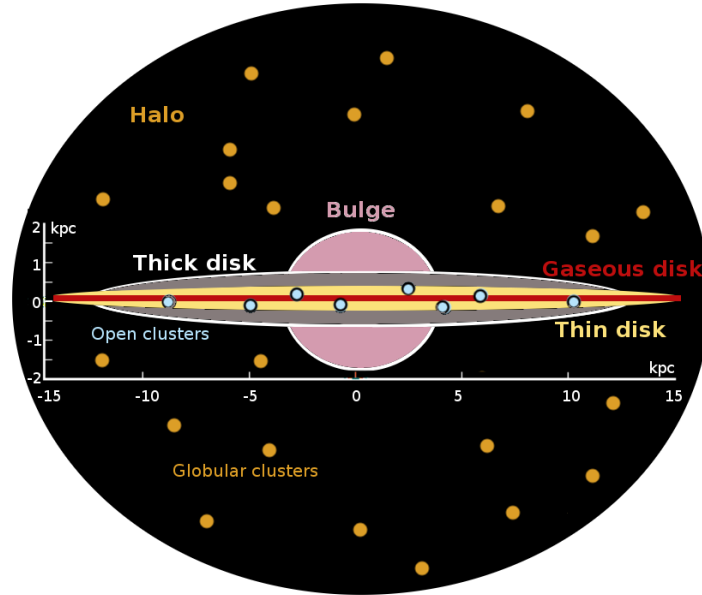


Figure 1.2: Schematic representation of components of our Galaxy.

Later on, [Eggen et al. \(1962\)](#) were the first to show that it is possible to study Galactic archaeology using stellar abundances and dynamics. They inferred that the Galactic metal-poor stars reside in a halo that was created during the rapid free-fall collapse of a isolated protogalactic cloud shortly after it decoupled from the universal expansion. This picture was challenged by [Searle and Zinn \(1978\)](#), who, studying globular clusters, suggested a halo built up over an extended period from independent fragments. The ideas of galaxy formation via hierarchical aggregation of smaller elements from the early Universe fit in easily with the view of a Galaxy formed from small fragments. Although the hierarchical model may be fundamentally different from the collapse model, it may have a few features in common. It is not unlikely that, early on in the history of the Galaxy, there was a phase which could be described as a fast dissipative collapse, but which was triggered by gas-rich mergers ([Brook et al. 2004](#)), rather than by the collapse of a giant gas cloud. Collisionless minor mergers are also proposed today to play a role in the formation of our Galaxy ([Toomre, 1977](#)) as well as external gas accretion from filaments of the cosmic web and internal secular processes ([Kormendy and Kennicutt, 2004](#)).

In this framework, the Milky Way is defined today as a late-type spiral, conventionally decomposed into: (i) a central bar – bulge that extends out to ~ 3 kpc; (ii) a nearly spherical halo that extends out to of order 100 kpc and is studded with globular clusters; (iii) a disk that defines the Galactic plane and is probably confined to radii R less 15 kpc. The disk is often decomposed into two components, a metal rich thin disk, in which the density falls with distance Z from the plane exponentially with scale height 300 pc and a more metal poor thick disk, which is characterised by a vertical scale height 700 pc ([Kordopatis et al., 2011](#)).

The thin disk is patterned into spiral arms but even now, the final word on the number and positioning of the arms present has not been spoken. Beyond the Sun the thin disk is warped.

1.2.1 *The thin and the thick disks*

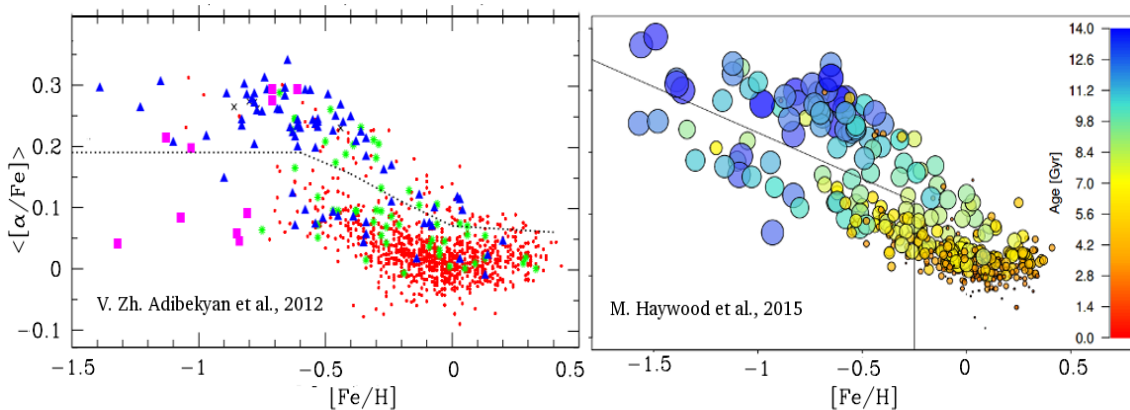


Figure 1.3: Abundance ratios $[\alpha/\text{Fe}]$ vs. $[\text{Fe}/\text{H}]$.

On the left: the blue triangles refer to the thick disk, red circles to the thin disk, magenta squares to the halo, the green asterisks and the black crosses to the transition stars between thin-thick and thick-halo, respectively. The black dashed curve separates the stars with high-/low α content. Credit: [Adibekyan et al. \(2012\)](#).

On the right: Same as the left panel but colour coded by age (the larger implies older). Credit: [Haywood et al. \(2015\)](#).

[Yoshii \(1982\)](#) and then [Gilmore and Reid \(1983\)](#) found that the vertical number density gradient of stars in the Solar neighbourhood could not be fit by a single exponential. Instead, the density was well described by a two-component fit, one with a short scale height and one with a larger scale height. These two components became known as the thin and thick disks respectively.

The range of iron abundances in thick disk stars lies within $[\text{Fe}/\text{H}]$ from around -1.0 to -0.5 dex, to be compared to the younger thin disk within $[\text{Fe}/\text{H}]$ from around -0.5 to $+0.3$ dex.

The geometrical scale heights are about 900 pc for thick disk and 300 pc for thin disks ([Jurić et al. \(2008\)](#)). In comparison to the thin disk, the stellar populations of thick disk have higher dispersion in vertical kinematics, older stellar ages ([Mason and Gilmore, 2015](#)) and higher ratio α -element abundances to iron content in sub-solar metallicity range ([Fuhrmann \(1998\)](#), [Bensby et al. \(2003\)](#), [Adibekyan et al. \(2013\)](#), [Recio-Blanco et al. \(2014\)](#)).

Since the first works highlighting the existence of the Milky Way's thin-thick disk dichotomy, the study of the structural and chemo-dynamical transition between the two disk populations has opened new pathways to constrain Galactic evolution models. Supported by the hierarchical formation of galaxies in the Λ CDM paradigm, external mechanisms have

been invoked to explain the chemo-dynamical characteristics of thick disk stars. Among them, the accretion of dwarf galaxies (Statler (1988), Abadi et al. (2003))

and minor mergers of satellites (Quinn et al. (1993), Villalobos and Helmi (2008)) heating the disk dynamically, have been proposed. Similarly, Jones and Wyse (1983), Brook et al. (2004) and Brook et al. (2007) have proposed that the thick disk would have been formed from the collapse produced by the accretion of a gas-rich merger. On the other hand, purely internal formation mechanisms have also been proposed, such as the early turbulent phase of the primordial disk (Bournaud et al., 2009) and the stars radial migration due to resonances with the spiral structure or the bar of the Milky Way (Schönrich and Binney (2009), Minchev and Famaey (2010), Loebman et al. (2011)), although see also Minchev et al. (2012). The relative importance of the different proposed physical processes of evolution can now be tested with increasing robustness thanks to the Galactic spectroscopic surveys targeting the disk stars.

1.3 Stellar Ages

The advent of the Gaia space mission (Chapter 2) has opened the path to stellar age estimations for large samples of stars, in particular, thanks to isochrone fitting methods. In addition, Gaia precise distances allow to develop indirect age estimations based on the stellar population chemical evolution clock. In the following, the main techniques of stellar age estimation are presented.

1.3.1 Asteroseismology

Historically, asteroseismology was centred in the study of solar atmosphere pulsations, excited and damped by a near-surface convection (Pesnell (1987), Brown et al. (1994), Gautschi and Saio (1995) & Gautschi and Saio (1996)). The oscillation frequencies depend on the properties of stellar interior. Since these are tightly linked with the mass and evolutionary status, the mass and age of a star can be estimated from the comparison of its oscillation spectrum with stellar model predictions. The physical origin of these oscillations can be found in two types of waves. First, acoustic waves (so-called pressure modes), and second, internal gravity waves (e.g., see Houdek et al. (1999), Samadi and Goupil (2001) & Samadi et al. (2001)). Asteroseismology age estimations are significant for solar-type and red-giant stars (Bedding et al., 2011), because the presence of a near-surface convection is a necessary condition for stars to show oscillations. The problems of modelling a star, in particular, the uncertainties on global parameters and chemical composition, and our misunderstanding of processes in stellar interiors (as the transport processes that may lead to core mixing and affect the model ages), put the limit on the age estimation accuracy.

1.3.2 *Nuclear cosmochronology*

This high-precision method is based on the spectroscopic abundances of heavy radioactive isotopes, taking into account the constant rate of radioactive decay, for example ^{238}U and ^{232}Th (Hoyle and Fowler (1960), Butcher (1987), Hill et al. (2002), Bland-Hawthorn and Freeman (2014)). Based on the knowledge about the half-life time for these elements, the initial age of the matter from which the star was created, can be estimated. For this reason, the method can be effectively applied to old metal-poor stellar content of the Galaxy. This limitation together with a poor presence of uranium and thorium lines in the stellar spectra put severe limitations on the possibility to widely applying this method for the Galactic Archaeology.

1.3.3 *Isochrone fitting methods*

The story of the stellar ages determination for multiplicity of objects started with the use of isochrone fitting at the end of XX century. The first attempt comes from Schaltenbrand (1974). The method consists in a comparison of absolute luminosity (or magnitude) and effective temperature (or color) with theoretical models, thus estimating the nearest point of the zero-age main sequence to a star on a two-color diagram (Valls-Gabaud, 2014). These models are represented on the Hertzsprung-Russel diagram with the lines, associated with populations of stars of the same age (Fig. 1.4). For this purpose different sets of isochrones can be used spanning a large range of stellar ages (Padova, Yonsei-Yale, Dartmouth etc.).

Many groups succeeded in the application of Bayesian methods to the isochrone-fitting age determination (Jørgensen and Lindegren, 2005). The relative likelihood distribution of probable values of stellar ages for the star after elimination of IMF and initial metallicity represents a probability for the star to have one or another stellar age inside confidence intervals.

However, one of the main limitations of the method is that it can only give reliable results for the turn-off stage and the sub-giant branch. Thus, the method can be mainly applied to late A-type, F and G-dwarfs (Jørgensen and Lindegren, 2005). For other populations there may exist many age-values estimations for the same object due to the overlapping of the different isochrones.

1.3.4 *Indirect chemical proxies*

Apart from the primordial Big Bang nucleosynthesis that occurred during the first three minutes of the Universe, stars themselves produce chemical elements in a chain of nuclear reactions during their lifetimes. The type of thermonuclear reactions depends basically on the initial mass of the star, the type and place (core- or in layer-burning) of the thermonuclear reaction together describe evolution status of the star. Finally, produced chemical elements can be ejected into interstellar medium due to the explosion process – explosions as supernova type Ia-II, explosions of asymptotic giant-branch stars, stellar winds, planetary nebulae etc.

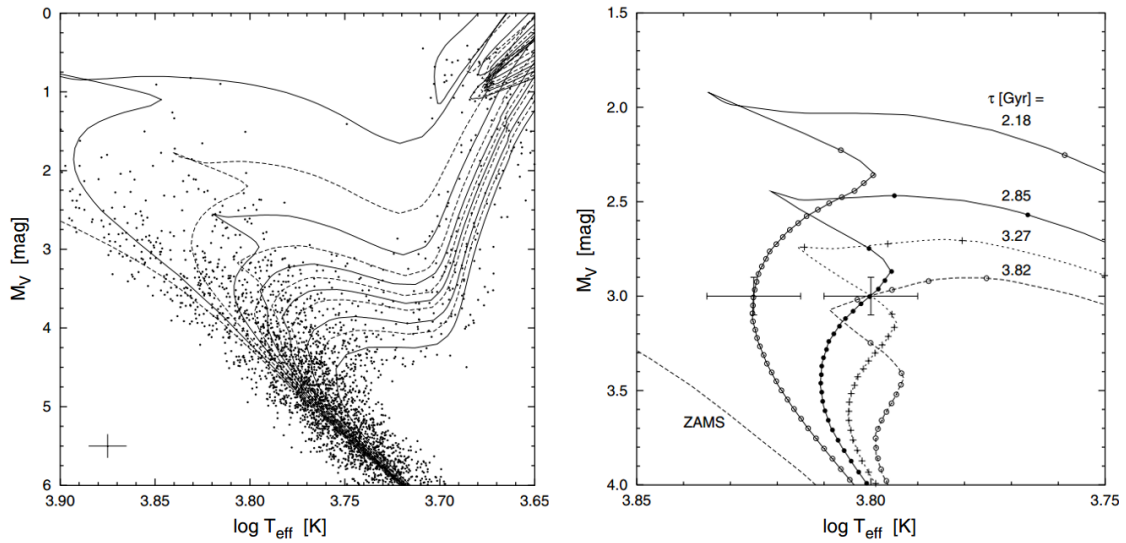


Figure 1.4: The HR diagram for the synthetic sample of 2968 stars (on the left) and the location of two hypothetical observation (on the right), the lines represent the set of isochrones of different ages. The example shows the critical case when the isochrone fitting gives a multiple solution for the same object. On the left: isochrones are for 0, 1, 2,..., 8, 10, 12 and 15 Gyr. On the right: the symbols along isochrones show where initial mass is a multiple of $0.01 M_{\text{sun}}$. Credit: [Jørgensen and Lindegren \(2005\)](#)

The processes of nucleosynthesis pass through hydrogen burning (the proton-proton chain or the CNO-cycle), helium (α -process), carbon, neon, oxygen and silicon burnings. During these processes the elements up to iron and nickel can be created. Heavier elements can be created by neutron capture processes (slow neutron capture "s-process") or during explosion, as supernovae (the rapid neutron capture "r-process", the rapid proton capture process "rp-process", and the proton capture "p-process"), which results in the nuclei photo-disintegration.

As the time scales of the various nucleosynthetic processes are different, the chemical abundance ratio of two elements produced by two different channels provides a time estimate with respect to the chemical enrichment of the studied population. Indirect chemical age proxies have been used for galactic archaeology studies in the last decades, their precision and applicability domains (e.g. metallicity and age intervals) are very badly constrained. The arrival of precise distances from the Gaia mission (Chapter 2) allows today to analyse them and calibrate them in detail. In addition, high-resolution stellar spectra of different stellar types are nowadays available thanks to big spectroscopic surveys (as for example, Gaia-ESO Survey, RAVE, APOGEE,...). They allow to determine stellar abundances with a high precision, using different algorithms and reference data (See Chapter 3, Chapter 4). This amount of spectroscopic data opens a new epoch of precise stellar dating for big samples of stars, based on the calibration of different chemical abundances with stellar ages (see Chapter 6).

[α /Fe] abundance ratio.

α -elements are predominantly synthesized in high-mass, very short-lived stars, and are ejected by type II supernova explosions (SN II). Iron is produced by both SN II and type I supernovae (SN Ia), whose binary progenitors are believed to have a longer pre-explosion lifetime of typically one billion years (1 Gyr). Comparing the relative abundances of the α -elements and iron provides a measure of the SN Ia/SN II ratio, and in turn a clock. In the galactic disk, the distribution of [α /Fe] versus metallicity plane shows bimodal distribution, that is associated with stellar thick and thin disks (Adibekyan et al. (2012), Recio-Blanco et al. (2014)). Thick disk stars have higher [α /Fe] abundances than thin disk stars of the same metallicity, showing also a faster evolution of their [α /Fe] abundance with time (Haywood et al. (2013), Hayden et al. (2017)).

[C/N] abundance ratio.

Carbon and nitrogen are expected to be good indicators of stellar masses (Masseron and Gilmore (2015), Martig et al. (2016)). A star arrived on the giant branch, has its convective envelope extended deep inside. These convective movements bring processed through the CNO-cycle material up to the stellar surface (so-called "dredge-up"). As a result of such convective mixing, a change in the [C/N] abundance ratio at the stellar surface is observed (Iben (1965), Salaris and Cassisi (2005)). The final [C/N] ratio at the surface depends on the stellar mass, because the [C/N] abundance ratio in the core and the depth reached by the dredge-up depend on stellar mass. Since mass and age are closely related for stars on the giant branch, it makes the [C/N] ratio a rather good proxy of stellar ages (Salaris and Cassisi, 2005).

[Y/Mg] abundance ratio.

Yttrium is known to be mainly produced by s -processes in the asymptotic giant branch stage of intermediate and low mass stars. On the other hand, magnesium, as an α -process element, is produced by SN type II in a shorter time scale. That makes the [Y/Mg] abundance ratio another good proxy for stellar age dating. Contrary to the method based on the [C/N] abundance ratio, the [Y/Mg] ratio does not require additional assumptions on internal stellar structure. Since the studies of da Silva et al. (2012), Nissen (2015), Spina et al. (2016), Tucci Maia et al. (2016), and the recent work of Anders et al. (2018), a correlation of [Y/Mg] with stellar age for solar twins has been noticed. In the work of Feltzing et al. (2017) they studied the relation for dwarf stars in the Solar neighbourhood in a wider range of metallicities, and Slumstrup et al. (2017) find that this relation works also for solar metallicity stars over the helium-core-burning phase. Nevertheless those pioneer studies, the actual precision and validity domain of the [Y/Mg] ratio as an age estimator is largely unknown. One of the goals of the present thesis is the study of [Y/Mg] abundance ratio age sensitivity in a wide range of metallicities. More precisely, the work is focussed on thin and thick disk stars for which Gaia astrometry data are very precise.

1.4 Spectroscopy of stellar atmospheres

The stellar atmosphere is considered to be a conservative system of gas under an equilibrium of macroscopic parameters. It can be modelled in 1D approximation as a sequence of flat parallel thin layers. The radiation transfer equation in this case could be written as: $dI_\nu/d\tau_\nu = -I_\nu + S_\nu$, where ν is a chosen frequency, I_ν is an intensity, $\tau_\nu = \int_0^z \sigma ds$ is an optical depth at chosen frequency and represents a measure of the extinction coefficient with an atmosphere depth, and $S_\nu = j_\nu/\kappa_\nu$ is a source function, defined as a ratio of the coefficients of emission to absorption. Then, the flux will be simply an integration of the intensity I_ν in solid angle ω in a chosen direction θ per unit of time and frequency: $f_\nu = \int I_\nu \cos\theta d\omega$.

1.4.1 Continuous spectra

In stellar physics the source function plays a key role, as far as its form represents that stars' continuous spectrum. The main source of opacity for different stars depends on its temperature: for hot stars it will be the ionization of neutral atoms of hydrogen HI, for solar type – negative hydrogen ions H^- together with atoms of Si and metals, and for cold stars the increasing number of numerous molecular lines will be important. The veracity of the approximation that the stellar atmospheres are in thermodynamic equilibrium is well confirmed by the fact that for those stars the source function is quite similar to the Planck function:

$$S_\nu = B_\nu(T) = (2h\nu^3/c^2) (\exp(h\nu/(kT)) - 1)^{-1},$$

where c is the speed of light ($2.998 \times 10^{10} \text{ cm s}^{-1}$), $h = 6.626 \times 10^{-27} \text{ eV.s}$ is the Planck constant, $k = 8.62 \times 10^{-5} \text{ eV K}^{-1}$ is the Boltzman constant. Considering this, the concept of effective temperature of the star was introduced as the temperature of a black body with the same size and luminosity as the star have: $F_{star} = \sigma T_{eff}^4$, where F_{star} is a total stellar flux, and $\sigma = 5.670 \times 10^{-8} \text{ W/(m}^{-2}\text{K}^{-4})$ is the Stefan-Boltzman constant.

1.4.2 Spectral lines

Spectral lines are narrow regions ($\Delta\lambda \ll \lambda$) in the spectra with the amplified intensity of the radiation (emission lines) or either weakened intensity of the radiation (absorption lines) compared to the continuous spectrum. The origin of spectral lines is mostly transitions of atoms, ions, molecules and atomic nuclei from one to another energy level.

The presence of spectral lines in stellar spectra means that the atmosphere is absorbing more radiation at those frequencies. For those frequencies the radiation comes from higher and less dense stellar atmosphere layers. There is no equilibrium between radiation and matter, and the radiation is damped due to the transition of the atoms from one energy level to another. This is the way how absorption spectral line appears.

An equivalent width of spectral line is a width of the rectangle with area that equals to the one in the spectral line. This concerns a plot of stellar flux versus wavelength. The

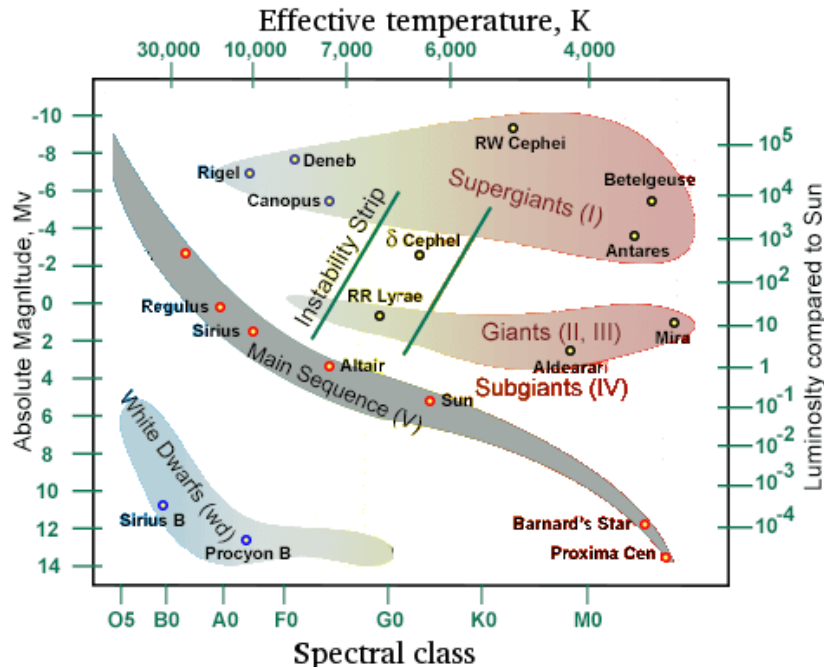


Figure 1.5: Hertzsprung-Russell diagram. Within the same sequence, there are smooth transitions of the parameters of the stars (mass, age, diameter, luminosity, temperature and other parameters.). Stars are classified according to the spectrum.

dependence of the equivalent width of the spectral line with the number of the particles on the line of sight is called the curve of growth (Fig. 1.6).

The diversity of observed stellar spectra gave birth to a classification by stellar spectral type (Morgan-Keenan), that shows a diversity of effective temperatures and luminosity classes (see also the next subsection). The different stellar types can be presented in the so-called Hertzsprung-Russell diagram (see the Fig. 1.5).

Broadening of stellar lines.

The observed profile of the line will be broadened due to many different effects. Apart a broadening of spectral lines, caused by finite spectral resolution of the instrument (so-called *instrumental profile*) there is a list of effects, that impact in the observed profile of a spectral line. Their identification is important because it reveals the physical conditions in stellar atmospheres.

First, *a radiation damping*, i.e. the energy lost of the atom due to the radiation, causes the so-called natural broadening.

Second, *the Doppler effect*, caused by the motion of the observed object, makes an impact in the profile of the spectral line.

Third, *the pressure effects*, i.e. the interaction of the atom with the surrounding particles, broad the observed profile. In this case atomic energy levels are displaced due to the action of inter-atomic electric fields (so-called Stark effect).

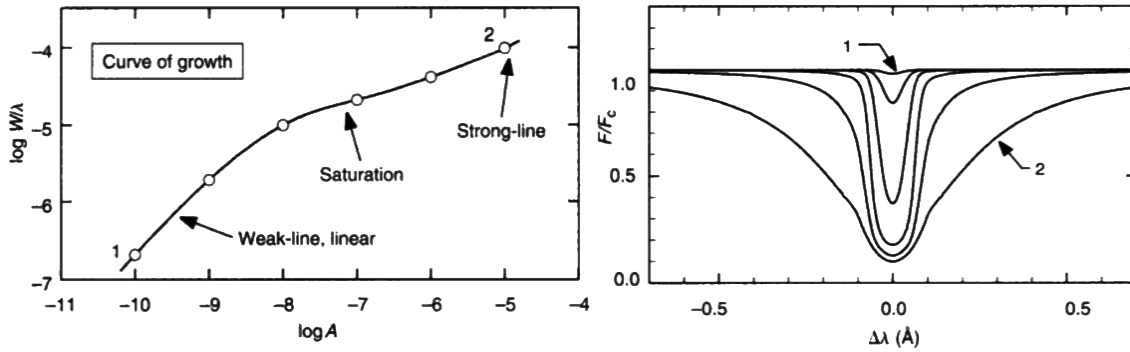


Figure 1.6: The curve of growth for the chemical elements as a function of its abundance. Three possible regimes – linear 1, saturation and strong lines 2 – are represented on the left panel, and their correspondence in the line profile (weak 1 and strong 2) on the right panel. Credit: (Gray, 2005).

The lines can be broadened also by the so-called *Zeeman effect*, the presence of magnetic fields affecting the atom. It is a splitting of the energy levels of atoms, molecules, and ions due to the electrostatic field of the electron (fine structure). It caused by the spin-orbital interaction, i.e. a relativistic interaction of a particle's spin with its motion inside a potential.

The hyper-fine structure can impact the spectral lines profile. It is a splitting of the energy levels of atoms, molecules, and ions, due to the interaction between the magnetic field created by the electron and the magnetic moment of the nucleus. In other words, it is caused by the interaction between the state of the nucleus and the state of the electron clouds.

Spectral lines from stellar atmospheres are normally calculated under the LTE condition (the system is in the equilibrium of all macro parameters, as a temperature, pressure, energy etc). Some additional spectral line effects, caused by the disturbance of local thermodynamic equilibrium, so-called *non-LTE effects*, could make an impact on the form of the spectral line for the elements with even atomic number.

Chemical abundances in stellar atmospheres.

All possible components of stellar composition can be simply defined by a sum of fractional percentages of hydrogen ($X = m_{\text{H}}/M$), helium ($Y = m_{\text{He}}/M$) and other chemical elements (metals, Z): $X + Y + Z = 1$, where m_i is the fractional mass of the element, M is the total mass of the system. The determination of the abundances is given by the number ratio to hydrogen: $A = \log(N_{\text{A}}/N_{\text{H}}) + 12$, it represents a number of hydrogen atoms in the solar photosphere for each atom of another element of another element A . Then the stellar abundances can be referred to the ones from the Sun, and in this case it will be given in a bracket notation: $[X/\text{Fe}] = \log(N_{\text{X}}/N_{\text{Fe}})_{\text{star}} - \log(N_{\text{X}}/N_{\text{Fe}})_{\text{sun}}$, and will be given in units of *dex*. As the result of the last definition, for some practical reasons some additional ratios can be determined as: $[A/\text{Fe}] = [A/\text{H}] - [\text{Fe}/\text{H}]$. This ratio is widely used in astronomy and sometimes it replaces an abundance of the element to the total metal content of the star, even if iron is not the most abundant heavy element in stellar atmospheres. The reason is a presence of numerous iron

lines in a visible part of stellar spectra, that makes it easy to measure.

1.5 The models of stellar atmospheres

The stellar atmosphere of a star can be modelled by a sequence of thin parallel layers under the assumption of local thermal equilibrium. Thus, a grid of individual models can be calculated, corresponding to the physical and chemical conditions of the analysed atmosphere (for example, MARCS models, [Gustafsson et al. \(2008\)](#)). These models contain a set of different parameters: electronic pressure, gas pressure, temperature, optical depth for each atmospheric layer. Each of these models corresponds to an individual value of effective temperature T_{eff} , surface gravity $\log(g)$, metallicity $[M/H]$, abundance of alpha elements $[\alpha/Fe]$ and microturbulence v_{micro} .

The effective temperature T_{eff} is the equivalent of the temperature of the black body, that has the same size as the given star, and that ejects the same amount of energy: $F \sim T_{\text{eff}}^4$. This temperature can also be determined from photometric estimations ([Alonso et al., 1996a](#)).

The surface gravity $\log(g)$ is the expression for the surface gravity of the star with a mass M and radius R , $g \sim M/R^2$, and it's accepted to use its logarithm, $\log(g)$. It can also be determined from photometry (knowing the mass and the distance), or from spectroscopy, based on the ionisation equilibrium of FeI and FeII.

The metallicity $[M/H]$ represents the total stellar chemical abundance for all the elements, that are heavier than He (and not only the iron-content).

The ratio $[\alpha/Fe]$ is the ratio of the alpha-elements (as O, Ne, Mg, Si, S, Ar, Ca, Ti, see Section 1.4) to the iron content in the stellar atmosphere.

The microturbulent velocity v_{micro} represents a thermal velocity, produced by the movements of the "cells" in the stellar atmosphere. It impacts the absorption coefficient of the spectral line, and thus, the form of the spectral line.

Finally, stellar atmosphere models allow to produce theoretical stellar spectra by solving the equations of radiative transfer through stellar atmosphere. The individual chemical abundances can then be estimated by comparison of the observed stellar spectra with the corresponding modelled ones for a given set of atmospheric parameters. It can be realised by measuring equivalent widths or by the fitting of the observed lines with the synthetic profile.

The Gaia mission as a new observational era

Contents

2.1 Gaia instruments	16
2.1.1 <i>Astrometry: ASTRO</i>	16
2.1.2 <i>Photometry: BP/RP</i>	16
2.1.3 <i>Spectroscopy: RVS</i>	17
2.2 Data Processing and Analysis Consortium	18
2.3 CU8 and GSP-Spec	20
2.4 The Gaia data releases	21
2.4.1 <i>First data release DR1</i>	21
2.4.2 <i>Second data release DR2</i>	22
2.4.3 <i>Future DR3+</i>	23
2.5 Summary	23

The Gaia satellite is a space mission of the European Space Agency (ESA), launched on the 19 December 2013 from the Kourou center at Guyane. Gaia’s primary objective are a studies of the Milky Way’s stellar content, the dynamics and current state and formation history. The scientific observations of the Gaia mission cover three principal areas: i) astrometry, including the measurement of stellar positions within an accuracy down to $24 \mu\text{arcseconds}$, parallax, and proper motion, ii) spectro-photometric data analysis in a red band (RP) and blue band (BP) and iii) medium-resolution spectroscopy providing radial velocities and astrophysical parameters determination. Figure 2.2 shows the different instruments in the Gaia’s focal plane.

Gaia performs an all-sky survey of about 10^9 stars in our Galaxy and beyond down to magnitude $G = 20$ (Perryman et al., 2001) and radial velocities estimations for about 200 millions of them (Wilkinson et al. (2005), Recio-Blanco et al. (2006)). Figure 2.3 shows the transmission for different Gaia instruments.

The spacecraft is controlled from the European Space Operations Centre (ESOC, Darmstadt, Germany) using the Cebreros (Spain), New Norcia (Australia), and Malargue (Argentina) ground stations.

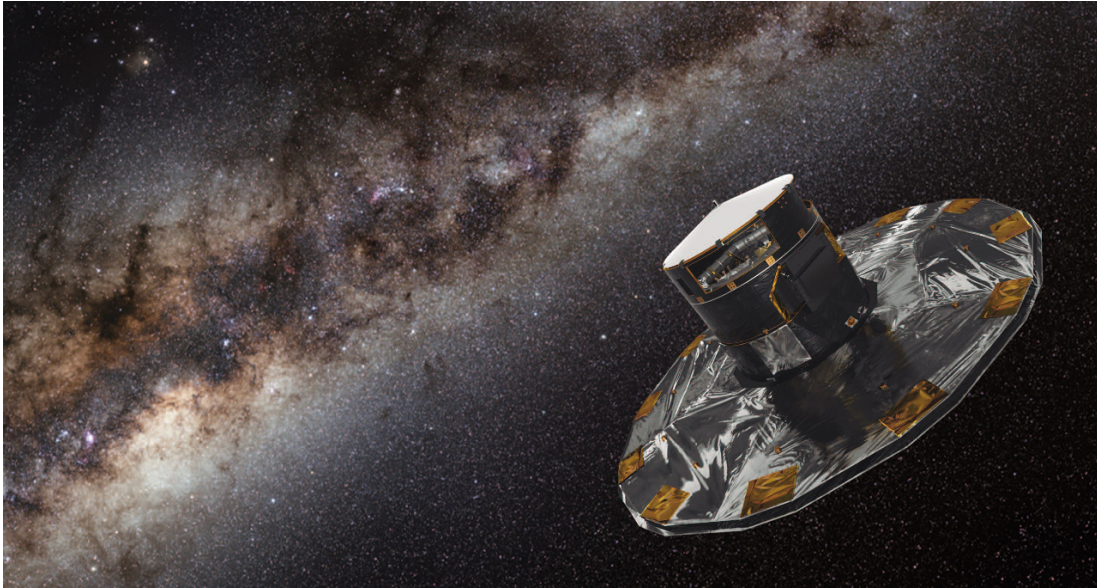


Figure 2.1: Artist representation of the Gaia spacecraft mapping the stars in the Milky Way galaxy. Credit: ESA/ATG medialab/ESO/S. Brunier

2.1 Gaia instruments

2.1.1 *Astrometry: ASTRO*

Gaia measures the relative positions of the thousands of stars that are simultaneously presented in the combined fields of view (Fig. 2.2). The astrometric field in the focal plane is sampled by an array of 62 CCDs charge-coupled device (Boyle and Smith, 1970), each read out is synchronized to the scanning motion of the satellite. Gaia performs an accurate measurement of up to 3 million stars per square degree (for stars with $G < 20$).

The spacecraft scans the sky in a continuously motion. High angular resolution, and thus high positional precision, is provided by the primary mirror of $1.45 \times 0.5 \text{ m}^2$ telescope.

2.1.2 *Photometry: BP/RP*

Photometric observations are collected with the photometric instrument at the same angular resolution as the astrometric observations. Its goal is to enable chromatic corrections of the astrometric observations, to provide astrophysical classification for all objects (e.g. star, quasar, etc.) and astrophysical parametrisation (for instance interstellar reddenings and effective temperatures for stars, photometric redshifts for quasars, etc.).

Gaia's photometric instrument consists of two low-resolution prisms dispersing all the light entering the field of view. One disperser, called BP for Blue Photometer, operates in the wavelength range 330 – 680 nm. The other, called RP for Red Photometer, covers the wavelength range 640 – 1050 nm. The spectral dispersion of the photometric instrument is a

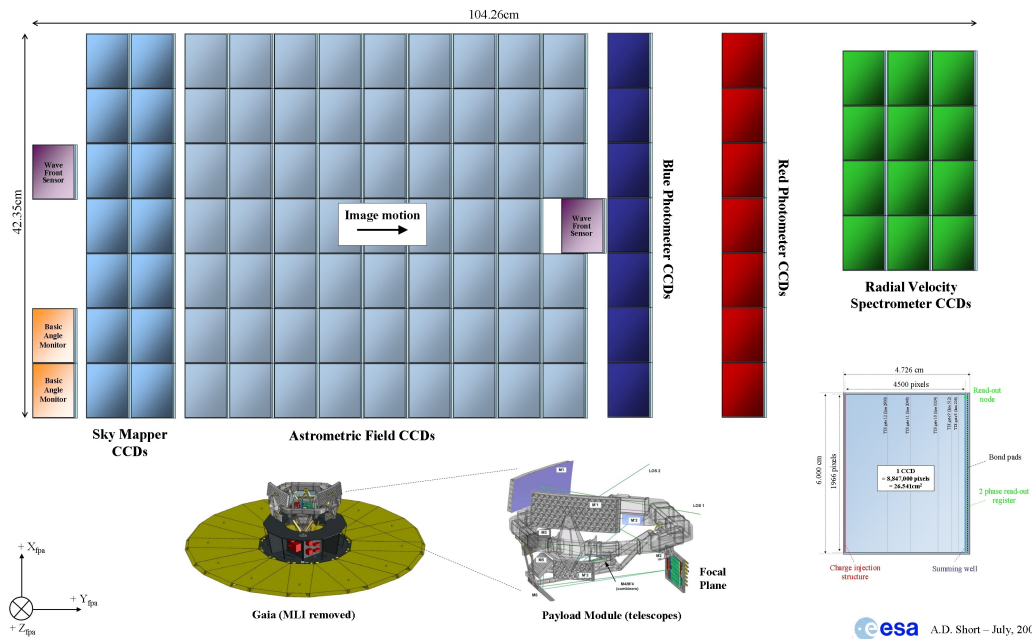


Figure 2.2: Gaia focal plane. 106 CCDs correspond to 938 million pixels and covers 2800 cm². Credit: ESA, Alexander Short

function of the wavelength. It varies in BP from 3 to 27 nm pixel⁻¹ covering the wavelength range 330 – 680 nm, and varies in RP, from 7 to 15 nm pixel⁻¹ covering the wavelength range is 640 – 1050 nm. The 76%-energy of the line-spread function along the dispersion direction varies along the BP spectrum from 1.3 pixels at 330 nm to 1.9 pixels at 680 nm and along the RP spectrum from 3.5 pixels at 640 nm to 4.1 pixels at 1050 nm.

2.1.3 Spectroscopy: RVS

Spectroscopic observations are collected with the spectroscopic instrument RVS for all objects down to $G \sim 16$ mag. It will provide radial velocities through Doppler-shift measurements for ~ 150 million stars. Additionally, astrophysical information, such as interstellar reddening, atmospheric parameters, and rotational velocities, for stars brighter than $G \sim 12.5$ mag will be available. The measurement of the elemental abundances for stars brighter than $G \sim 11$ mag (totally several million stars) will be possible.

The radial velocity spectrometer RVS (Wilkinson et al., 2005), (Katz et al., 2004) provides continuous spectra in the narrow infra-red band from 8470 to 8740 Å with a resolution of 11500 (Fig. 2.3, right). This range has been selected in order to coincide with the peaks of energy-distribution for G- and K-type stars. The primary purpose of the instrument is the determination of the radial velocities and atmospheric parameters, but the stellar abundances of several elements (Ca, Fe, Si, Ni, Ti and possibly Mg) are possible to estimate for these late-type stars. For the early-type stars the abundances of Ca, He and N from weak lines can

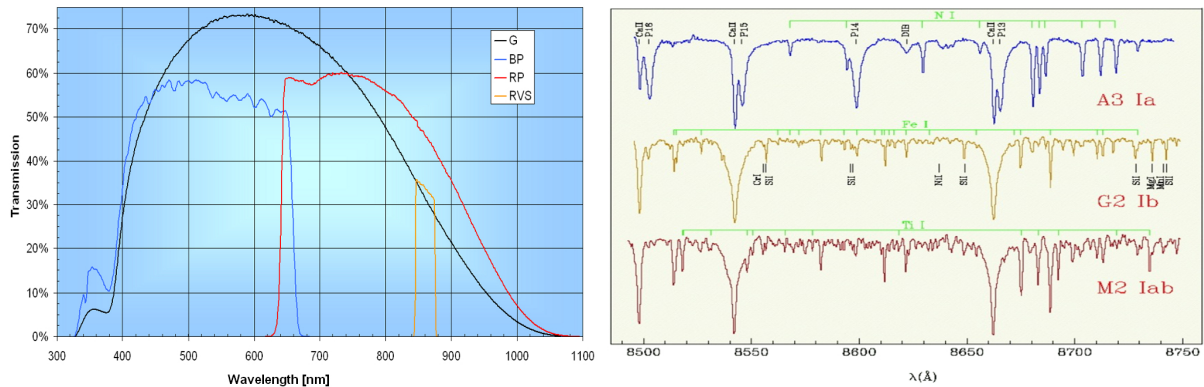


Figure 2.3: On the left: transmission for different Gaia instruments (BP with blue line, RP with red line, and RVS with orange line). On the right: the main lines available with Gaia RVS (from A3 supergiants to M2 type stars). Credit: <http://gaia.obspm.fr/le-satellite/article/le-spectrographe>

be measured, but they will generally be dominated by Hydrogen Paschen lines. The spectroscopic instrument can cope with object densities up to 35,000 stars per square degree. In denser areas, only the brightest stars are observed and the completeness limit will be brighter than $G_{\text{RVS}} = 16$ th magnitude.

The details on the design and other additional information can be found on the Gaia web page (<http://sci.esa.int/gaia/40129-payload-module/?fbodylongid=1916>).

2.2 Data Processing and Analysis Consortium

In order to analyse the pre- and post-launched data, a big consortium of astronomers (Data Processing and Analysis Consortium, DPAC) has been created. DPAC has been in place since 2006 and has the task to develop the data processing algorithms, the corresponding software, and the IT infrastructure for Gaia. It also executes the algorithms during the mission in order to turn the raw telemetry from Gaia into the final scientific data products that will be released to the scientific community.

The responsibilities of the Gaia Data Processing and Analysis Consortium are the preparation of the data analysis algorithms, including astrometric, photometric, and spectroscopic data. DPAC is responsible for the generation and supply of simulated data to support the design, development and testing of the data processing system, the hardware and software processing environment, as well as the Gaia database and archive.

The Consortium is structured around specialized sub-units called Coordination Units (Fig. 2.4 and Table 2.1), each is responsible for a particular task of the overall Gaia data processing system. CUs develop the scientific algorithms and software, that later are run by one of the data processing centres (DPCs). These centres host the computing hardware and provide software engineering support to the CU, and each supports at least one CU.

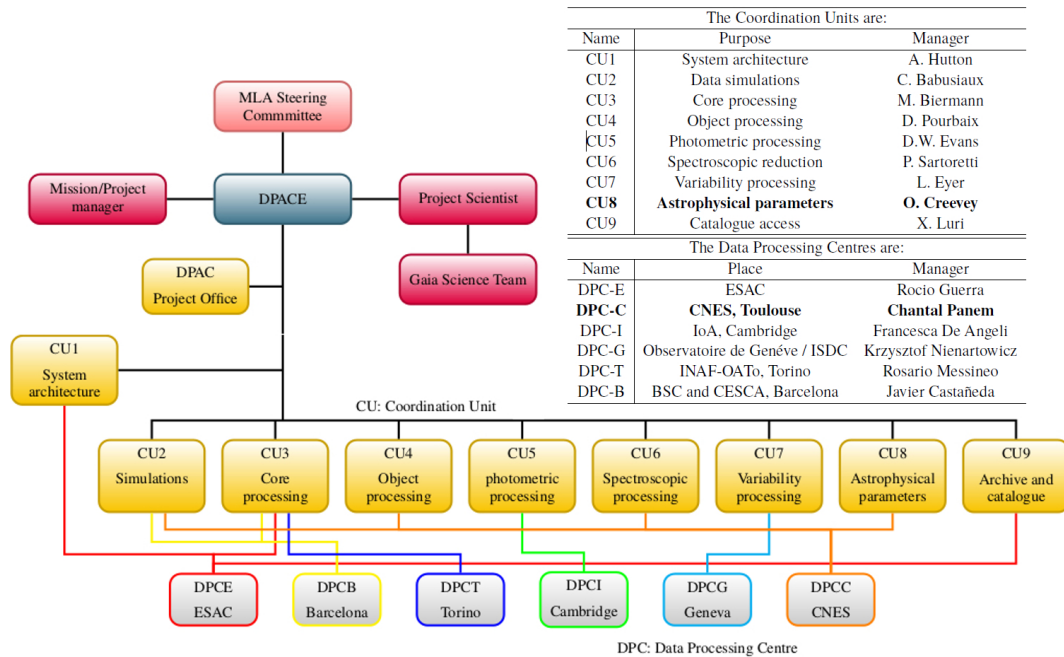


Figure 2.4: Coordinate Units separation in Gaia mission, more information can be found on the web-page <http://www.mpia.de/gaia/about/cus>

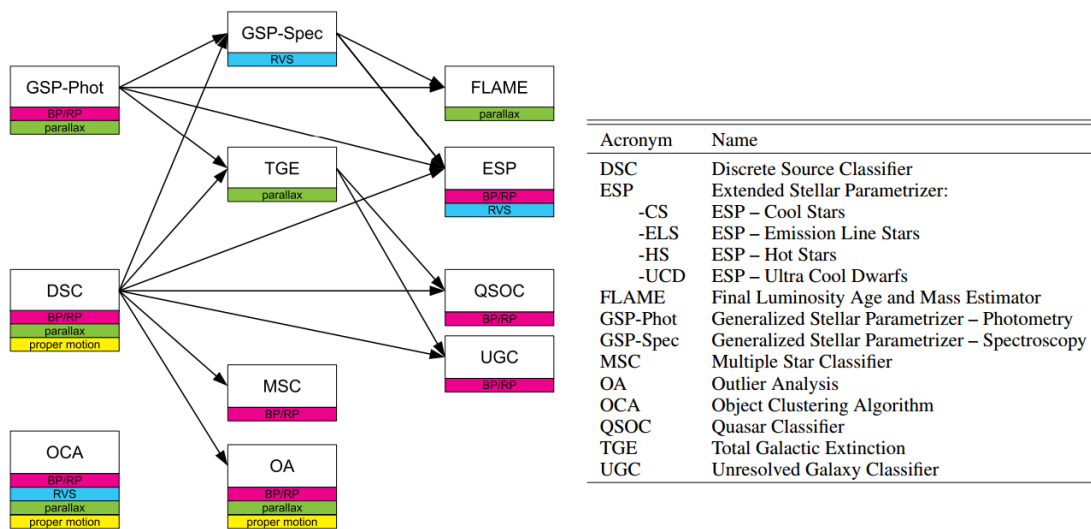


Figure 2.5: Component modules in Apsis and their interdependency. The module names are defined on the right panel. The arrows indicate a dependency on the output of the preceding module. The coloured bars underneath each module indicate which data it uses. Most of the modules additionally use the photometry and some also the Galactic coordinates. Credit: Bailer-Jones et al. (2013).

The Coordination Units are:		
Name	Purpose	Manager
CU1	System architecture	A. Hutton
CU2	Data simulations	C. Babusiaux
CU3	Core processing	M. Biermann
CU4	Object processing	D. Pourbaix
CU5	Photometric processing	D.W. Evans
CU6	Spectroscopic reduction	P. Sartoretti
CU7	Variability processing	L. Eyser
CU8	Astrophysical parameters	O. Creevey
CU9	Catalogue access	X. Luri

The Data Processing Centres are:		
Name	Place	Manager
DPC-E	ESAC	Rocio Guerra
DPC-C	CNES, Toulouse	Chantal Panem
DPC-I	IoA, Cambridge	Francesca De Angeli
DPC-G	Observatoire de Genève / ISDC	Krzysztof Nienartowicz
DPC-T	INAF-OATo, Torino	Rosario Messineo
DPC-B	BSC and CESCA, Barcelona	Javier Castañeda

Table 2.1: The list of the wavelengths of adopted MgI and YII lines. Left column represents the core wavelengths for each line, and the used for the abundance estimation wavelength ranges are included in other two columns.

2.3 CU8 and GSP-Spec

The coordinate unit eight CU8 Astrophysical Parameters, is in charge of the classification and the parametrization of the observed targets (Bailer-Jones et al., 2013). Eleven modules of analysis compose the global CU8 astrophysical parameters inference system (APSYS, see Fig. 2.5). In particular, the working group General Stellar Parametrizer – Spectroscopy (GSP-Spec) is responsible for the main parametrization of the RVS spectra (Recio-Blanco et al., 2016). To complement this GSP-Spec parametrization, other CU8 modules (Extended Stellar Parametrizer, ESP) will also estimate atmospheric parameters from RVS spectra of more specific types of stars as emission-line stars (ESP-ELS), hot stars (ESP-HS), cool stars (ESP-CS) and, ultra-cool stars (ESP-UCD) (Bailer-Jones et al., 2013). This thesis work has been partially developed in the framework of the CU8/GSP-Spec working group. In particular, the automatic algorithm of the determination of individual chemical abundances integrated in GSP-Spec has been optimized and tested (Chapter 4).

2.4 The Gaia data releases

2.4.1 First data release DR1

Gaia DR1 is based on observations collected between the 25 July 2014 and the 16 September 2015, e.g. during the first 14 months of Gaia's routine operational phase. Gaia DR1 was released on the 14th of September 2016. In this data release, positions (α , δ) and G-magnitudes for all sources (1 142 679 769 objects) with acceptable formal standard errors on positions are reported. The five-parameter astrometric solution – positions, parallaxes, and proper motions – for stars in common between the Tycho-2 Catalogue (Høg et al., 2000) and Gaia is contained (2,057,050 objects). This part of Gaia DR1 is called the Tycho-Gaia Astrometric Solution (TGAS, Michalik et al. (2015), Lindegren et al. (2016)), the first full-sky five parameters astrometric solution using Gaia data. Historically, the information from the HIPPARCOS catalog (Perryman et al. (1982), van Leeuwen (2007)) – the Hundred Thousand Proper Motions HTPM (Mignard, 2009) project – was thought to be used as the source of the improved proper motions for the Gaia mission. The big difference in time, 24 years between HIPPARCOS and the Gaia mission, allowed to detect interesting objects, for example, long-period astrometric binaries. Unfortunately, HTPM has a number of limitations, that requires the use of additional "auxiliary" stars Michalik et al. (2014). In this case, the full astrometric solution could be polluted by a potential bias, involved by these "auxiliary" stars. In the paper of Michalik et al. (2015) they have shown that the situation can be improved, if the full astrometric solution is solved using the Tycho-2 stars instead of "auxiliary" stars. Typical errors in parallax are 0.64 mas for 90% of all TGAS sources sources, including the subsets with a precision of 0.24 mas for 10% of the sources and 0.32 mas for 50% of the sources. Corresponding errors in proper motion are 0.72, 1.32 and 3.19 mas yr⁻¹ respectively. The additional systematic parallax error is about 0.3 mas.

Limitations.

The initial Gaia DR1 is not a complete survey. In particular, the source list is incomplete at the bright part ($G \leq 7$). All sources were treated as single stars without taking into account their radial velocities. Moreover, in dense areas of the sky (above some 400,000 stars per

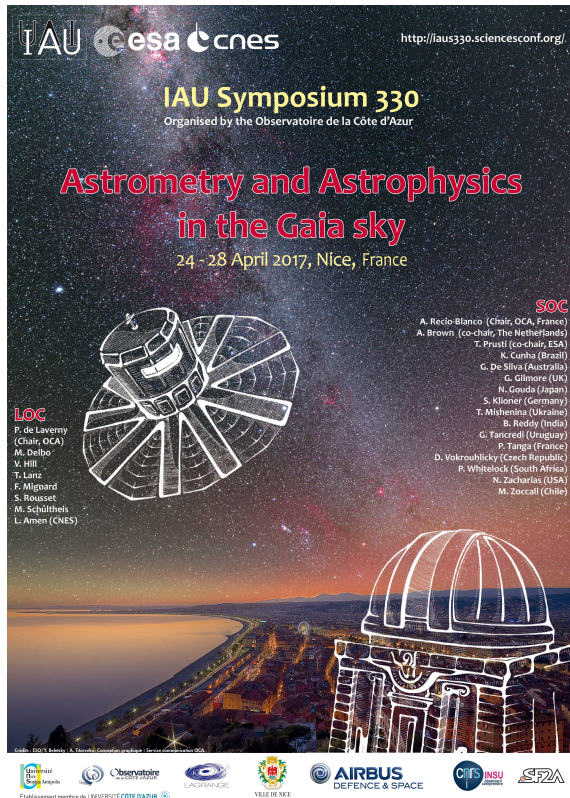


Figure 2.6: The poster of IAUS 330, "Astrometry and Astrophysics in the Gaia sky". Graphic credit: A. Titarenko. Concept: Y. Beletsky & OCA Communication service.

square degree) the reported magnitude limit of Gaia DR1 may be brighter by up to several magnitudes. Finally, the sources that are close to bright objects are sometimes missing as well as high proper motion stars ($\mu > 3.5$ arcsec yr⁻¹).

Contribution.

I have participated in the preparation of IAU Symposium 330, "Astrometry and Astrophysics in the Gaia sky", held in Nice in 2017. In particular, I created the graphic concept of Gaia and the grande coupole at OCA (Fig. 2.6). Lately, the concept was used for German postal-stamps as an advertisement of the Gaia mission.

2.4.2 Second data release DR2

Gaia DR2 data are based on observations collected between the 25th July 2014 and the 23th May 2016, covering a period of 22 months. It has been released the 25th April 2018.

The five-parameter astrometric solution – positions (α , δ), parallaxes, and proper motions – for more than 1.3 billion sources, with a limiting magnitude of $G = 21$ and a bright limit of $G \sim 3$ are reported. In the Gaia DR2 parallaxes and proper motions are based on Gaia data only and do no longer depend on the Tycho-2 Catalogue. For an additional set of more than 361 million sources, a two-parameter astrometric solution is also reported. It includes the positions on the sky (α , δ) combined with the mean G magnitude.

Parallax uncertainties reach 0.04 milliarcsecond for sources at $G < 15$, 0.1 mas for sources with $G = 17$, and 0.7 mas at $G = 20$. The corresponding uncertainties in the respective proper motion components reach 0.06 mas yr⁻¹ (for $G < 15$ mag), 0.2 mas yr⁻¹ (for $G = 17$ mag) and 1.2 mas yr⁻¹ (for $G = 20$ mag).

Median radial velocities for more than 7.2 million stars with a mean G magnitude between about 4 and 13 and an effective temperature in the range of about 3550 to 6900 K are reported. The overall precision of the radial velocities at the bright end reaches 200-300 m s⁻¹ while at the faint end the total precision reaches 1.2 km s⁻¹ for a $T_{eff} = 4750$ K and 2.5 km s⁻¹ for a $T_{eff} = 6500$ K.

GBP and GRP magnitudes for more than 1.38 billion sources, with precisions varying from a few milli-mag at the bright ($G < 13$) end to around 200 milli-mag at $G = 20$ are reported. Additionally, a classification for more than 550,000 variable sources consisting of Cepheids, RR-Lyrae, Mira and Semi-Regular Candidates, High-Amplitude δ Scuti, BY Draconis candidates, SX Phoenicis Candidates and short time scale phenomena is reported.

The effective temperatures estimation is reported for more than 161 million sources brighter than 17th magnitude with effective temperatures in the range 3000 to 10 000 K. For a subset of about 87 million sources also the line-of-sight extinction A_G and reddening E (from BP-RP instruments) are given. For part of this subset (around 76 million sources) the luminosity and radius estimations are available.

Limitations.

The Gaia DR2 catalogue is essentially complete between $G = 12$ and $G = 17$. Although the completeness at the bright end ($G \leq 7$) has improved, it still has some problems with the

faint magnitude limit.

The completeness near bright sources and for high proper motion stars have significantly improved with respect to Gaia DR1. In dense areas of the sky (above some 400,000 stars per square degree) the magnitude limit of Gaia DR2 is now $G = 18$.

No radial velocity determination is available for objects identified as emission-line stars and detected double-lined spectroscopic binaries. Single-lined spectroscopic binaries have been treated as single stars and only a median radial velocity is provided.

The values of T_{eff} , extinction A_G , radius, and luminosity were determined only from the three broad-band photometric measurements and the parallax. A strong degeneracy between T_{eff} and extinction/reddening when using the broad band photometry exists.

Contribution.

As a DPAC CU8 member, I am a co-author of 6 papers on Gaia DR2. [Gaia Collaboration et al. \(2018b\)](#) is one of the main papers, consisting on the contents summary and survey properties. The other papers are performance verification articles: [Gaia Collaboration et al. \(2018a\)](#) is about observational Hertzsprung-Russell diagrams, [Mignard et al. \(2018\)](#) is dedicated to the celestial reference frame, [Gaia Collaboration et al. \(2018e\)](#) is about the observations of solar system objects, [Gaia Collaboration et al. \(2018d\)](#) mapping the Milky Way disk kinematics, and finally, [Gaia Collaboration et al. \(2018c\)](#) describes kinematics of globular clusters and dwarf galaxies around the Milky Way.

2.4.3 Future DR3+

As it was mentioned before, the next Gaia catalogue will be published at the end of 2020. This will be definitively the stellar catalogue that will play a central role for many varied fields of astronomy. It will contain the full astrometric solution (positions, distances and motions) and photometric data (brightness and color) for over one billion stars. As an extension, object classification and astrophysical parametrisation, together with BP/RP spectra and/or RVS spectra they are based on, will be released for spectroscopically and spectro-photometrically data. It will also include non-variable stars with available atmospheric-parameter estimates, variable stars, multiple stellar systems and exoplanet-hosting stars. For more than 150 million stars the radial velocities will be released.

The next Gaia data release DR3 will be first release of products for the CU8/GSP-Spec module of the DPAC APSIS pipeline.

2.5 Summary

This thesis is developed in the framework of the Gaia DPAC consortium, in particular to optimize the abundance estimation capabilities of the GSPspec module. In addition, the arrival of the first Gaia astrometric data has started the observational revolution of the Galactic Archaeology studies. In this thesis work the Gaia DR1 astrometric measurement were exploited to study the possible use of a particular chemical abundance ratio $[Y/Mg]$ as a stellar

age estimator. To this purpose complementary high-resolution spectroscopic data from the AMBRE project (Chapter 3) were used.

As shown in the Fig. 2.7, adapted from Gilmore (2012), the complementary use of Gaia and ground based spectroscopic data allows to explore the complete vision of the galactic stellar populations.

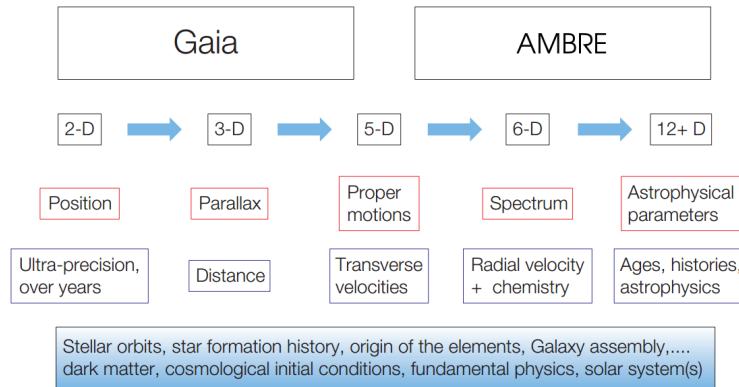


Figure 2.7: Diagrammatic representation of the outputs of the Gaia and AMBRE databases, showing how they are complementary. Adapted from: Gilmore et al. (2012)

Building up the AMBRE-TGAS catalogue

Contents

3.1	The AMBRE project	26
3.2	Procedures	26
3.2.1	<i>Object identification: search radius</i>	27
3.2.2	<i>Object identification: estimated photometric temperatures</i>	27
3.2.3	<i>Object identification: comparison of object names</i>	27
3.2.4	<i>Object identification: quality labels</i>	28
3.2.5	<i>Additional flags for post-cross-match validation</i>	28
3.3	AMBRE HARPS	29
3.4	AMBRE UVES	33
3.5	AMBRE FEROS	36
3.6	Summarizing different instruments: the total AMBRE catalogue	40
3.7	The AMBRE – TGAS catalogue	43

At the epoch of big spatial projects, such as Gaia, the ground-based observations are still playing an important role. In particular, high-resolution spectroscopic observations, covering a large wavelength domain, are important complement for Gaia data. Moreover, the huge amount of high-resolution spectroscopic data, collected from different ground-based instruments during the last years, is archived and available in open access. A clear example of this is the ESO archive advanced data products. In this thesis, the capabilities of the ESO archival data were exploited, analysing the AMBRE project (de Laverny et al., 2013). This huge amount of the data requires a homogeneous treatment, in order to extract from the results the highest precision level. In particular, this chapter is dedicated to the analysis of the stellar coordinates for the different ground-based spectroscopic data. Its goal is the improvement of the existing catalogue thanks to a homogeneous objects identification, capable to overcome the challenges of the complexity of a data base that is build up from archive data.

3.1 The AMBRE project

The AMBRE Project is the analysis of high-resolution archival ESO spectra, as described in [de Laverny et al. \(2013\)](#). It contains a uniform parametrization of spectra taken from three ESO spectrographs: HARPS (up to $R = 115\,000$, [Mayor et al. \(2003\)](#)), FEROS (up to $R = 48\,000$, [Kaufer et al. \(1999\)](#)), and UVES (up to $R = 110\,000$, [Dekker et al. \(2000\)](#)). This allows to use these homogeneously analysed datasets in the framework of galactic archaeology studies. The synthetic spectral grid of AMBRE is generated from MARCS model atmospheres ([Gustafsson et al., 2008](#)), in a range of metallicities $[\text{Fe}/\text{H}]$ from -5.0 dex to $+1.0$ dex, alpha abundances $[\alpha/\text{Fe}]$ from -0.4 dex to $+0.8$ dex, effective temperatures T_{eff} from 2500 K to 8000 K, and surface gravities $\log(g)$ from -0.5 dex up to 5.5 dex. Thus, accurate stellar parameters can be determined for different stellar types, covering the entire HR-diagram. Within AMBRE stellar atmospheric parameters are derived using the MATISSE algorithm ([Recio-Blanco et al., 2006](#)), and the full description is presented in [De Pascale et al. \(2014\)](#) for the HARPS instrument, [Worley et al. \(2012\)](#) for FEROS, and [Worley et al. \(2016\)](#) for UVES.

To analyse and properly homogenise the catalogue, a check of each target coordinates has to be performed. To this purpose, the 2MASS catalogue ([Skrutskie et al., 2006](#)) was chosen as a reference for a coordinate cross-match due to its advantage in photometric information for each target. Later, the identified stars were also searched in the Tycho-Gaia Astrometric Solution (TGAS, [Michalik et al. \(2015\)](#), part of the first Gaia data release). The tests described below in this chapter were done independently from the previous published results about the AMBRE data. The presented results constitute a new precise identification of the whole AMBRE catalogue and for each instrument separately. The observational periods for the datasets are given below in the following order: instrument, modified julian date, day-month-year in brackets:

instrument	modified julian date		day-month-year	
HARPS	52936.038	55471.412	24-10-2003	02-10-2010
UVES	51616.27891065	55501.38837811	13-03-2000	01-11-2010
FEROS	53646.1328125	55194.3671875	03-10-2005	29-12-2009

3.2 Procedures

The automatic procedure *find2mass* (CDS client in Strasbourg) was used for performing the object identification with the 2MASS catalogue by coordinate comparison. The cross-match between the AMBRE and the Tycho-2 catalogues was performed with the *xcross* program (developed by Mathias Schultheis). The idea behind both of the methods is the search of a number of objects from the 2MASS and Tycho-2 catalogues that are located inside a circle

with a given radius. The central point of the circle has the coordinates of right ascension RA and declination DEC for the object from the AMBRE catalogue.

3.2.1 *Object identification: search radius*

There is no sharp criteria to define the radius of search, but a combination of factors can give a prompt. First, the knowledge about the initial precision for each set of AMBRE (HARPS, UVES, FEROS) coordinates gives an indication. Second, a threshold value can be empirically defined by increasing the search radius until the number of unique solutions reaches a maximum. Then a sub-sample of identified stars can be analysed to study the distribution of differences between the 2MASS-coordinates and initial AMBRE coordinates (those from the header of the spectra fits file). This distribution is fitted with a Gaussian in order to obtain a 2σ value, that is finally defined as the optimal search radius.

3.2.2 *Object identification: estimated photometric temperatures*

The search procedure performed by the comparison between the 2MASS-coordinates with the AMBRE ones within a chosen search radius can be resulted in multiple-identifications for a single AMBRE object. For this reason, an additional procedure of check should be carried out, and a comparison of the effective temperatures from the AMBRE catalogue and the corresponding estimated photometric temperatures can provide additional information. For each match from the 2MASS catalogue, the effective photometric temperature was calculated using the formula of [Alonso et al. \(1996b\)](#) and constants from [González Hernández and Bonifacio \(2009\)](#): $\theta = a_0 + a_1X + a_2X^2 + a_3X^3 + a_4X[\text{Fe}/\text{H}] + a_5[\text{Fe}/\text{H}] + a_6[\text{Fe}/\text{H}]^2$, where $\theta = 5040/T_{\text{eff}}$, X is the color ($J - K$). The constants in the equation are different for giants and dwarfs, so the AMBRE catalogue value of $\log(g) = 3.5$ dex was adopted as a threshold value to separate the populations. If no estimation of the metallicity is available in the catalogue, then a solar value of the iron abundance was used. If no surface gravity information is presented in the AMBRE catalogue, then this object was accepted as a dwarf. Finally, the $|T_{\text{phot}} - T_{\text{AMBRE}}|$ difference was used to constrain the AMBRE-2MASS cross-match.

3.2.3 *Object identification: comparison of object names*

Among other things, the AMBRE catalogue provides the "object name" entry for each spectrum inside its header information. This identification can be used as an additional parameter together with the described above in order to improve the identification between the AMBRE and the 2MASS catalogues. First, the list of object names from the AMBRE catalogue was checked using the Simbad database. The coordinates differences $\Delta\text{RA} = \text{RA}_{\text{SIMBAD}} - \text{RA}_{\text{INSTRUMENT}}$ and $\Delta\text{DEC} = \text{DEC}_{\text{SIMBAD}} - \text{DEC}_{\text{INSTRUMENT}}$ were checked and reported for the final cross-match.

3.2.4 *Object identification: quality labels*

The quality of the stars identification can be evaluated according to the precision of the match with the 2MASS catalogue. To perform this correctly, the separation in two groups was assumed: the spectra with available T_{eff} , $\log(g)$ and $[M/H]$ in the first group, and the spectra which have only T_{eff} values in a separate group. Another level of quality evaluation can be defined by the number of matches during the search-radius procedure: spectra that have a single identification from the 2MASS catalogue, and those with an initial multiple-identification within the radius of search. Finally, a last level of quality comes from the comparison between the AMBRE effective temperature and the corresponding calculated photometric T_{eff} from 2MASS (see Sect. 3.2.2). A threshold for the value of temperature difference was defined by propagating the mean errors in T_{AMBRE} and T_{phot} : $\Delta T_{\text{eff}}^2 < T_{\text{AMBRE-mean-error}}^2 + T_{\text{phot-mean-error}}^2$, where $\Delta T = T_{\text{phot}} - T_{\text{AMBRE}}$, where $T_{\text{AMBRE-mean-error}}$ is the mean error given in the AMBRE catalogue, and $T_{\text{phot-mean-error}}$ is the mean analytical error calculated for the photometric temperature.

For practical purposes, a threshold of $\Delta T < 2\sigma$ was assumed. Finally, the following quality labels were adopted:

- quality 1 – unique matches, AMBRE T_{eff} , $\log(g)$ and $[M/H]$ available, the difference $\Delta T \leq 2\sigma$;
- quality 2 – unique matches, AMBRE T_{eff} , $\log(g)$ and $[M/H]$ available, the difference $\Delta T > 2\sigma$;
- quality 3 – multiple matches, AMBRE T_{eff} , $\log(g)$ and $[M/H]$ available;
- quality 4 – matches for which the AMBRE T_{eff} exist, but $\log(g)$ and $[M/H]$ are unavailable.

3.2.5 *Additional flags for post-cross-match validation*

Once the spectrum is associated with a given 2MASS source following the above described procedures, an additional verification was performed taking into account all available physical parameters. For all the spectra with the same 2MASS-name the median values and standard deviations were calculated for the set of the AMBRE parameters: radial velocity, effective temperature, logarithm of surface gravity and metallicity. A threshold value of each parameter was selected as the 85th quantile of the distribution. Following this selection, a set of additional quality flags was accepted for each spectrum: if all the above described parameters lie inside the selected 85th quantile of the distribution, then the individual spectrum was marked as "good"; if at least one of the parameters is going outside, the "bad" flag is selected. If for the 2MASS-name there is only one corresponding spectrum, this spectrum was marked as "uniq". When only two spectra were associated to the same 2MASS name, both of them were marked as "2spectra". The spectra with no available values of surface gravity and metallicity were marked as "neutral".

3.3 AMBRE HARPS

The precision of the HARPS coordinates allows to perform a quite simple direct cross-match with the 2MASS catalogue (Fig. 3.1 & 3.2). The cross-match was tested for radii of search from 1 to 10 arcsec with a step of 1 arcsec. The value of 5 arcsec was finally adopted as the good one following the criteria described in Sect. 3.2.1. Figure 3.1 shows the number of results with a single match as a function of the search radius. The value of 5 arcsec corresponds to the maximum of the curve. The comparison of effective temperatures between AMBRE and the photometrically derived one (Sect 3.2.2) was performed.

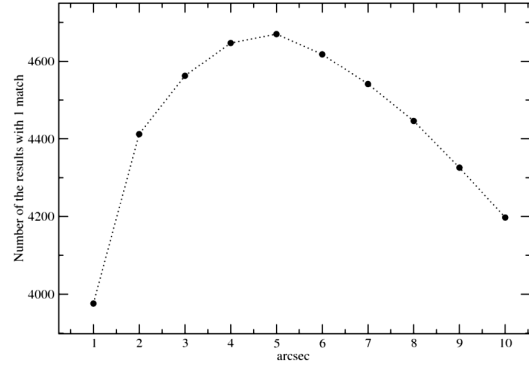


Figure 3.1: The distribution of the number of unique matches within a search radius area for the HARPS data.

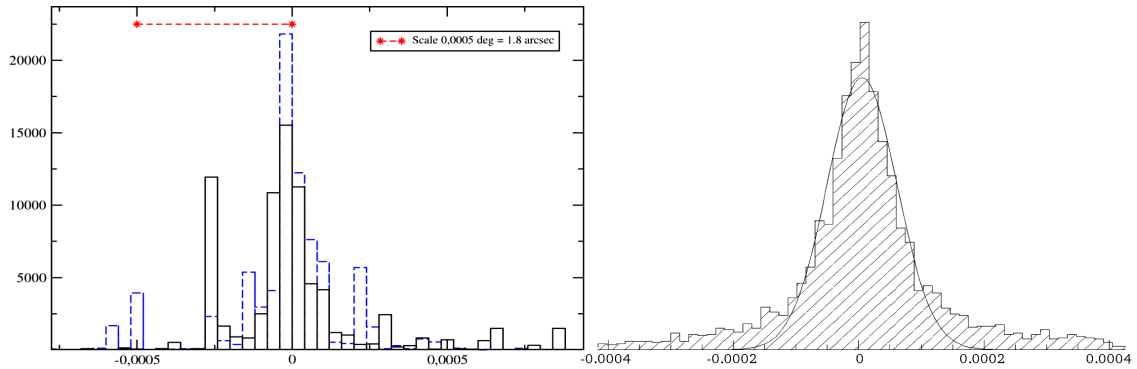


Figure 3.2: On the left: the histogram of the difference between the coordinates from 2MASS and AMBRE HARPS. The blue dotted line indicates the difference in DEC, the solid black one indicates the difference in RA. On the right: the histogram of the difference between the RA-coordinates from 2MASS and AMBRE HARPS for the result of a 5 arcsec. The histogram is fitted by a normal distribution (solid line) with a value of $\sigma = 0.36$ arcsec.

The final following quality labels were adopted (Sect 3.2.4):

- quality 1 – single match, AMBRE estimations of T_{eff} , $\log(g)$ and $[M/H]$ exist, the difference ΔT between calculated T_{phot} and T_{AMBRE} is inside $[-400;400]$ K (Fig. 3.3);
- quality 2 – single match, AMBRE estimations of T_{eff} , $\log(g)$ and $[M/H]$ exist, the difference ΔT is out of the above mentioned range;
- quality 3 – multiple match (2 matches), AMBRE estimations of T_{eff} , $\log(g)$ and $[M/H]$ exist;
- quality 4 – the AMBRE T_{eff} estimation exists, but $\log(g)$ and $[M/H]$ are unavailable.

The criteria for "quality label 1" matches implies that $\Delta T_{\text{eff}}^2 < T_{\text{AMBRE-mean-error}}^2 + T_{\text{phot-mean-error}}^2$. The AMBRE errors from HARPS are of 93 K, the mean error from the photometric estima-

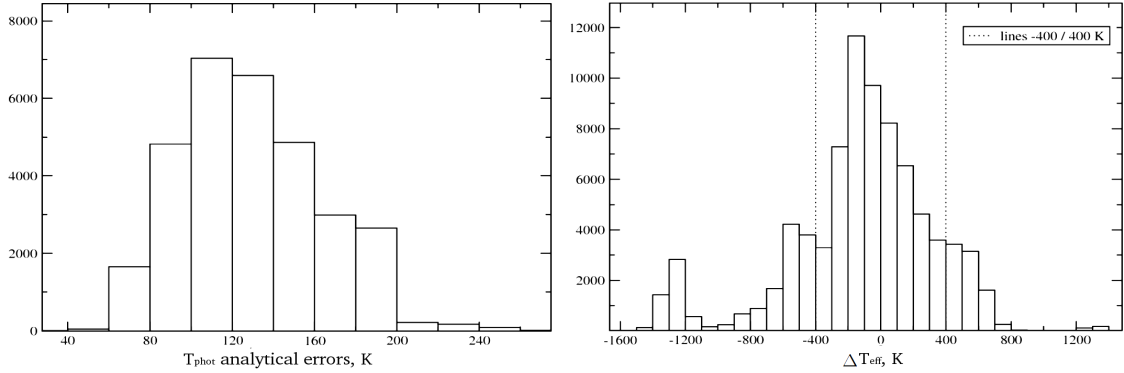


Figure 3.3: AMBRE HARPS. On the left: the histogram (20K bin) of the photometric temperature errors, the maximum is around 130 K. On the right: the distribution (100 K bin) of ΔT_{eff} . The dotted lines indicate the 2σ threshold used for the quality label1.

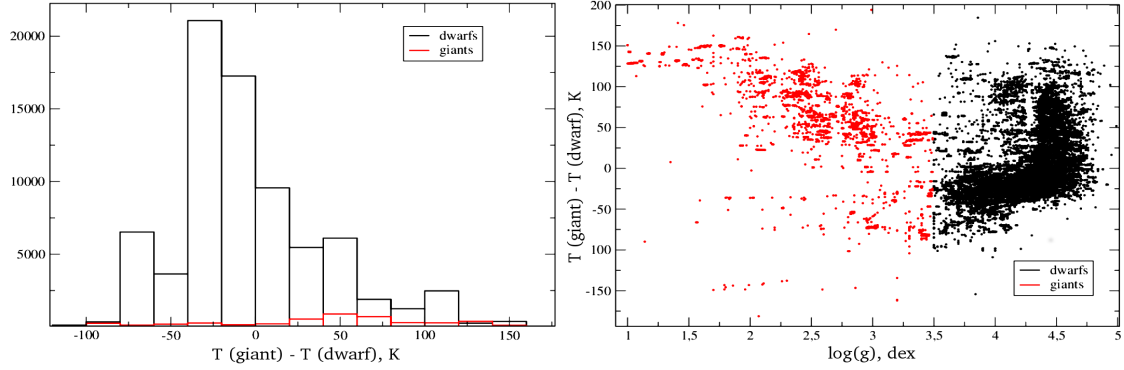


Figure 3.4: AMBRE HARPS. On the left: the distribution of the differences between the photometric temperatures of giants and dwarfs ($T_{\text{giants}} - T_{\text{dwarfs}}$), width of the bin is 20 K. On the right: the dependence between this difference and the surface gravity $\log(g)$.

tions is 130 K (see Fig. 3.3), therefore, $\Delta T_{\text{eff}} \sim 160$ K. The level of $2\sigma = 400$ K was adopted.

To check the possible error of the calculated photometric temperatures for a star with no estimation of its surface gravity, both the giant and dwarf equations were used for each entry of AMBRE HARPS (Sect. 3.2.2). The Fig. 3.4 shows, that this distribution is not going out of the ± 100 K value. That confirms the assumption, given in the Sect. 3.2.2, that the AMBRE stars without any estimation of surface gravity can be assumed to be dwarfs for the purpose of the cross-match. Additionally, the HR-diagram and the dependence of the $[\alpha/\text{Fe}]$ with stellar metallicity are presented for individual spectra of AMBRE HARPS (Fig. 3.5), and the distribution of the stellar positions and the dependence of the color ($J - K$) with K -magnitude are presented for the AMBRE HARPS stars (Fig. 3.8).

In order to associate post-cross-match flags (Sect. 3.2.5), the distributions of T_{eff} , $\log(g)$, v_{radial} and $[\text{M}/\text{H}]$ for each stars with multiple spectra were used. The level of 85% of the distribution corresponds to 100 K the effective temperature distribution, radial velocity to

5 km/s, logarithm of surface gravity to 0.15 dex, metallicity to 0.06 dex (Fig. 3.6 & 3.7).

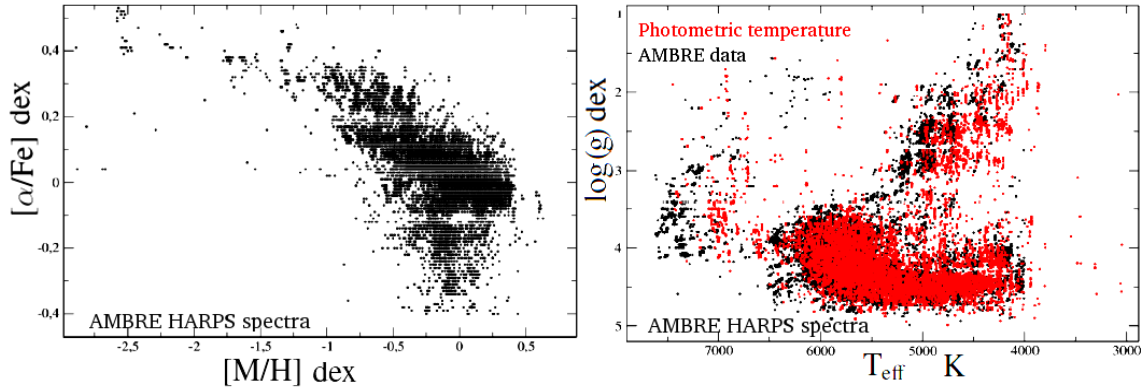


Figure 3.5: HARPS AMBRE data. On the left: dependence of the α -element abundances $[\alpha/\text{Fe}]$ related to iron versus stellar metallicity $[\text{M}/\text{H}]$. On the right: the dependence of the surface gravity $\log(g)$ with the effective temperature T_{eff} .

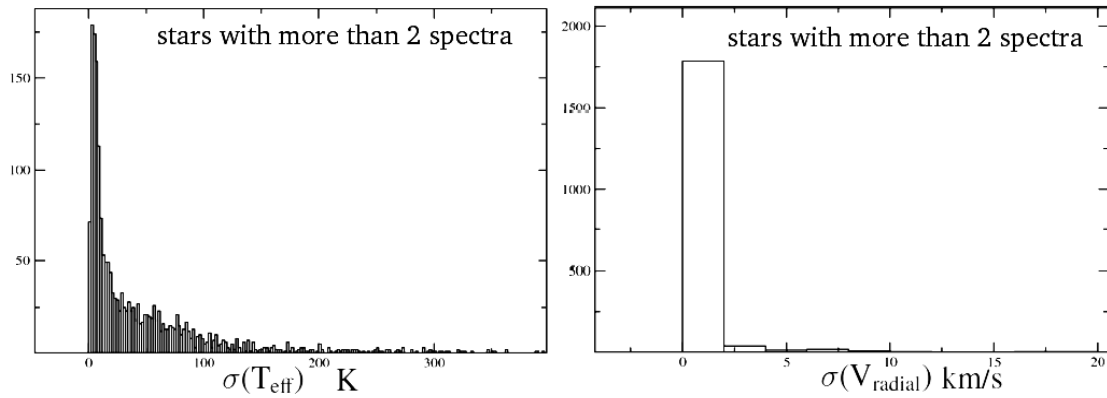


Figure 3.6: The distributions of the standard deviations of the effective temperature $\sigma(T_{\text{eff}})$ on the left and radial velocity $\sigma(V_{\text{radial}})$ on the right for AMBRE HARPS. The threshold values are 100 K and 5 km/s.

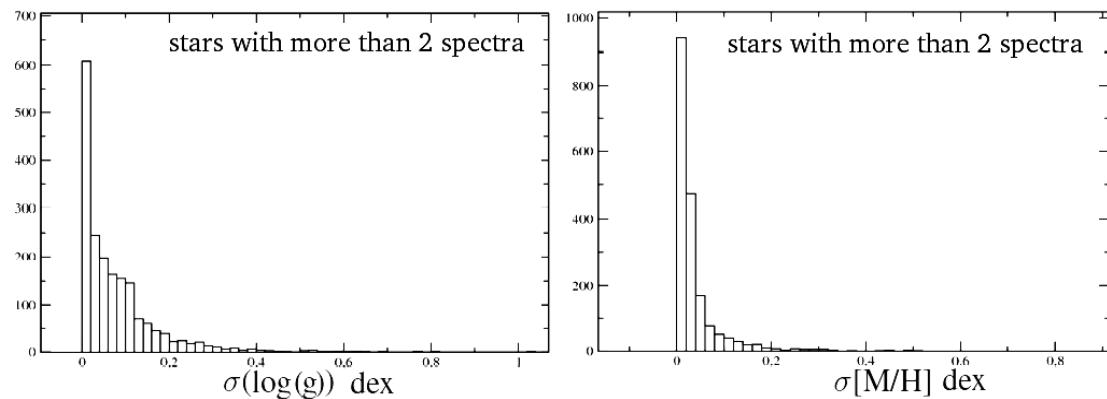


Figure 3.7: The distributions of the standard deviations of the surface gravity $\sigma(\log(g))$ on the left and the metallicity $\sigma[\text{M}/\text{H}]$ on the right for AMBRE HARPS. The threshold values are 0.15 dex and 0.061 dex.

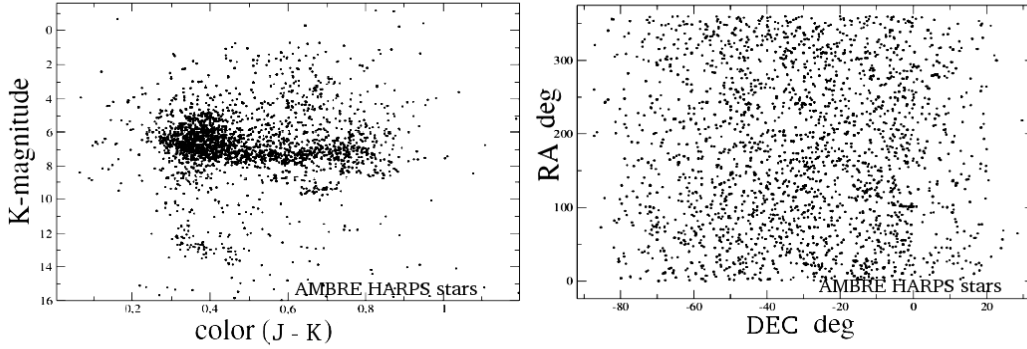


Figure 38: HARPS AMBRE data. On the left: the dependence of $(J - K)$ with K-magnitude. On the right: the distribution of the object coordinates from the 2MASS-catalog, presented in right ascension RA and declination DEC.

The AMBRE_HARPS 126688 spectra (**93116 with T_{eff}**)

5 arcsec \sim 80420 spectra totally			
quality	$N_{spectra}$	Mean (ΔT_{eff}), K	$\sigma(\Delta T_{eff})$, K
1	54270	-24	199
1 + 2	79900	-119	409
3	515	-71	168

For the rest spectra identification was done with the complementary 20 arcsec search, the number of non-validable results in this case \sim 12150 spectra.

Totally \sim 92570 spectra (99%) = 2416 different objects
 \sim 54270 'qual 1' spectra (58%) = 2129 different objects

2MASS-name verification

(number of spectra that common for the flag and qual1 given in the brackets)
 $flag = N_{spectra}$: good = 71750 (47820), uniq = 430 (310), neutral = 0 (0),
 bad = 19802 (5642), 2spectra = 581 (0), nothing = 548 (0)

qual = 1 - 1 match, all data + $|\Delta T_{eff}|$ from [-400;400] K
 qual = 2 - 1 match, all data + $|\Delta T_{eff}|$ out of this area
 qual = 3 - n matches, all data
 qual = 4 - no met no $\log(g)$

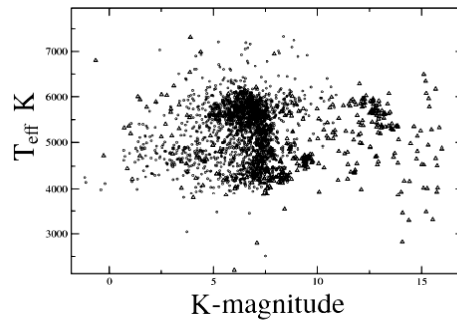


Figure 3.9: The dependence of the effective temperature T_{eff} with the K-magnitude for AMBRE HARPS.

3.4 AMBRE UVES

As for the HARPS catalogue, the precision of the coordinates from the UVES catalogue allows to perform a good enough cross-match with 2MASS (Fig. 3.10 & 3.11).

shows the number of results with single match as the function of a search radius. The value of 5 arcsec corresponds to the maximum of the curve.

Again, the cross-match was tested for radii of search from 1 to 10 arcsec within a step of 1 arcsec. Fig. 3.10 shows the number of results with a single match as a function of the search radius. The value of 4 arcsec corresponds to the maximum of the curve. The comparison of effective temperatures between AMBRE and the photometrically derived one (Sect 3.2.2) was performed.

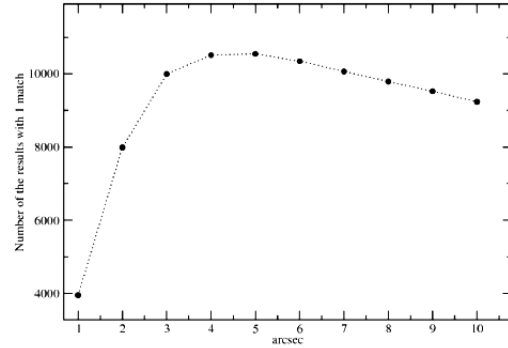


Figure 3.10: The distribution of the number of unique matches within a search radius area for the UVES data.

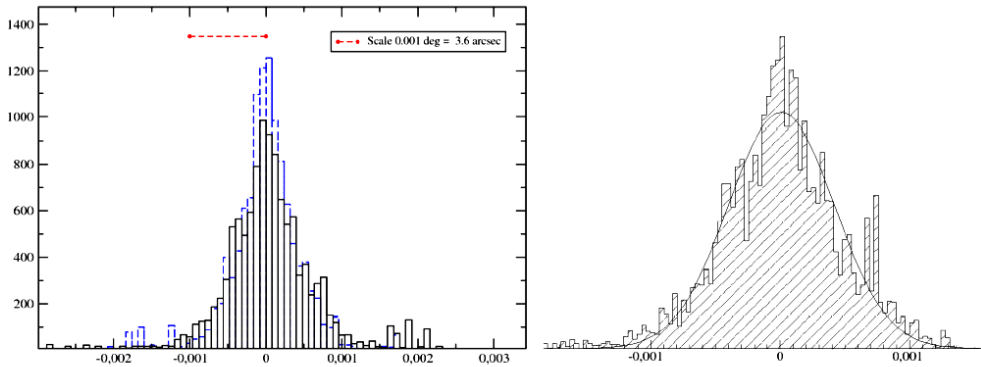


Figure 3.11: On the left: the histogram of the difference between the coordinates from 2MASS and AMBRE UVES. The blue dotted line indicates the difference in DEC, the solid black one indicates the difference in RA. On the right: the histogram of the difference between the RA-coordinates from 2MASS and AMBRE UVES, the result from 4 arcsec search with the 2MASS catalogue. The histogram is fitted by the normal distribution (solid line) with a value of $\sigma = 1.44$ arcsec.

The final following quality labels were adopted (Sect 3.2.4):

- quality 1 – single match, AMBRE T_{eff} , $\log(g)$ and $[M/H]$ exist, the difference ΔT between calculated $T_{\text{photometric}}$ and initial T_{AMBRE} inside $[-500;500]$ K (Fig. 3.12);
- quality 2 – single match, AMBRE T_{eff} , $\log(g)$ and $[M/H]$ exist, the difference ΔT is out of the above mentioned range;
- quality 3 – multiple match (2 matches), AMBRE T_{eff} , $\log(g)$ and $[M/H]$ exist;
- quality 4 – the AMBRE T_{eff} exists, but $\log(g)$ and $[M/H]$ are unavailable.

The criteria for "quality label 1" implies that:

$\Delta T_{\text{eff}}^2 < T_{\text{AMBRE-mean-error}}^2 + T_{\text{phot-mean-error}}^2$. The AMBRE errors from UVES are 198 K, the mean error from the photometric estimations is 150 K (Fig. 3.12), therefore, $\Delta T_{\text{eff}} \sim 250$ K. A threshold of $2\sigma = 500$ K was adopted (Fig. 3.13).

In order to associate post-cross-match flags of the 2MASS-name, the distributions of T_{eff} , $\log(g)$, v_{radial} and $[M/H]$ for each star with multiple spectra were used (Sect. 3.2.5). The level 85% for effective temperature distribution corresponds to 490 K, radial velocity to 5 km/s, logarithm of surface gravity to 0.44 dex, metallicity to 0.30 dex (Fig. 3.13 & 3.14).

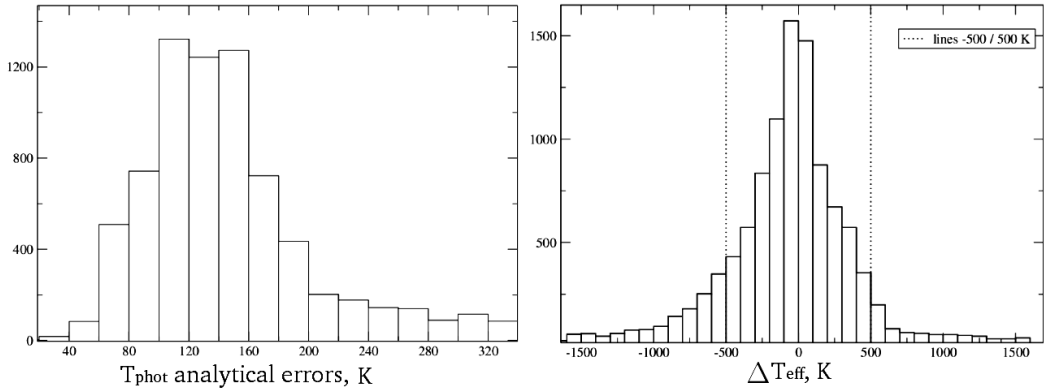


Figure 3.12: The distribution (20K bin) of the errors in the photometric temperatures T_{phot} for AMBRE UVES, the maximum is around 150 K (on the left). The distribution (100K bin) of ΔT_{eff} for AMBRE UVES. The dotted lines show the threshold of 2σ (on the right).

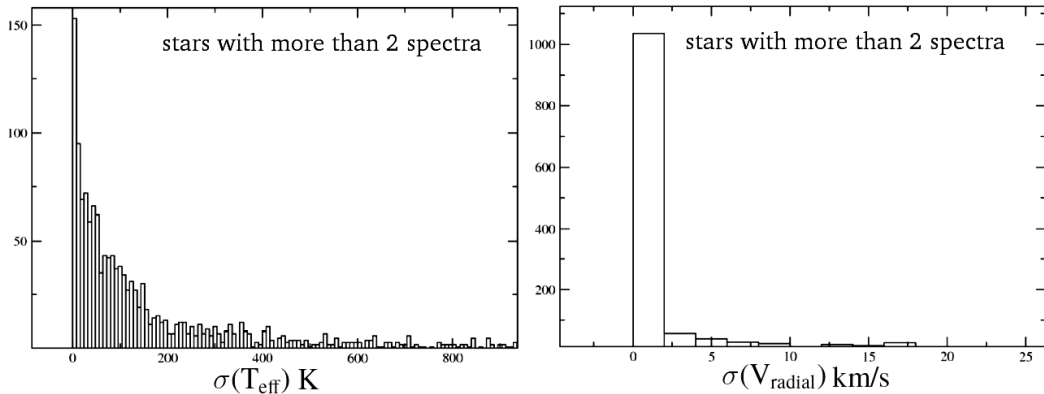


Figure 3.13: The distributions of the standard deviations of the effective temperature $\sigma(T_{\text{eff}})$ on the left and radial velocity $\sigma(V_{\text{radial}})$ on the right for AMBRE UVES. The threshold values are 490 K and 5 km/s.

The HR-diagram and the dependence of the $[\alpha/\text{Fe}]$ with stellar metallicity are presented for individual spectra of AMBRE UVES on the Fig. 3.15, and the distribution of the stellar positions and the dependence of the color ($J - K$) with K -magnitude are presented for the AMBRE UVES stars on the Fig. 3.16.

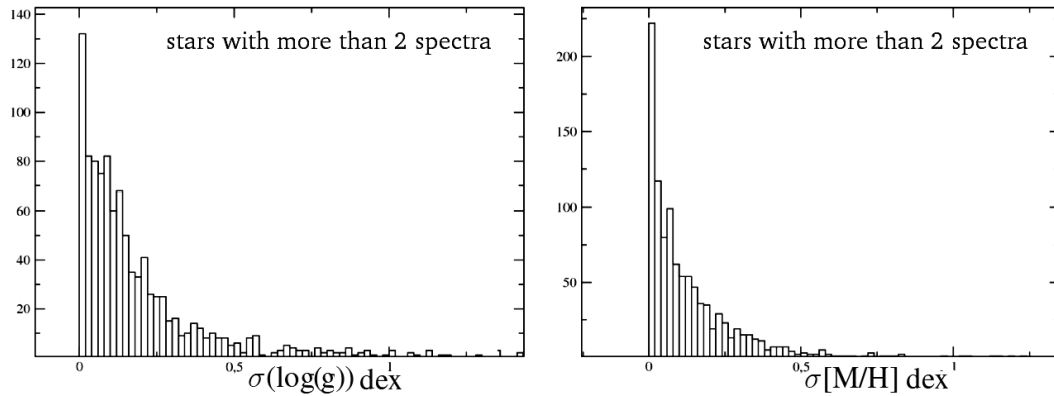


Figure 3.14: The distributions of the standard deviations of the surface gravity $\sigma(\log(g))$ on the left and the metallicity $\sigma[M/H]$ on the right for AMBRE UVES. The threshold values are 0.44 dex and 0.304 dex.

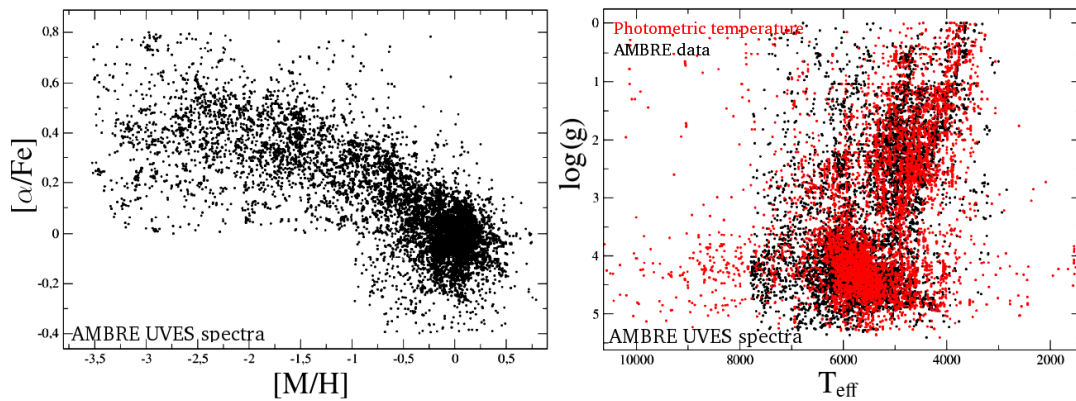


Figure 3.15: AMBRE UVES. On the left: the dependence of the α -element abundances $[\alpha/Fe]$ related to iron versus stellar metallicity $[M/H]$. On the right: the dependence of the surface gravity $\log(g)$ with the effective temperature T_{eff} .

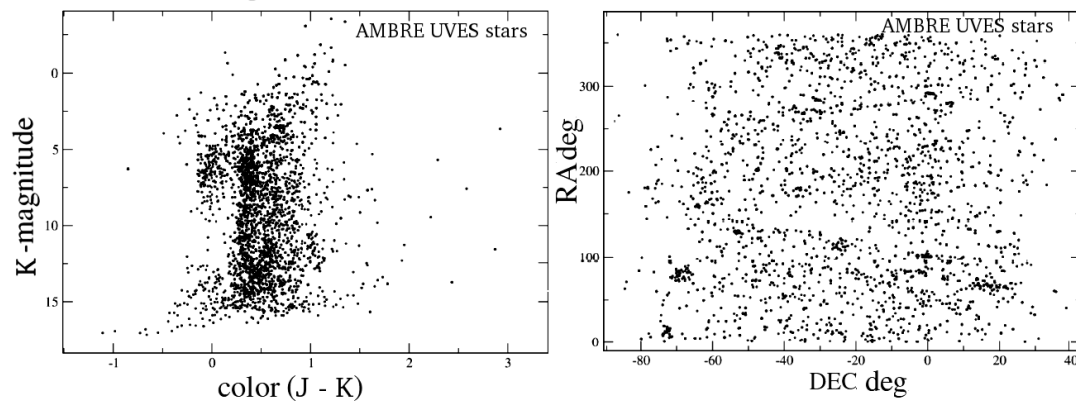


Figure 3.16: AMBRE UVES. On the left: the dependence of $(J - K)$ with the K-magnitude. On the right: the distribution of the coordinates from the 2MASS-catalog, presented in right ascension RA and declination DEC.

The AMBRE_UVES 51921 spectra (12403 with T_{eff})

4 arcsec \sim 10610 spectra totally			
quality	$N_{spectra}$	Mean (ΔT_{eff}), K	$\sigma(\Delta T_{eff})$, K
1	6850	-37	214
1 + 2	8846	-72	348
3	111	-171	285
4	1650	533	1319

For the rest spectra identification was done with the complementary 10 arcsec search, the number of non-validable results in this case \sim 920 spectra.

Totally \sim 11530 spectra (92%) = 2456 different objects
 \sim 6850 'qual 1' spectra (55%) = 1425 different objects

2MASS-name verification

(number of spectra that common for the flag and qual1 given in the brackets)

$flag = N_{spectra}$: good = 5813 (4574), unqi = 813 (435), neutral = 1700 (0),
 bad = 2550 (1476), 2spectra = 647 (372), nothing = 875 (0)

qual = 1 - 1 match, all data + $|\Delta T_{eff}|$ from [-750;750] K

qual = 2 - 1 match, all data + $|\Delta T_{eff}|$ out of this area

qual = 3 - n matches, all data

qual = 4 - no met no $\log(g)$

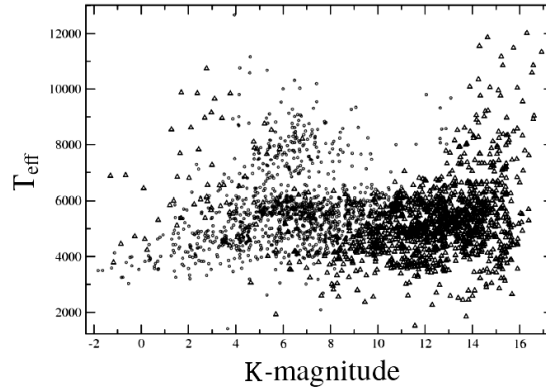


Figure 3.17: The dependence of the effective temperature T_{eff} with the K-magnitude the for AMBRE UVES.

3.5 AMBRE FEROS

The direct cross-match of the FEROS coordinates with the 2MASS catalogue, described above in case of HARPS and UVES, gave non-realistic results: K-magnitudes fainter than the 13 magnitude were mainly obtained, which is not possible for the FEROS-spectrograph, mounted on 2.2-meters telescope. The reason is an important shift in right ascension RA for the FEROS instrument (Fig. 3.18). Firstly, the coordinates were corrected for a shift $\Delta RA = 0.02$ deg. Then, using the AMBRE information about the object name, these coordinates were compared to the Simbad ones for a sub-sample of objects to confirm the validity

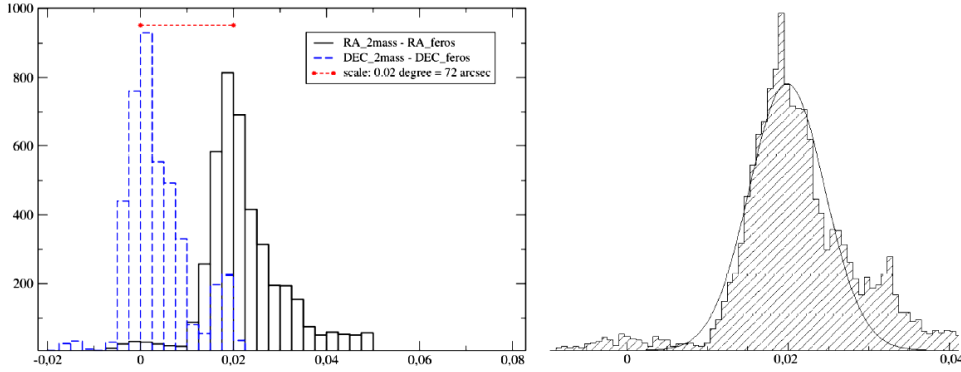


Figure 3.18: On the left: the histogram of the difference between the coordinates from 2MASS and FEROS. The blue dotted line shows the difference in DEC, the solid black one shows the difference in RA. On the right: the histogram of the difference between the RA-coordinates from 2MASS and the AMBRE FEROS ones. The histogram is fitted by the normal distribution (the solid line) with a value of $\sigma = 18$ arcsec.

of the procedure.

After this first adjustment of the coordinates, the cross-match using a radius of search from 1 to 5 arcsec with a 1 arcsec step was carried out. The value of 3 arcsec was adopted, following the criteria of maximizing the number of unique matches. Finally, the following quality labels were adopted (Sect 3.2.4):

- quality 1 – single match, AMBRE T_{eff} , $\log(g)$ and $[M/H]$ exist, the difference ΔT between calculated $T_{\text{photometric}}$ and initial T_{AMBRE} is inside $[-500;250]$ K (Fig. 3.19);
- quality 2 – single match, AMBRE T_{eff} , $\log(g)$ and $[M/H]$ exist, the difference ΔT is out of the above mentioned range;
- quality 3 – multiple match (2 matches), AMBRE T_{eff} , $\log(g)$ and $[M/H]$ exist;
- quality 4 – the AMBRE T_{eff} exists, but $\log(g)$ and $[M/H]$ are unavailable.

The level of the quality label was chosen as:

$\Delta T_{\text{eff}}^2 < T_{\text{AMBRE-mean-error}}^2 + T_{\text{phot-mean-error}}^2$, where $T_{\text{AMBRE-mean-error}}$ is 120 K for FEROS. The mean error of the photometric effective temperatures (the peak of the distribution) is 130 K (left) and 80 K (right) (Fig. 3.19). Therefore, $\Delta T_{\text{eff}} \sim 180$ K (left) and 150 K (right). The level of $2\sigma = 400$ K for the left border and 300 K for the right border was adopted (Fig. 3.19).

In order to put the post-cross-match flags of the 2MASS-name for each spectrum, the distributions of T_{eff} , $\log(g)$, v_{radial} and $[M/H]$ were used (Sect.3.2.5). The level 85% for effective temperature distribution corresponds to 115 K, radial velocity to 5 km/s, logarithm of surface gravity $\log(g)$ to 0.13 dex, metallicity to 0.06 dex (Fig. 3.20 & 3.21).

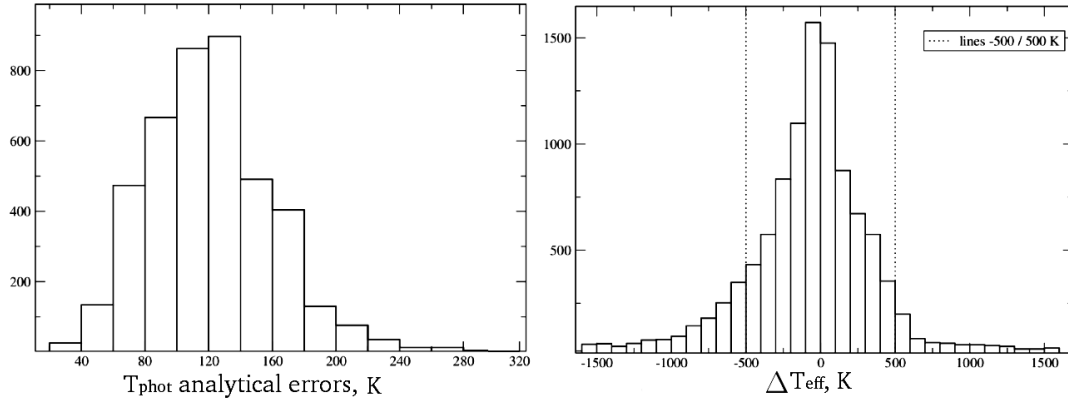


Figure 3.19: The distribution (20 K bin) of the errors in the photometric temperatures T_{phot} for AMBRE FEROS, the maximum is around 130 K (on the left). The distribution (100 K bin) of the errors in the effective temperatures T_{eff} for AMBRE FEROS, the dotted lines show the threshold of 2σ (on the right.)

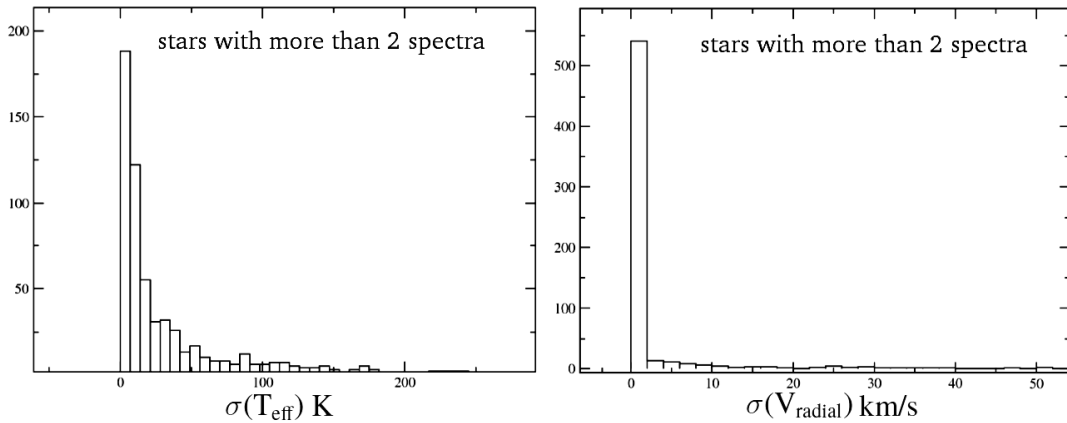


Figure 3.20: The distributions of the standard deviations of the effective temperature $\sigma(T_{\text{eff}})$ on the left and radial velocity $\sigma(V_{\text{radial}})$ on the right for AMBRE FEROS. The threshold values are 115 K and 5 km/s.

The HR-diagram and the dependence of the $[\alpha/\text{Fe}]$ with stellar metallicity are presented for individual spectra of AMBRE FEROS on the Fig. 3.22, and the distribution of the stellar positions and the dependence of the color ($J - K$) with K -magnitude are presented for the AMBRE FEROS stars on the Fig. 3.23.

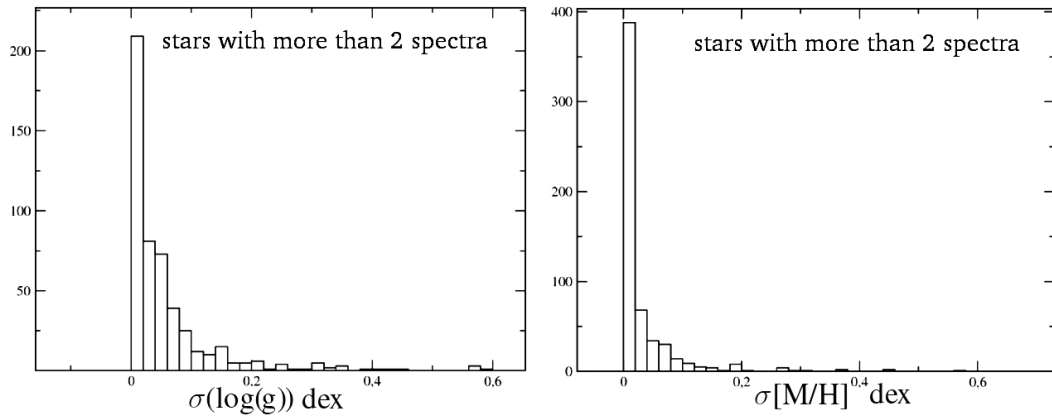


Figure 3.21: Distributions of the standard deviations of the logarithm of the surface gravity $\sigma(\log(g))$ on the left and metallicity $\sigma[M/H]$ on the right for FEROS AMBRE data. The threshold values are 0.13 dex and 0.065 dex.

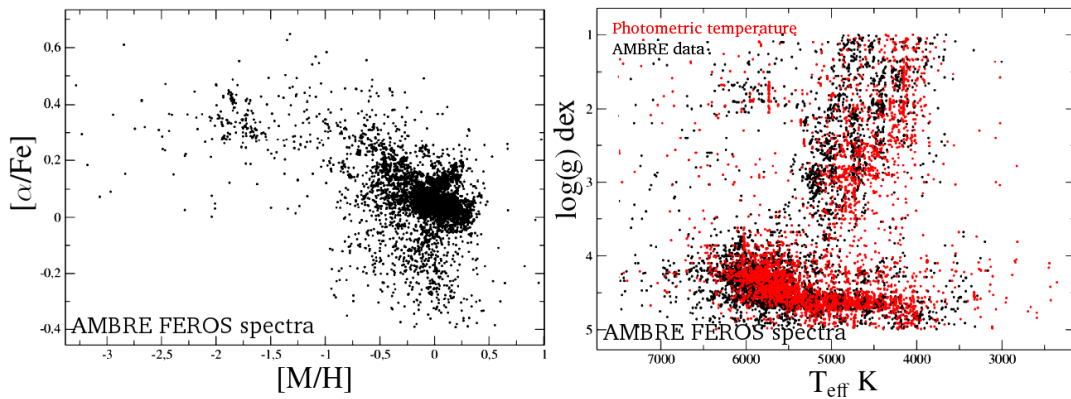


Figure 3.22: AMBRE FEROS. On the left: the dependence of the α -element abundances $[\alpha/Fe]$ related to iron versus stellar metallicity $[M/H]$. On the right: the dependence of the surface gravity $\log(g)$ with the effective temperature T_{eff} .

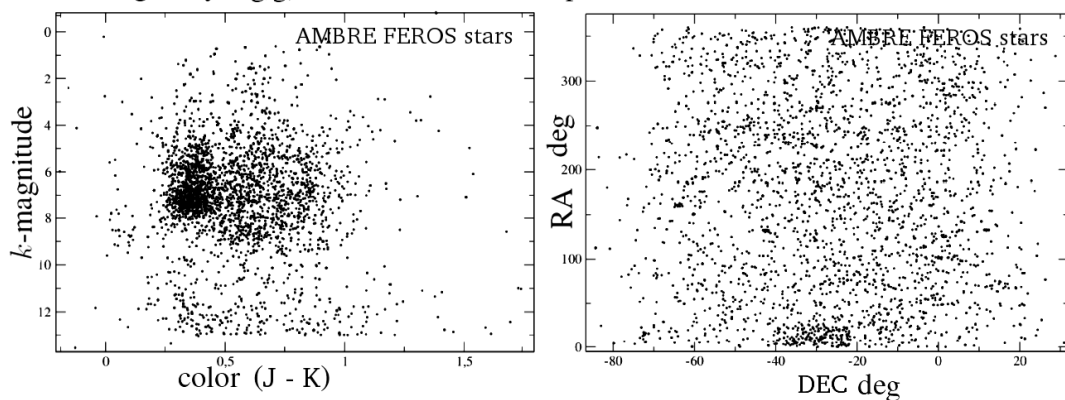


Figure 3.23: AMBRE FEROS. On the left: the dependence of $(J - K)$ with the K-magnitude. On the right: the distribution of the object coordinates from the 2MASS-catalog, presented in right ascension RA and declination DEC.

The AMBRE_FEROS 21551 spectra (6508 with T_{eff})

4940 spectra with T_{eff} have 'object names' that exist in Simbad
The sample with $|\Delta| < 0.05$ deg consist of $N_{spectra} \sim 4450$ (1994 diff objects)

3 arcsec \sim 4430 spectra totally
(the coordinates adopted from Simbad were used)

quality	$N_{spectra}$	Mean (ΔT_{eff}), K	$\sigma(\Delta T_{eff})$, K
1	3670	-147	178
1 + 2	4260	-187	241
4	167	-385	1116

For the rest spectra identification was done with the complementary 36 arcsec search,
the number of non-validable results in this case \sim 1235 spectra.

Totally \sim 5665 spectra (87%) = 2789 different objects
 \sim 3670 'qual 1' spectra (56%) = 1632 different objects

2MASS-name verification
(number of spectra that common for the flag and qual given in the brackets)

flag = $N_{spectra}$: good = 2226 (1710), uniq = 1978 (1176), neutral = 301 (0),
bad = 520 (339), 2spectra = 635 (448), nothing = 843 (0)

qual = 1 - 1 match, all data + $|\Delta T_{eff}|$ from [-550;250] K
qual = 2 - 1 match, all data + $|\Delta T_{eff}|$ out of this area
qual = 3 - n matches, all data
qual = 4 - no met no log(g)

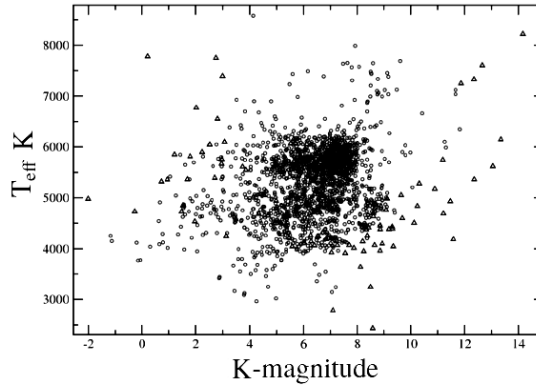


Figure 3.24: The dependence of the effective temperature T_{eff} with the K-magnitude for AMBRE FEROS.

3.6 Summarizing different instruments: the total AMBRE catalogue

The AMBRE catalogue, based on the spectroscopic data from the HARPS, UVES and FEROS instruments, contains the parametrisation of 200160 spectra, and 112027 spectra of them (about 56%) have estimations of the effective temperature T_{eff} . Its identification with the 2MASS catalogue covers 6776 individual stars, corresponding to a total number of 109765 spectra from the AMBRE catalogue, at least parametrised with the effective temperature value. In other words, the 97.9% of the parametrised spectra, that exist in the AMBRE cata-

logue, have associated coordinates from the 2MASS catalogue.

Additionally, the stars in common between the different individual AMBRE catalogues, was analysed. It equals to 456 stars between FEROS and HARPS, 240 stars between HARPS and UVES and 262 stars between FEROS and UVES. The number of stars, that is common for all the three instruments, equals to 97 objects. These numbers are summarised in the table below.

The AMBRE (HARPS+UVES+FEROS) contains 200160 spectra (112027 with T_{eff})

Total number of identified objects: 6776
Corresponding to 109765 spectra with T_{eff} (97.9 %)

Number of objects in common for
 FEROS and HARPS = 456, HARPS and UVES = 240, UVES and FEROS = 262
 Objects in common for the three datasets = 97

Figures 3.25 & 3.26 show the distribution of coordinates RA_{2MASS} and DEC_{2MASS} and color-magnitude distribution for 6776 stars, identified with the 2MASS catalogue. Figures 3.27 & 3.28 show the HR-diagram and $[\alpha/Fe]$ with metallicity dependence for 109758 individual spectra from the total AMBRE catalogue, that were associated with the objects from the 2MASS catalogue by the comparison of the coordinates. Table 3.1 gives the format of the different columns, provided in the final catalogue.

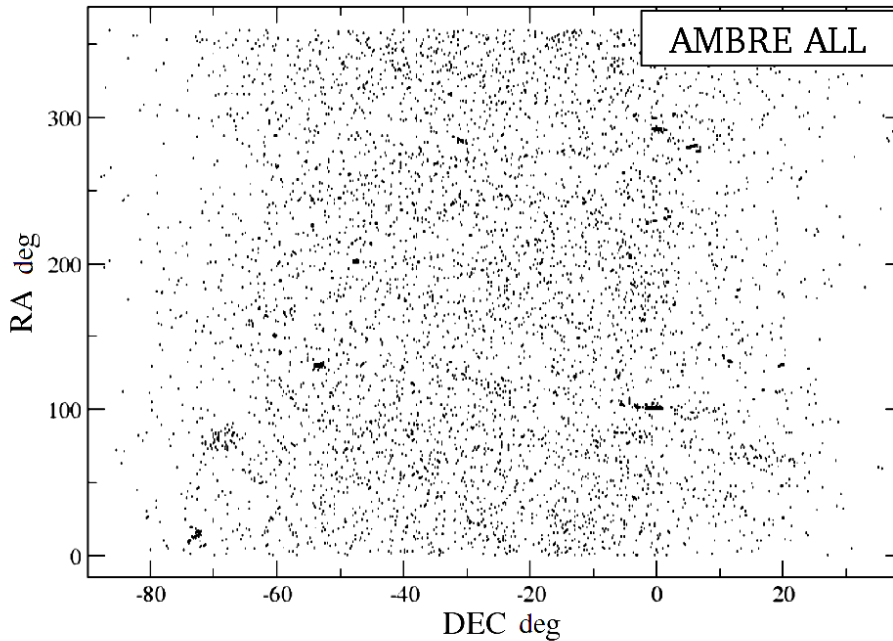


Figure 3.25: The RA-DEC distribution for the total AMBRE catalog.

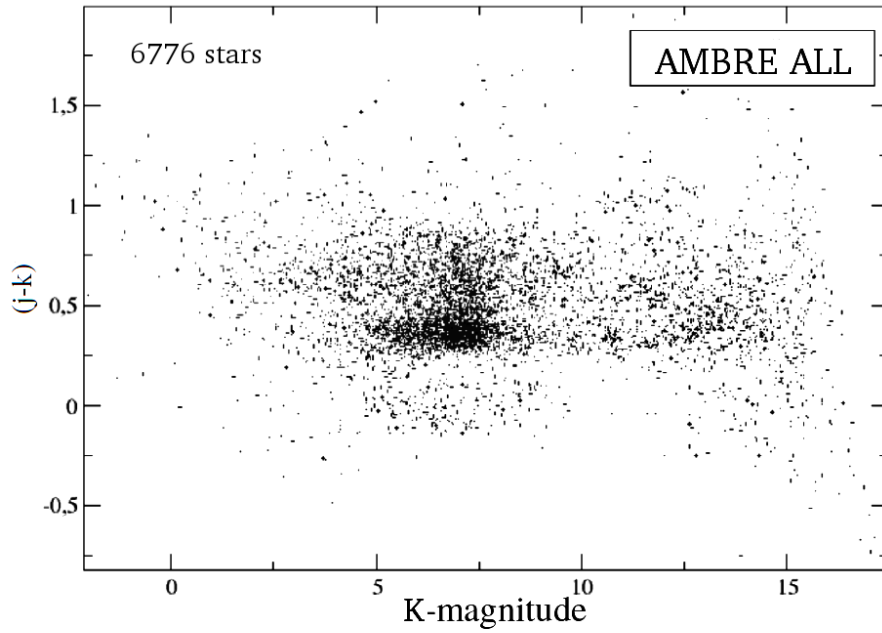


Figure 3.26: The color-magnitude dependence $(j-k)$ vs K-magnitude for the total AMBRE catalog.

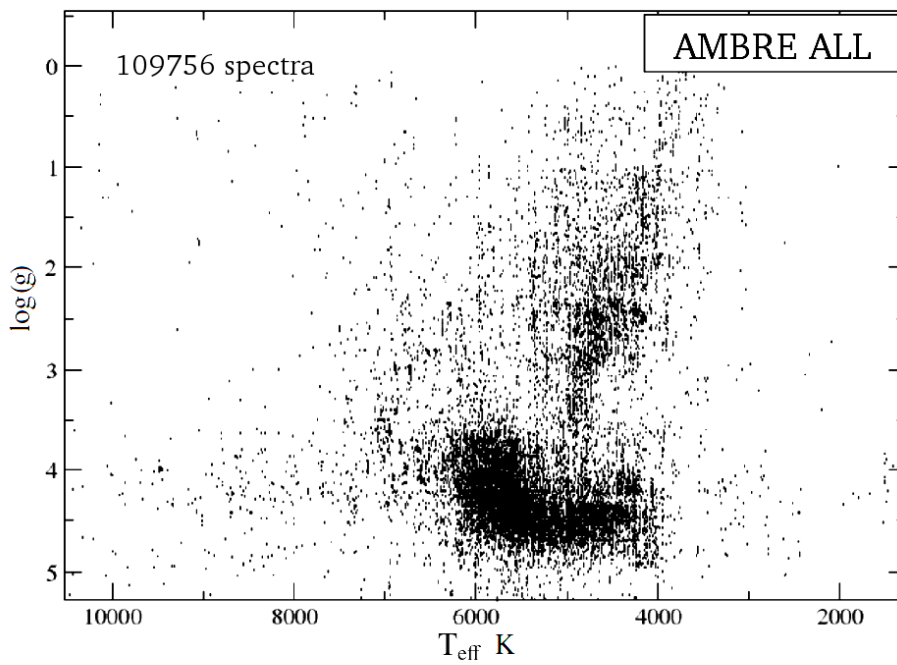


Figure 3.27: HR-diagram for the total AMBRE catalog.

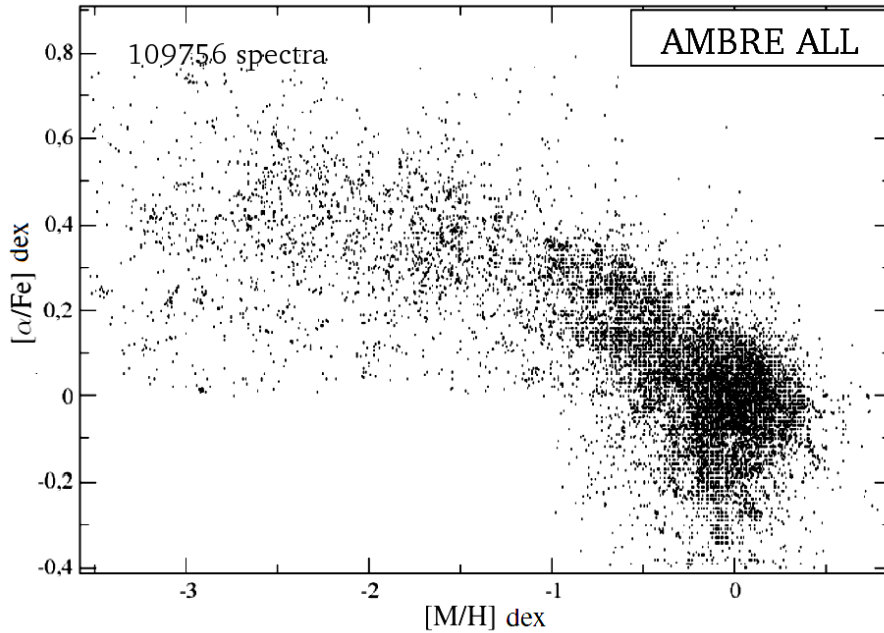


Figure 3.28: The $[\alpha/\text{Fe}]$ vs metallicity dependence for the total AMBRE catalog.

3.7 The AMBRE – TGAS catalogue

The Tycho-Gaia astrometric solution (TGAS, [Michalik et al. \(2015\)](#)) is the first full-sky five parameters astrometric solution, provided in the first Gaia data release ([Lindergren et al., 2016](#)), see Chapter 2. It is a joint solution, solved through the use of the Tycho-2 stars ([Høg et al., 2000](#)) as an additional source of high astrometric data, complementing the data from the Gaia mission.

The TGAS catalogue is 99% complete to magnitudes of $V = 11$ ([Høg et al., 2000](#)). Thus, the AMBRE catalogue can have an overlap with TGAS in its bright part. As an example, figure 3.29 represents the sample of the stars that are in common for three analysed AMBRE datasets (97 objects). Their K-magnitude distribution shows a maximum around $K = 5$. The cross-match between the final AMBRE sample and TGAS covers 1919 stars from the HARPS dataset, 1567 stars from FEROS, and 750 stars from UVES. Totally 2521 stars with precise atmospheric parameters are reported.

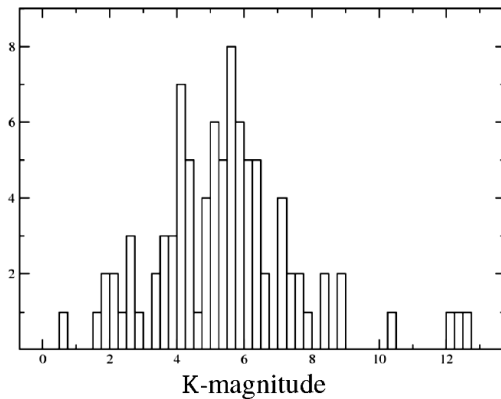


Figure 3.29: The distribution of the K-magnitudes for the objects that are common for all three datasets.

Description of final file with the AMBRE-data. The capital letters are the data from the initial AMBRE catalogue.
 The file consists of the data for spectra with available initial T_{eff} -estimation
 FEROS, UVES – all columns, HARPS – all except *-marked

Col_name	Description
DP_ID	Spectrum name
RAJ2000	RA-coordinate from the AMBRE, deg
DEJ2000	DEC-coordinate from the AMBRE, deg
MJD_OBS	Modified julian date of observations
EXPTIME	Exposition time, sec
SNR	Signal-to-noise ratio
* SNR_F	Signal-to-noise ratio flag
* EXEM_F	Extreme emission line flag
* EM_F	Emission line flag
* MEANFWHM	Mean FWHM lines, Angstrom
* FWHM_F	Mean FWHM lines flag
VRAD	Vrad, km/s
ERR_VRAD	Errors Vrad, km/s
VRAD_CCF	Vrad CCF FWHM, Angstrom
VR_F	Vrad flag
TEFF	Effective temperature, K
ERR_TEFF	Total error of effective temperature, K
LOGG	Logarithm of gravity, cm/sec ²
ERR_LOGG	Total error of logarithm of gravity, cm/sec ²
M_H	Metal abundance, dex
ERR_M_H	Total error of metal abundance, dex
ALPHA	Abundance of alpha-elements, dex
ERR_ALPHA	Total error of abundance of alpha-elements, dex
CHI2	χ^2
CHI2_F	χ^2 flag
ra2mass	RA-coordinate for associated object from the 2MASS catalogue, deg
dec2mass	DEC-coordinate for associated object from the 2MASS catalogue, deg
2mass_id	2MASS-identifier for associated object from the 2MASS catalogue
n_matches	The number of matches for object from the AMBRE in the 2MASS catalogue
jmag	J-magnitude from the 2MASS catalogue
err_jmag	Total error of J-magnitude
hmag	H-magnitude from the 2MASS catalogue
err_hmag	Total error of H-magnitude
kmag	K-magnitude from the 2MASS catalogue
err_kmag	Total error of K-magnitude
Tphot	Effective temperature, calculated from (j-k) color and metallicity, K
err_Tphot	Analytical error of effective temperature calculated from (j-k) color and metallicity, K
Tphot-Tam	The difference between calculated T_{eff} and initial one, K
qual	Quality label
pm1	Proper Motion in $RA \cdot \cos(DEC)$, mas/year
erpm1	Mean error in $pmRA \cdot \cos(DEC)$, mas/year
pm2	Proper Motion in Dec, mas/year
erpm2	Mean error in $pmDe$, mas/year
prlx	Parallax, mas
er_prlx	Standard error in Parallax, mas
ra_tycho	RA-coordinate for associated object from the Tycho-2 Catalogue, deg
dec_tycho	DEC-coordinate for associated object from the Tycho-2 Catalogue, deg
UVES_SETUP	UVES-setup (just for AMBRE.UVES-data)
flag	veracity of the 2mass-identification

Table 3.1: The format of the different columns, provided in the final catalog.

The GAUGUIN – automatic method of stellar abundance determination: optimization and tests

Contents

4.1	The models of stellar atmospheres	46
4.2	Overview of stellar abundance determination – methods "on the fly" . . .	46
4.2.1	<i>Automatic methods using synthetic profile fitting</i>	46
4.2.2	<i>Automatic methods using equivalent width fitting</i>	47
4.3	Pre-calculated grid – the GAUGUIN method	47
4.4	Interpolation on the parameter grid	49
4.5	Normalization of the spectra	52
4.6	Visualisation	54
4.7	Summary	55

Gaia performs the spectroscopic observation of several hundreds of millions of stars (Recio-Blanco et al. (2016), Gaia Collaboration et al. (2016b), Gaia Collaboration et al. (2016a)) thanks to the spectroscopic RVS instrument. This chapter is dedicated to the method of chemical abundance determination in stellar atmospheres, used by the Gaia mission DPAC and later in this thesis work. In order to measure stellar abundances from RVS spectra in automatic or semi-automatic mode, the method, based on the GAUGUIN algorithm (Bijaoui (2012), Guiglion (2015), Guiglion et al. (2016)), was re-coded into the *java* programming language, adapted and optimized. The first integration of the algorithm into the Gaia interface was done before the arrival of the first real Gaia RVS data (in Sept 2017). That allowed the GSP-Spec module to run on the APSIS validation platform for cycles 2&3 (Sect. 2.2). Its testing and optimization were performed using the AMBRE HARPS dataset (Sect. 3.3) in high resolution.

4.1 The models of stellar atmospheres

Stellar atmosphere models allow to produce theoretical stellar spectra by solving the equations of radiative transfer through stellar atmosphere. The individual chemical abundances can then be estimated by comparison of the observed stellar spectra with the corresponding modelled ones for a given set of atmospheric parameters. It can be realised by measuring equivalent widths or by the fitting of the observed lines with the synthetic profile.

At the epoch of big spectroscopic projects, from ground based (Gaia-ESO Survey, RAVE, APOGEE...) observations or from space (Gaia RVS), the development of automatic procedures to estimate the stellar chemical abundances is crucial. For big datasets, the measurement of chemical abundances based on (1) a measurement of an equivalent width of spectral lines or (2) the comparison of the spectral profiles between an observed and a synthetic spectrum can be realised in two different ways: based on a pre-calculated grid, or using an analysis "on the fly".

4.2 Overview of stellar abundance determination – methods "on the fly"

These methods can be separated in two groups: first, the fit of the profile of the observed spectral line with a synthetic one, and second, the a fit of the equivalent width of the observed spectra with theoretical ones. These two approaches are based on the minimisation of the distance χ^2 between the observed spectral line and the calculated synthetic one, when varying the theoretical chemical abundance. At each step, the χ^2 is calculated between the observed and the synthetic profiles in a narrow area of wavelength $\Delta\lambda$, centred at the core of the observed line λ_0 . The final abundance is derived when the χ^2 takes the minimal value. These methods are based on optimisation algorithms, either by direct χ^2 -minimisation, either by more complex algorithms.

4.2.1 Automatic methods using synthetic profile fitting

One of the basic methods that represents this approach is SME "Spectroscopy Made Easy" (Valenti and Piskunov, 1996). Within this routine the determination of both the rotation velocity $v \sin i$ and the individual chemical abundances is possible. Each synthetic profile is generated from the radiative transfer equations under the assumption of local thermal equilibrium, based on the SYNTH code (Piskunov, 1992). The atmosphere models come from the interpolation on the MARCS grid (Gustafsson et al. (2008)). The χ^2 -minimisation is realised through the method, described in W. Marquardt (1963). Another method, that is similar in its realisation, was realised by Blanco-Cuaresma et al. (2014) and it is named iSpec, and has four available radiative transfer codes: TURBOSPECTRUM (Plez, 2012), SPECTRUM Gray (1999), SYNTH (Piskunov, 1992) and MOOG (Snedden, 1973).

Another method of this category is the [Mikolaitis et al. \(2014\)](#) one, for which the spectral profiles are generated on the fly using the TURBOSPECTRUM code ([Plez, 2012](#)) under the assumption of local thermal equilibrium, and atmosphere models are calculated from a linear interpolation on the MARCS grid ([Gustafsson et al., 2008](#)). Two methods, developed by [Van der Swaelmen et al. \(2013\)](#) and [Posbic et al. \(2012\)](#) (SPADES), include the creation of a one-dimensional grid of synthetic spectra for each spectral line for each star.

4.2.2 Automatic methods using equivalent width fitting

The codes ARES ([Sousa et al. \(2007\)](#)), DAOSPEC ([Stetson and Pancino \(2008\)](#)) and FASMA ([Andreasen et al. \(2017\)](#)) allow to measure the equivalent widths of the lines, fitting them with Gaussian (ARES, FASMA) or Lorentzian (DAOSPEC for strong lines) profiles. Once the observed equivalent width is identified, the radiative transfer code (ex. MOOG, [Snedden \(1973\)](#)) and atmosphere models (ex. ATLAS, [Castelli and Kurucz \(2003\)](#)) are used in order to estimate the abundances. Similarly, the GALA code ([Mucciarelli et al., 2013](#)) is based on the WIDTH9 algorithm ([Kurucz, 2005](#)), and it works both with MARCS and ATLAS models.

4.3 Pre-calculated grid – the GAUGUIN method

Methods based on pre-calculated grids of synthetic spectra are known to work faster, as the radiative transfer calculations are performed in a phase previous to the application. The grids are based on a set of parameters, usually T_{eff} , $\log(g)$, v_{micro} , $[\text{Fe}/\text{H}]$ and $[\alpha/\text{Fe}]$. They allow to analyse a big amount of spectra in a short time. Examples of these methods are MyGIsFOS ([Sbordone et al., 2014](#)), FERRE ([Allende Prieto et al., 2006](#)), the RAVE pipeline using XCSAO within IRAF ([Boeche et al., 2011](#)), and, finally, the GAUGUIN code, realised in C++ programming language ([Bijaoui \(2012\)](#), [Guiglion et al. \(2016\)](#), [Guiglion \(2015\)](#)). GAUGUIN is a classical, local optimization method that implements a Gauss-Newton algorithm, and it is based on a local linearisation around a given set of parameters that are associated with a reference synthetic spectrum (via linear interpolation of the derivatives).

The pre-calculated grid of GAUGUIN is based on a five dimensional parameter space spanning: T_{eff} , $\log(g)$, $[\text{M}/\text{H}]$, $[\alpha/\text{Fe}]$ and A_X , where A_X is the chemical abundance of the X element. For the input set of observed stellar parameters T_{eff}^* , $\log(g)^*$, $[\text{M}/\text{H}]^*$, $[\alpha/\text{Fe}]^*$ for each star, a theoretical spectrum is interpolated. Then a one-dimensional grid with variation in A_X values is calculated. If the X element is an α -element, the algorithm can work without the creation of an additional 1D-grid on A_X , but using the $[\alpha/\text{Fe}]$ variation. A few iterations of the Gauss-Newton algorithm are needed until the algorithm converges towards the minimum distance between the observed and the synthetic spectra (Fig. 4.1). In practice, GAUGUIN can be used with the stellar parameters independently determined, as it was done with the MATISSE algorithm ([Recio-Blanco et al., 2006](#)) to derive stellar parameters for the AMBRE project.

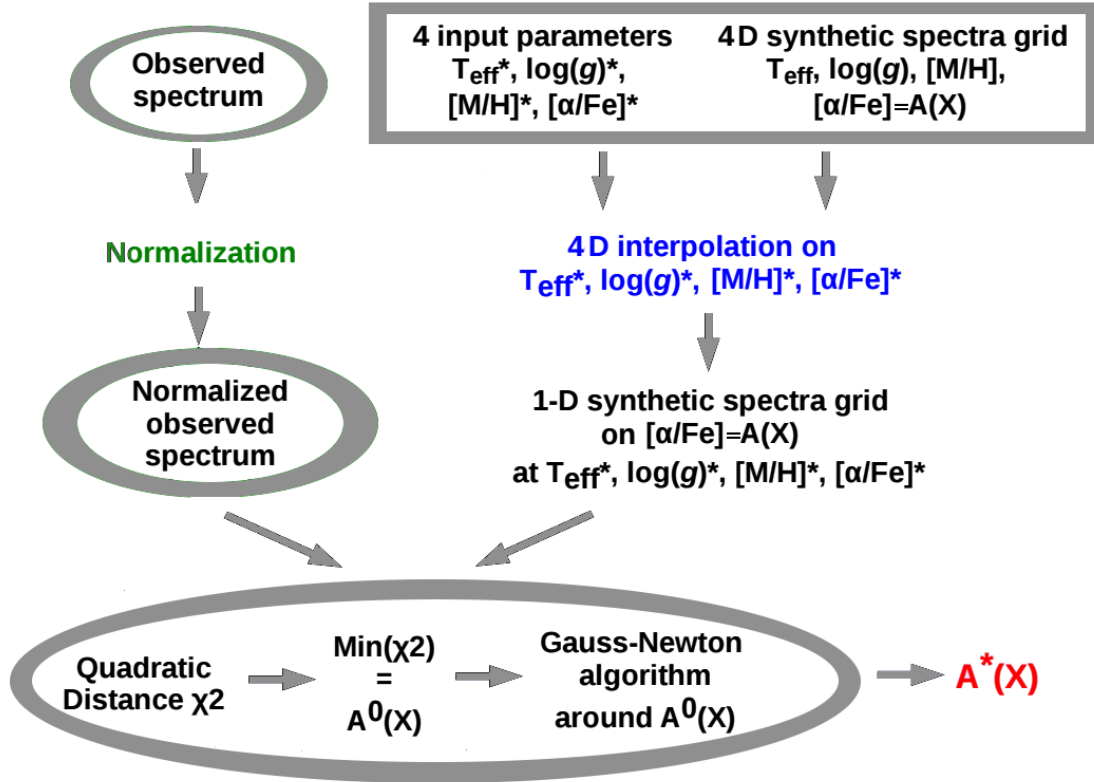


Figure 4.1: The representation of the major steps in GAUGUIN procedure for the stellar α -element abundances determination (Guiglion (2015), adapted). In case if A_X is not an α -element, the initial synthetic grid contains 5 parameters.

The main steps of the GAUGUIN tool are the following (Fig. 4.1):

- 1) Interpolation of a synthetic spectrum, based on derived atmospheric parameters;
- 2) Polynomial normalization of the observed spectrum, using the continuum of the associated theoretical spectrum. An optional local normalization, based on a narrow wavelength region around the selected spectral line is also possible;
- 3) Definition of a set of synthetic profiles from the minimal to the maximum values of the abundance with a given step (for example, -0.4 dex to 0.8 dex with a step of 0.12 dex).
- 4) The individual abundance is estimated through a Gauss-Newton algorithm.

GAUGUIN method was recoded in the *java*-language, in order to integrate it into the interface of the Gaia-DPAC pipeline and for the automatic determination of stellar abundances from RVS-spectra (see Chapter 2). The GAUGUIN method then optimized and tested in the framework of the GSPspec working group of the Gaia DPAC/CU8. The main modifications concerned the interpolation on a non-regular synthetic spectral grid as that of de Laverny et al. (2012). The *java*-version of the GAUGUIN method is very efficient in terms of computational time. As an example, the time needed for the abundance estimation from one spectral line in ~ 4500 spectra (area of $\pm 15 \text{ \AA}$ in a wavelength around the core of the line)

approaches 3 minutes (the configuration of used "cosmos" server: DELL PowerEdge 730, 2 CPU de 20 core each (40 cores): Xeon E5-2698 v4 @ 2.20 GHz, 256 Gio de RAM, CentOS 7.4).

The full description and realisation of the GAUGUIN method, realised in C++ programming language, can be found in [Guiglion \(2015\)](#), while this chapter is dedicated to the issues of the java-version of GAUGUIN, that will be discussed below.

4.4 Interpolation on the parameter grid

Each possible combination of the parameters on the pre-calculated stellar grid is represented as a 4D-vector with coordinates $r_{\text{grid}} = (T_{\text{eff}}, \log(g), [M/H], [\alpha/Fe])$ with an additional 1D-vector of abundances (A_X) if needed ($A_{X_{j+1}} < A_{X_j}$). In this space, a given star is represented as a 4D-vector $r_{\text{observed}} = (T_{\text{eff}}^*, \log(g)^*, [M/H]^*, [\alpha/Fe]^*)$ (see Sect. 4.3). In order to successively interpolate the set of N observed parameters on the space of synthetic parameters, the 2^N neighbour points of the synthetic grid are required (See Fig. 4.2). In the case of GAUGUIN, problems with the interpolation procedure were detected because of two reasons. First, a lack of neighbour points (e.g. effects on grid borders), and second, an irregular character of the synthetic grid, e.g. the non-homogeneous distribution of the grid points.

As shown on the right panel of Fig. 4.4, the $[\alpha/Fe]$ grid has an irregular distribution in the region of metallicities $[Fe/H]$ from -1 dex to 0 dex. It addition, it does not cover the parameter space $[\alpha/Fe] \leq 0$ and $[\alpha/Fe] \geq 0.8$ for the metal-poor content and $[\alpha/Fe] \leq -0.4$ and $[\alpha/Fe] \geq 0.4$ for metal-rich stars.

The first application of the java GAUGUIN tool to the analysis of HARPS spectra from the AMBRE project, produced an anomalous estimation of the the Mg abundance. The left panel of Figure 4.6 shows the distribution of estimated Mg abundance for one spectral line as a function of the AMBRE metallicity for the non-adapted version on the GAUGUIN method.

Basically, the problem lies in the way how the "neighbour" points (see Fig. 4.2) are defined for a given vector of the parameters $r_{\text{observed}} = (T_{\text{eff observed}}, \log(g)_{\text{observed}}, [M/H]_{\text{observed}}, [\alpha/Fe]_{\text{observed}})$ in case of an irregular grid. In order to solve this issue, two procedures were implemented for the $[Mg/Fe]$ one dimensional grid.

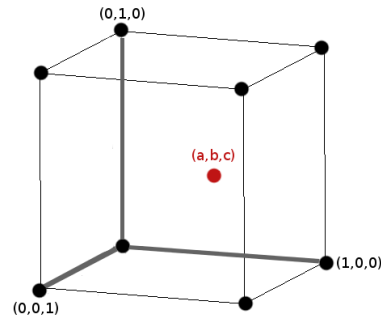


Figure 4.2: The example of the 3D-vector $p=(a, b, c)$ (red circle), where their coordinates can take a positive values up to 1 dex. In this case $2^N = 8$ grid points (black circles) are required to define the vector p .

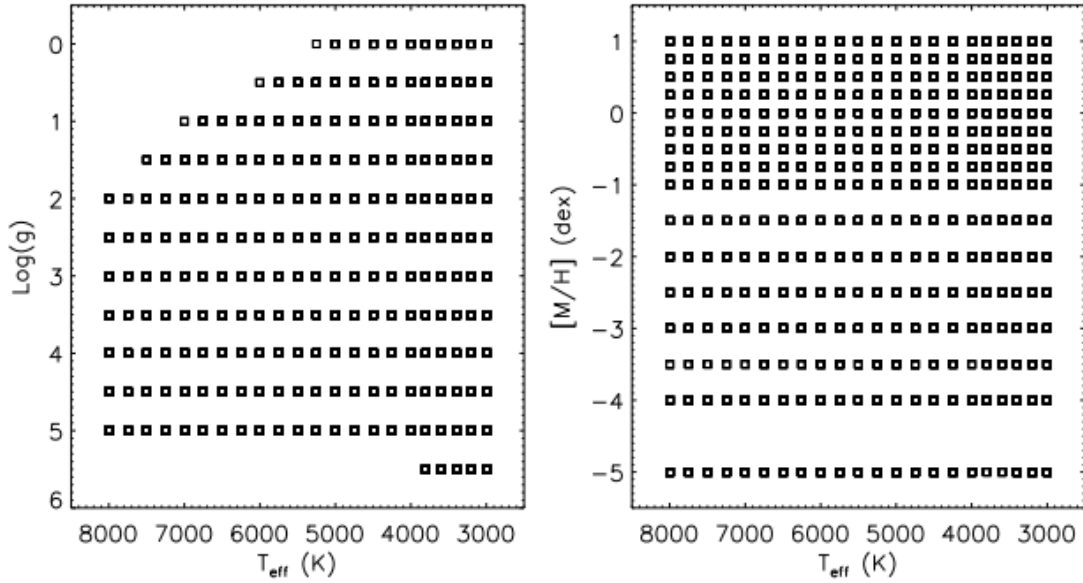


Figure 4.3: Example of atmosphere parameters for the grid GES (see also de Laverny et al. (2012)), used by the GAUGUIN method. On the left: $\text{log}(g)$ with T_{eff} dependence, on the right: $[M/H]$ with T_{eff} dependence. Source of the grid: great.ast.cam.ac.uk/GESwiki/GESHome .

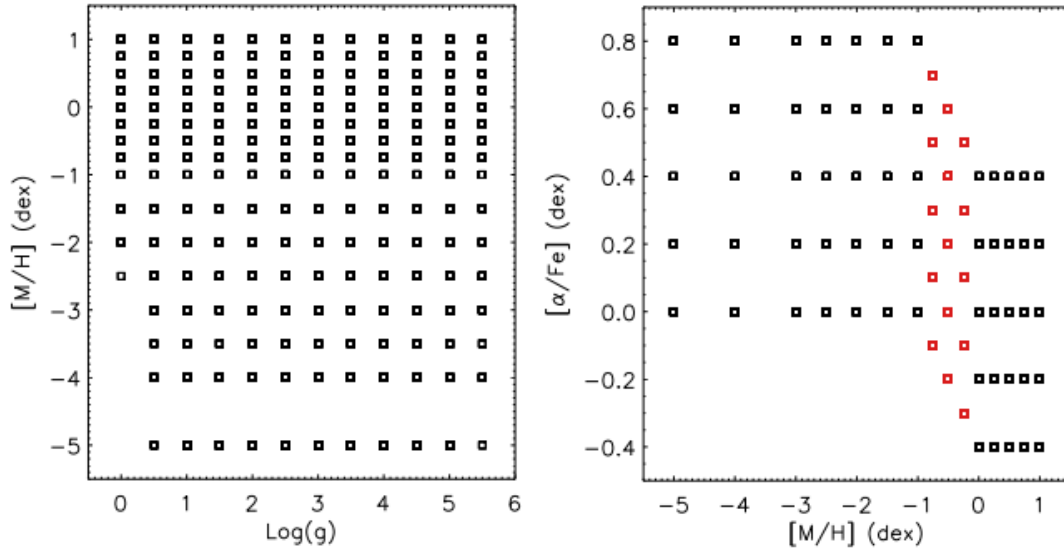


Figure 4.4: Example of atmosphere parameters for the grid GES (see also de Laverny et al. (2012)), used by the GAUGUIN method. On the left: $[M/H]$ with $\text{log}(g)$ dependence, on the right: $[\alpha/Fe]$ with $[M/H]$ dependence. Red points show the area where the distribution of the grid point for $[\alpha/Fe]$ with metallicity $[Fe/H]$ has an irregular character. Source: great.ast.cam.ac.uk/GESwiki/GESHome .

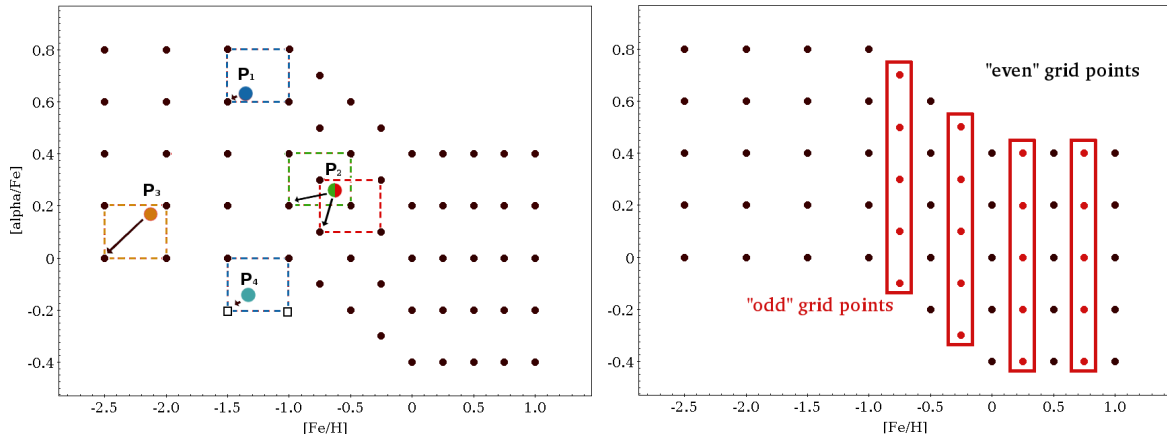


Figure 4.5: The example of the specific grid points of GES-grid (black circles), $[\alpha/\text{Fe}]$ with $[\text{Fe}/\text{H}]$ dependence. On the left: the choice of the "zero"-point during the interpolation. Coloured circles represent different observed values P_i . Dashed lines limit the space of the interpolation, black arrows indicate the "zero"-point for selected set of observed parameters. On the right: separation of the grid point into two categories, based on their values of $[\alpha/\text{Fe}]$ and $[\text{Fe}/\text{H}]$. The "odd" points (red circles) were ignored while interpolating the observed parameters, when the "even" points (black circles) were used.

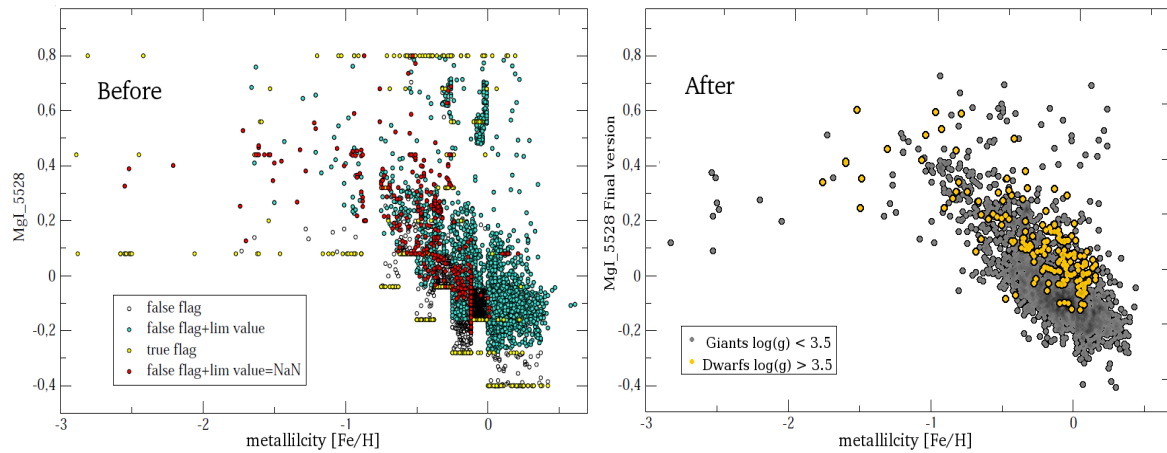


Figure 4.6: Example of the $[\alpha/\text{Fe}]$ vs. metallicity distribution, obtained by the GAUGUIN method. On the left: algorithm version, non-adapted to the issues on irregular synthetic parameter grid. Different colors represent flagged points: open circles are accepted values, yellow are rejected border grid values, turquoise are rejected values with overestimated abundance, red represents rejected values with no estimation of abundance limit. On the right: final version of the algorithm with implemented corrections (See Sect. 4.4). Grey circles show giant stellar population ($\log(g) < 3.5$), yellow circles show dwarf stellar population ($\log(g) > 3.5$).

The left panel of Figure 4.5 shows a reconstruction of the neighbour points starting with the choice of the "zero"-point. For the a value of $P_i = ([\alpha/\text{Fe}]_{\text{observed}}, [\text{M}/\text{H}]_{\text{observed}})$ the distance d between P_i and all possible points of the grid is calculated. The set N neighbour points ($N = 4$ on 2D-grid, $N = 8$ on 3D-grid) with a smallest values of d is chosen for the interpolation (dashed lines in Fig. 4.5). The contour, defined by these four neighbour points, always contains the P_i inside. The neighbour point with a minimal value of $[\alpha/\text{Fe}]_{\text{zero}}$ $[\text{M}/\text{H}]_{\text{zero}}$ is defined as a "zero"-point.

In some cases the observed point can be associated with two different sets of neighbourhood points, caused of the irregular character of the grid (P_2 on the left panel of Figure 4.5). In this case, a correct definition of the abundance set of A_X is not possible due to a violation of the condition $A_{X_{j+1}} < A_{X_j}$. Therefore, the method estimates chemical abundances, solving the Gauss-Newton algorithm on randomly chosen set of neighbour points. To avoid this random solutions, the $[\alpha/\text{Fe}]$ distribution of the grid was regularized by eliminating some of the grid points. In particular, as it shown on the right panel of Figure 4.5, the points of the grid were flagged as "odd" and "even". The points, identified as "odd", were ignored by the algorithm when treating the grid. In this way, the "even" points built-up a homogeneously distributed grid.

Final version includes these two corrections, that has allowed to solve the estimation problems. The right panel of Figure 4.6 shows the distribution of estimated Mg abundance for one spectral line as a function of the AMBRE metallicity for the optimized java version of the GAUGUIN method.

4.5 Normalization of the spectra

The global normalization of the observed spectrum is directly connected with an interpolated theoretical spectrum, that has the same atmospheric parameters as the given observed one. This theoretical spectrum is the result of the interpolation on the pre-calculated spectral grid to the derived atmospheric parameters (Sect. 4.3). Both the theoretical spectrum and the observation contain the same number of points with a regular step $\Delta\lambda$ in the same range of wavelength from λ_{init} to λ_{fin} , that requires the correction of the observed spectrum for the radial velocity shift v_{rad} .

The normalization of the observed spectrum passes by following steps.

- 1) An identification of the continuum points in the associated theoretical spectrum. These points constitute the mask of wavelengths.
- 2) A translation of the defined continuum points in the synthetic spectrum to the observed one, based on the created mask of wavelengths.
- 3) A reconstruction of the continuum with a polynomial interpolation on the final set of the continuum points.

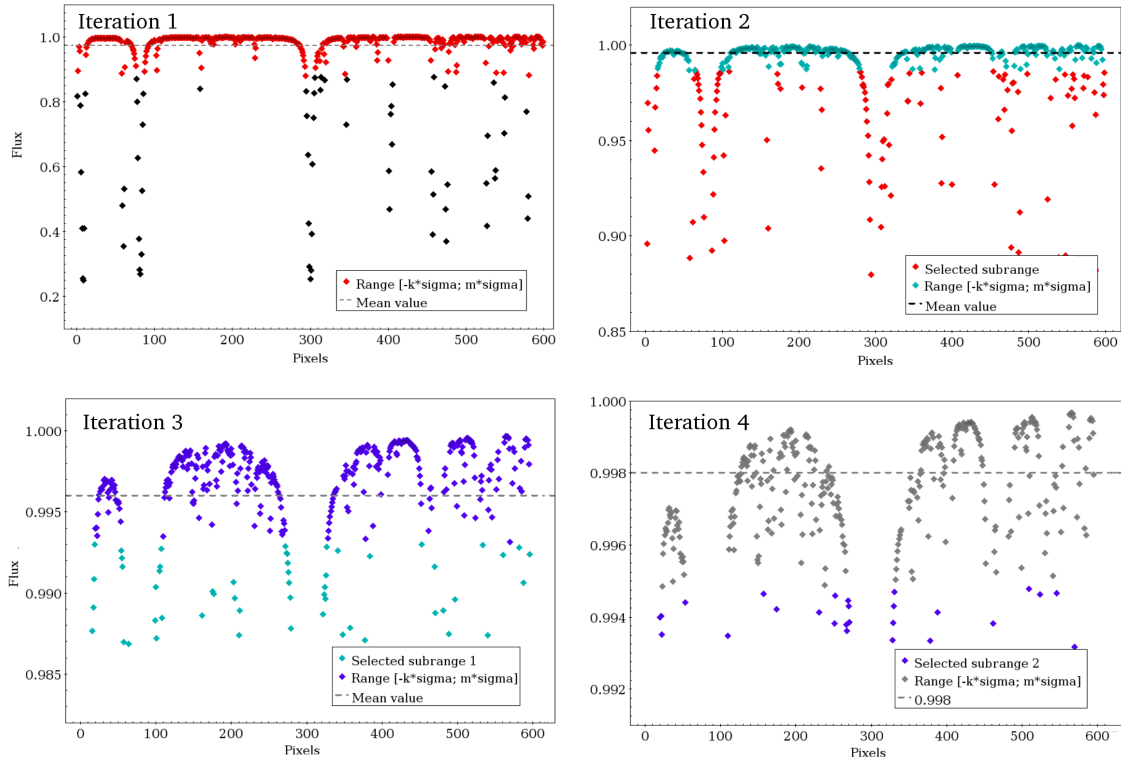


Figure 4.7: An example of the iteration, running in interpolation-normalisation mode with synthetic spectrum.

1. Searching of the continuum points in the Synthetic spectrum.

(1st cycle) The first cycle of the normalisation procedure consists on the estimation of the Mean value (M_1) and the Standard deviation (σ_1) for the flux in the selected wavelengths. The first approach for the set of continuum points is selected inside the range $[M_1 - k \cdot \sigma_1; M_1 + m \cdot \sigma_1]$, where normally the selected values are $k = -0.5$ and $m = 5$. The procedure passes through 10 iterations. That means, that at the iteration $i = 1$ all points from the synthetic spectrum constitute the input, at the iteration $i = 2$ the input consist of the points, selected at the first iteration. The third iteration is build up from the points, selected at the second iteration, etc. Thus, each time, the i -iteration is based on the set of points, selected at the $(i - 1)$ -iteration. Figure 4.7 shows the color-coded example for 4 iteration processes. The correspondence of the colors indicate the sample of the selected and ignored points of the continuum at each iteration.

(2d cycle) At the second cycle, the set of selected points in the last iteration of cycle 1, is used to build up the intermediate spectrum. Using this reconstructed spectrum as the input, the same procedure as described in the cycle 1 passes. The estimation of the Mean value (M_2) and the Standard deviation (σ_2) is performed with a new criteria of the continuum selection from $[M_2 - n \cdot \sigma_2; M_2 + l \cdot \sigma_2]$. The parameters are selected as $n = -5$ and $l = 3$. The whole cycle contains 10 iterations (the same as Fig. 4.7 with a different σ -clipping criteria).

(3d cycle) The third step is similar to the previous one. The Mean value (M_3) and the Standard deviation (σ_3) are calculated, and the continuum points are selected to be inside the range $[M_3 - r \cdot \sigma_3; M_3 + s \cdot \sigma_3]$, where $r = -1$ and $s = 2$. The whole cycle contains 10 iterations (the same as Fig. 4.7 with a different σ -clipping criteria).

(4th cycle) Again a new σ -clipping cycle is implemented, the Mean value (M_4) and the Standard deviation (σ_4) are calculated and the points for the next iteration are chosen inside $[-2\sigma_4; 2\sigma_4]$ range. The whole cycle contains 10 iterations.

2. Associating the selected continuum points to the Observed spectrum.

The last iteration of cycle 4 gives the set of continuum points that are associated with the points from the observed spectrum according to the initial wavelength in both spectra. Based on this "mask", the Mean value (M_{obs}) and the Standard deviation (σ) are calculated. Then, similarly to the procedure described for the synthetic spectrum, the points inside $[M_{obs} - \sigma_{obs}; M_{obs} + 5\sigma_{obs}]$ are chosen. This procedure goes through a single iteration. The selected points constitute the almost final version of the continuum selection $S_{preliminar}$.

3. Reconstruction of the continuum.

Finally, the sample of obtained continuum points is cleaned by introducing the additional parameter $\mu = \frac{\sigma_M}{M} \times R_{max}$, where M is the mean flux, calculated for all the selected points, σ_M is the associated standard deviation and R_{max} is the maximal value of the residuals (the difference between the fluxes at selected point value and the M). The final set of the continuum points S_{final} is defined by the expression: $S_{preliminar} - S_{final} > -0.2\mu$, where $S_{preliminar}$ is the set of continuum points.

Based on the defined final set of the continuum points S_{final} , the continuum is reconstructed for the whole wavelength range. A polynomial fit with a selected degree finish the normalization.

4.6 Visualisation

A visualisation option of the spectra with a saving possibility of the selected plots was included into the list of GAUGUINs capacities. For each spectral line, the output of two figures is available. First, a comparison of the observed spectral line with a set of calculated abundances and the final solution (Fig. 4.8). Second, a plot with the observed non-normalised spectrum, the synthetic one and the final observed normalised spectrum. Figure 4.9 shows the examples of the normalisation for a dwarf (left column) and giant (the right one) star, for the wavelength region that covers the area from 5150 to 5730 Å. Finally, the obtained normalised spectra can be automatically saved in the individual files using the FITS-format.

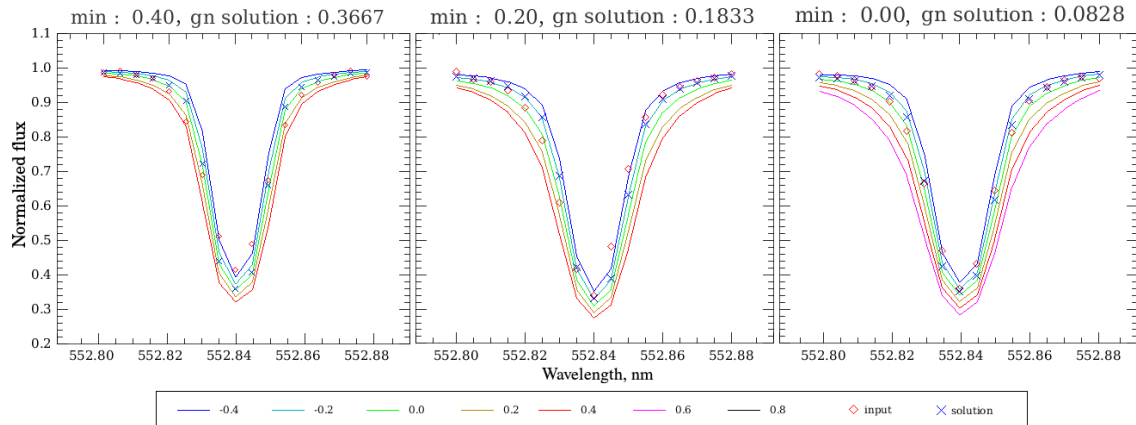


Figure 4.8: Example of the visualisation tool of GAUGUIN for MgI ($\lambda_{\text{core}} = 5528.4 \text{ \AA}$) spectral line for three different spectra. Different lines represent calculated synthetic grid, rhombus symbols are the points of the observed spectrum, cross-symbols are the GAUGUIN solution. The closest value from calculated grid given as "min", the final abundance is "gn solution" value.

4.7 Summary

This chapter has presented the method developed to perform the automatic estimation of individual chemical abundances. The optimization and testing of the method was performed with the measurement of the individual abundances of magnesium from six spectral lines in optical range. The method was applied to 13500 high-resolution synthetic spectra and 4355 high resolution observed HARPS spectra. The final version of the method was integrated to the interface of the Gaia satellite, in order to perform automatic determination of the individual abundances of chemical elements for the RVS spectra. The module is applied to real satellite data since September 2017 for validation cycles 2&3 within Gaia DPAC.

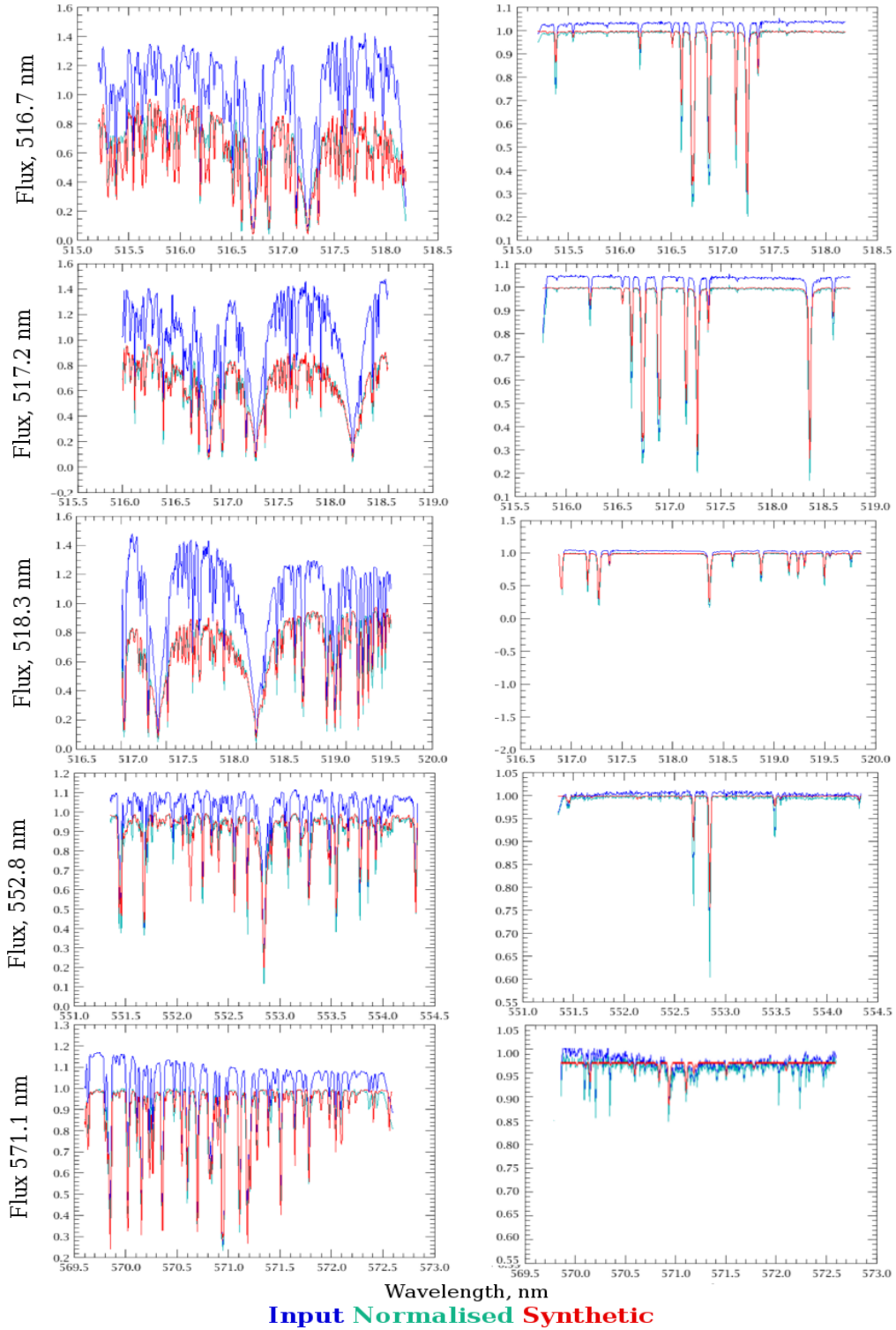


Figure 4.9: On the left: the spectrum of HD 59984 ($T_{\text{eff}} = 5960 \pm 100$, $\log(g) = 3.9 \pm 0.26$, $[\text{Fe}/\text{H}] = -0.85 \pm 0.08$, $[\alpha/\text{Fe}] = 0.13 \pm 0.04$). On the right: the spectrum of HD 74000 ($T_{\text{eff}} = 6200 \pm 100$, $\log(g) = 3.95 \pm 0.26$, $[\text{Fe}/\text{H}] = -2.1 \pm 0.08$, $[\alpha/\text{Fe}] = 0.38 \pm 0.04$)

Abundances of Mg and Y

Contents

5.1 Observations and synthetic grid	57
5.2 Spectroscopic sample: selection of Mg and Y lines	58
5.3 Methodology of the chemical abundance estimation	59
5.4 Abundance error estimation	60
5.5 Summarizing Mg and Y stellar abundances	62

This chapter is dedicated to the chemical analysis of high resolution stellar spectra. Having the method of automatic determination of the individual chemical abundances (GAUGUIN, Chapter 4) on one hand and the refined catalogue of stellar parameters high resolution spectra (AMBRE, Chapter 3) on the other, the estimation of magnesium and yttrium abundances was performed in the optical diapason. In particular, the dataset with the highest spectral resolution, AMBRE HARPS, was analysed.

5.1 Observations and synthetic grid

The selected observed sample contains 4355 HARPS parametrized spectra of FGK stars in the range of wavelength 5167–6319 Å, that contains selected magnesium lines, and 4124–5729 Å with selected yttrium lines. Each spectrum was corrected for the radial velocity shift. The spectra were normalized following the procedures described in Sect. 4.5. Finally, the spectra are cut in the chunks of $\pm 15\text{Å}$ around the selected spectral lines.

Regarding the magnesium abundance estimations, the reference theoretical spectra grid used by GAUGUIN was the GES synthetic grid of non-rotating FGKM-type spectra, provided for the GES consortium. It is a high resolution optical synthetic spectra grid in the 4200–6900 Å wavelength range calculated from the MARCS stellar atmosphere models (Gustafsson et al., 2008), GES/LineList_V5 atomic and molecular line-lists, provided by the GES/LineList Group. The microturbulence v_{micro} was implemented in the synthetic spectra, following the relation proposed by Hill & Bergemann in 2012: for main sequence and subgiants ($\log(g) \geq 3.5$) with two possible temperature regimes ($T \geq 5250$ and $T < 5250$), and giants ($\log(g) < 3.0$). For atmospheric models with high $\log(g) \in [3.5; 5.5]$ v_{micro} was set at

1.0 km s⁻¹ and for low $\log(g)$ (≤ 3.0) v_{micro} was set at 2.0 km s⁻¹, which are typical values for dwarfs and giants respectively. The [Mg/Fe] variations used for the abundance estimation correspond to the $[\alpha/\text{Fe}]$ variation of the grid, i.e. ± 0.4 dex around the nominal value with a step of 0.2 dex.

Regarding the Y abundance estimations, a specific grid of synthetic spectra has also been computed around the YII lines. A similar procedure to the adopted one for the AMBRE grid (de Laverny et al., 2012) was followed, but considering also an enhancement in yttrium varying over a range of ± 1.2 dex around the metallicity with a step of +0.2 dex (leading to 13 different values of [Y/Fe] for each metallicity value). The yttrium line data from Hannaford et al. (1982) and McWilliam et al. (2013) were adopted (see Table 5.1). More details on the computation of the grid can be found in Guiglion (2015) and Guiglion et al. (2018).

To be in agreement with the prepared observational HARPS spectra, the resolution of the theoretical spectra was reduced to $\sim 110\,000$.

5.2 Spectroscopic sample: selection of Mg and Y lines

Our selection of Mg spectral lines is based on the work of Mikolaitis et al. (2017). We finally retained the five strong lines presented in Table 5.1, for which the Mg abundance results were less dispersed. In addition, the selection of Y spectral lines has been done to avoid possible blends (Van der Swaelmen, private communication).

The abundances of Y and Mg from each spectrum were calculated as the median value of all available lines (see Table 5.1), and the result was flagged with the final number of lines, used for each spectrum. As a first quality cut, we adopted the results for the spectra with $S/N > 30$ (see Fig. 5.1) and standard deviation smaller than 0.4 dex. The final stellar abundance was then defined as the median abundance value from the different spectra of the star.

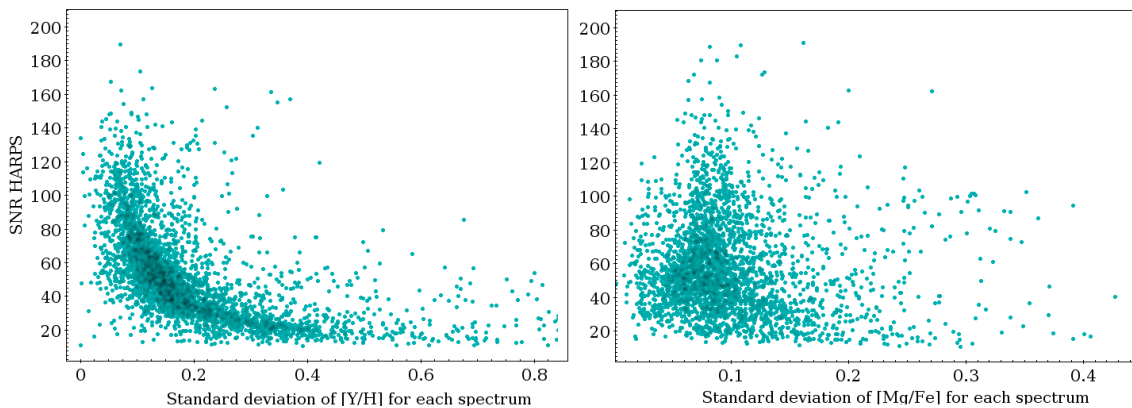


Figure 5.1: Distribution of the signal-to-noise ratio as a function of the lines standard deviation σ for [Y/H] (on the left panel) and [Mg/Fe] (on the right panel) for each spectrum.

MgI line (Å)	Line range (Å)	
5167.3	5166.9	5167.7
5172.6	5172.2	5173.15
5183.6	5183.2	5184.0
5528.4	5528.0	5528.8
5711.0	5710.7	5711.4
YII line (Å)	Line range (Å)	
4124.19	4123.81	4125.01
4398.01	4397.86	4398.16
4883.68	4883.48	4883.88
4900.12	4899.97	4900.27
4982.13	4981.98	4982.28
5087.42	5087.27	5087.57
5200.41	5200.26	5200.56
5728.89	5728.69	5729.09

Table 5.1: The list of the wavelengths of adopted MgI and YII lines. Left column represents the core wavelengths for each line, and the used for the abundance estimation wavelength ranges are included in other two columns.

5.3 Methodology of the chemical abundance estimation

The abundances of magnesium and yttrium were homogeneously derived for the complete HARPS-TGAS catalogue. For this purpose, the GAUGUIN method (Bijaoui (2012), Guiglion et al. (2016)) was used (Chapter 4). It is a classical local optimization method implementing a Gauss-Newton algorithm, based on a local linearisation around a given set of parameters that are associated with a reference synthetic spectrum (via linear interpolation of the derivatives). A few iterations are carried out through linearisation around the new solutions, until the algorithm converges towards the minimum distance between the observed spectrum and the synthetic spectrum library. In practice, we used GAUGUIN together with the stellar parameters independently determined by the algorithm MATISSE (Recio-Blanco et al. (2006), De Pascale et al. (2014)) for the AMBRE project. The GAUGUIN code includes a local normalization step around the selected spectral lines. It is worth noting that GAUGUIN is part of the GSPspec module of the APSIS pipeline (Bailer-Jones et al., 2013) implemented within the Gaia Data Processing and Analysis Consortium. In particular, GSPspec is in charge of deriving parameters and abundances from Gaia RVS spectra (Recio-Blanco et al., 2016).

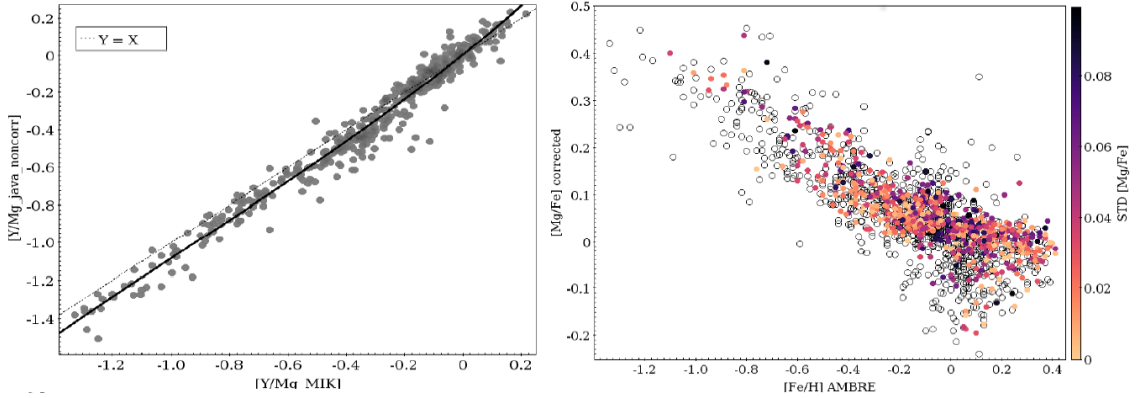


Figure 5.2: On the left: The relation of $[Y_{\text{cor}}/\text{Mg}_{\text{non-cor}}]$ vs $[Y_{\text{cor}}/\text{Mg}_{\text{Mikolaitis}}]$ for 260 turn-off stars. "Corrected" here means that abundances of Y and Mg were corrected for solar values. Polynomial fit of 3d degree was applied. The solid line represents the calibration, that was applied to calculated abundances, the dashed one is diagonal. On the right: The abundances of $[\text{Mg}/\text{Fe}]$ for sample of 660 stars with $\sigma < 0.1$ are color-coded with the σ value, the rest of the sample (~ 1140 stars) are presented with open circles.

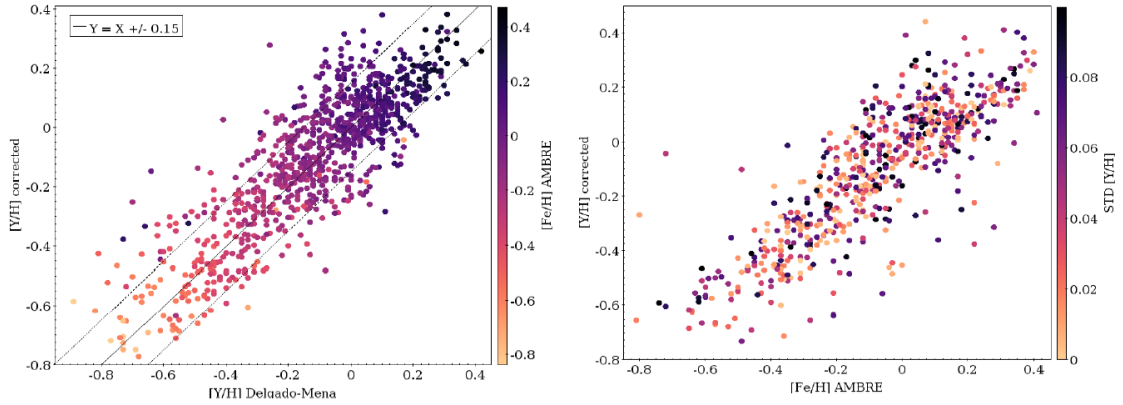


Figure 5.3: On the left: the relation of the corrected abundances for $[\text{Y}/\text{H}]$ and the literature ones (Delgado Mena et al., 2017) for the same sample of objects, 920 stars in common. On the right: calibrated $[\text{Y}/\text{H}]$ abundances for 630 stars with standard deviation $\sigma_{[\text{Y}/\text{H}]} < 0.1$, color-coded with $\sigma_{[\text{Y}/\text{H}]}$ value, calculated as the standard deviation of the $[\text{Y}/\text{H}]$ abundance from 8 lines.

5.4 Abundance error estimation

We have performed the abundance error analysis following three different indicators. First, the internal error, given by the line-to-line dispersion per spectra, has been considered. The corresponding histograms for the Mg and Y abundances are shown in Fig. 5.4. The peak of the distribution is at 0.07 dex for the Mg abundance and 0.12 dex for the Y one.

Second, thanks to the important number of repeats in the catalog (40% of the stars have

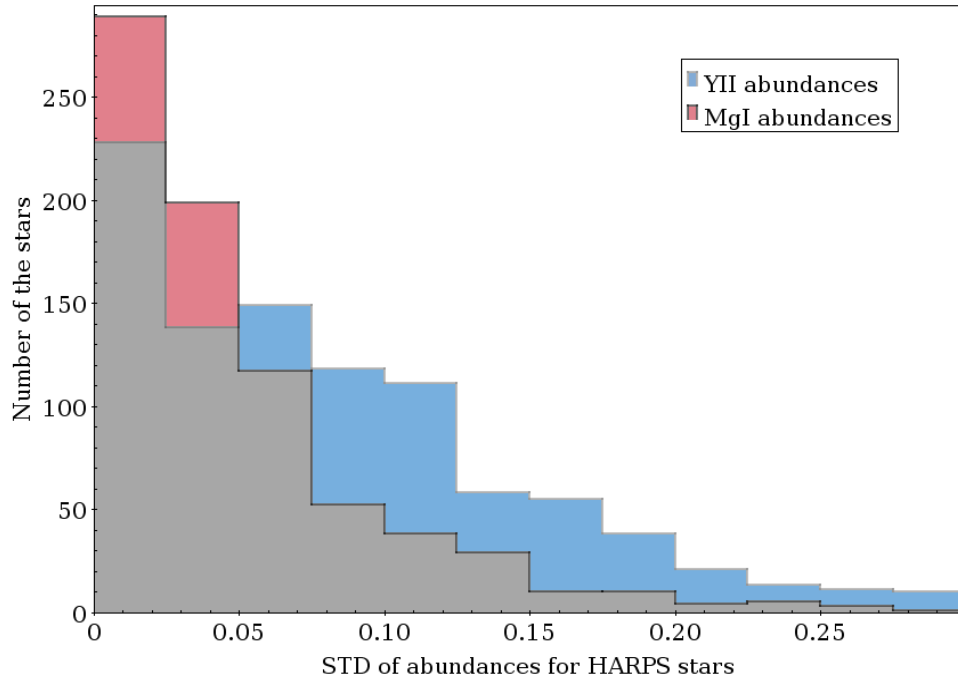


Figure 5.4: Distribution of standard deviation of $[Y/H]$ and $[Mg/Fe]$ abundances for HARPS stars repeated observations. The red color represents MgI distribution, blue represents YII, grey represents the common area for both.

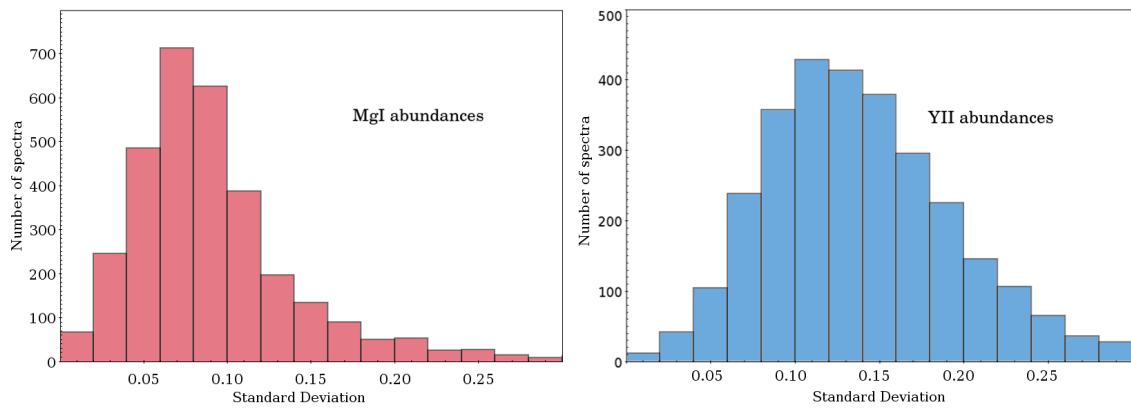


Figure 5.5: The distribution of standard deviation for the determination of $[Y/H]$ and $[Mg/Fe]$ for HARPS spectra. On the left: distribution of the standard deviation of $[Mg/Fe]$ for each spectrum, calculated as median value by 5 spectral lines from Table 5.1. On the right: the same for $[Y/H]$ abundances, calculated by 8 spectral lines.

one spectrum, and 95% of the stars have being observed less then 30 times, see [De Pascale et al. \(2014\)](#)), we have been able to evaluate the influence of the parameter uncertainties in the abundance estimation by looking at the spectrum-to-spectrum dispersion. We recall that the AMBRE project provides atmospheric parameters for each individual spectrum of

a particular star. The variations in the atmospheric parameters for the repeated spectra with signal-to-noise higher than 30 are lower than 40 K in effective temperature, 0.07 dex in $\log(g)$ and 0.03 dex in $[M/H]$. Figure 5.5 shows the histogram of the Mg and Y abundances dispersion for the repeated spectra. The third quantile of the distribution is at 0.06 dex for Mg and 0.10 dex for Y.

Finally, external errors have been evaluated by comparing our abundance estimations to literature samples having a statistically relevant overlap with our data set. The left panel of the Figure 5.6 shows the histogram of the difference between our Mg abundance estimations and the Mikolaitis et al. (2014) ones. The standard deviation of the difference is 0.08 dex. We notice that Mikolaitis et al. (2014) have used the same AMBRE parameters as this work, but only the highest signal to noise spectra per star has been considered, contrary to our approach. In addition, they used a different abundance estimation method, as well as a different reference spectra grid. The right panel of the Figure 5.6 presents the histogram of the differences between our Y abundance estimations and the Delgado Mena et al. (2017) ones (935 stars in common). In this case, the atmospheric parameters, the abundance estimation method and the reference theoretical spectra used by Delgado Mena et al. (2017) differ from the ones used in this work. The standard deviation of the Y abundance difference is 0.12 dex.

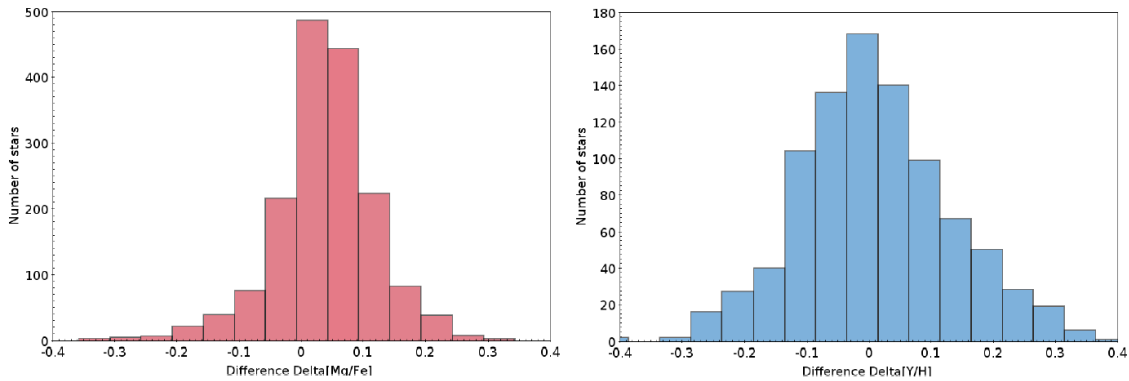


Figure 5.6: On the left: Distribution of the difference between $[Mg/Fe]$ abundances between AMBRE/HARPS and the results from Mikolaitis et al. (2017). On the right: Distribution of the difference between $[Y/H]$ abundances between AMBRE/HARPS and the results from Delgado Mena et al. (2017).

5.5 Summarizing Mg and Y stellar abundances

The sample of 4355 high-resolution HARPS spectra of FGK stars in the wavelength range 4124–6319 Å was analysed. Using the GAUGUIN method (Chapter 3) together with the atmospheric parameters, collected in the AMBRE HARPS project, the individual abundances from 8 spectral lines of YII and 5 spectral lines of MgI were obtained. The selection by the standard deviation value, calculated from the median of all lines and all spectra for each star,

leads to a sample of 2050 stars with estimated yttrium abundances and 1795 stars with estimated magnesium abundances. From this total database a sub-sample of 342 turn-off stars has both YII and MgI abundance estimations. Turn-off stars are here selected by requiring $M_J < 3.75$ and $\log(g)$ from [3.6; 4.4]. The M_J is the absolute magnitude and is determined using the apparent 2MASS magnitude and the distance (Hayden et al., 2018, submitted). This main sequence turn-off sub-sample, for which precise age estimations from isochrone fitting can be derived, will be used in the following chapter to study the time dependence of the yttrium and magnesium abundances for disk stars.

The details of the number of analysed stars is summarized in Table 5.2.

$N_{\text{stars YII}}$	$N_{\text{stars MgI}}$	<i>Description</i>
2050	1795	All calculated abundances;
-	1670	In common with Mikolaitis et al. (2017);
935	-	In common with Delgado Mena et al. (2017).
342		Final sample of TO-stars with available stellar age value.

Table 5.2: The details of the number of analysed stars, the single spectrum cases and the overlap with reference catalogues for the Y and Mg abundances.

[Y/Mg] correlation with Age

Contents

6.1	Age estimations	65
6.2	Exploring the age dependence of the Y, Mg and Fe abundance	66
6.3	Exploring the age dependence of the [Y/Mg]	68
6.4	The chemical clock: inverting the [Y/Mg]-Age relation	70
6.5	Differences between the thin and the thick disk	71
6.6	Summary	72

In this chapter the time dependence of the [Y/Mg] abundance as a function of metallicity, age and disk component membership (thin or thick disk) will be analysed. The stars have been tagged as belonging to the thin disk, the thick disk or the high-alpha metal-rich population, following the chemical classification of Mikolaitis et al. (2017), which is based on its [Mg/Fe] chemical index.

Magnesium is one of the so-called α -elements. As was mentioned before, these elements are the result of the life of massive stars, ejecting them into the interstellar medium through the supernova type II explosion process. These processes are quite short with respect to the lifetime of the Galaxy, because massive stars have short life times (Crowther, 2012).

Yttrium is an element of slow neutron capture), that is produced during asymptotic giant branch phase of intermediate mass and low-mass stars. The time-scale for this elements is longer than for α -elements (Battistini and Bensby, 2016). The ratio of these two elements [Y/Mg] can therefore inform us about the chemical evolution of a particular stellar population. In addition, it can provide an estimation of the stellar age by providing a clock of the chemical evolution.

6.1 Age estimations

First of all, the distances and the stellar ages were determined, using the HARPS-TGAS catalogue, described in Chapter 3. A Bayesian analysis was used to this purpose as described in Hayden et al., 2018 (submitted). The derived stellar parameters from AMBRE were compared to theoretical isochrones from the Dartmouth group (Dotter et al., 2008), following a

method similar to the one described by [Jørgensen and Lindegren \(2005\)](#). A complete description of the methods to determine ages is included in the *AMBRE-Gaia* DR1 catalog ([Hayden et al., 2018, submitted](#)). The derived and observed stellar parameters (effective temperature T_{eff} , metallicity $[\text{Fe}/\text{H}]$, abundance $[\text{Mg}/\text{Fe}]$, absolute magnitude in K-band M_K) were compared to those provided by the Dartmouth isochrones. The isochrones are spaced in age from 0 to 15 Gyr, with the step of 100 Myr, in $[\text{Fe}/\text{H}]$ from -2.0 to $+0.6$ with the step of 0.1 dex, and from 0.0 to $+0.4$ dex in $[\text{Mg}/\text{Fe}]$ with the step of 0.2 dex. In order to select a sample of the stars that have a unique estimation of age, the turn-off stars were identified. Following the selection, that requires $M_J < 3.75$ and $\log(g)$ from $[3.6; 4.4]$, where M_J is the absolute magnitude, determined with use of the apparent 2MASS magnitude and the distance ([Hayden et al., 2018, submitted](#)), the sample of 502 turn-off stars was identified (Fig. 6.1).

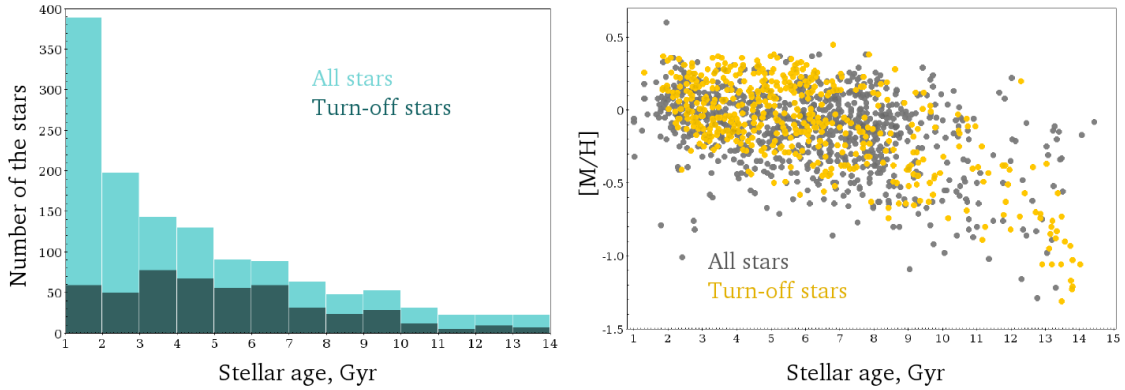


Figure 6.1: The characteristics of the catalog of stellar ages ([Hayden et al., 2018, submitted](#)) for the *AMBRE* HARPS data. The left panel represent the histogram of the stars by their ages, the right panel shows a trend of the metallicity with the stellar age. The sample of 502 turn-off stars is color-coded in dark blue (left panel) and yellow circles (right panel).

6.2 Exploring the age dependence of the Y, Mg and Fe abundance

Figure 6.2 presents the abundances of $[\text{Fe}/\text{H}]$, $[\text{Y}/\text{H}]$ and $[\text{Mg}/\text{Fe}]$ as a function of the stellar age for turn-off stars with errors lower than 0.1 dex in abundances. A linear fit for each abundance ratio is presented and given by the following equations:

$$[\text{Fe}/\text{H}] = 0.250 - 0.055 \times \text{Age} \text{ with a } \sigma_{[\text{Fe}/\text{H}]} = 0.231 \text{ (Eq. 1),}$$

$$[\text{Y}/\text{H}] = 0.150 - 0.050 \times \text{Age} \text{ with a } \sigma_{[\text{Y}/\text{H}]} = 0.212 \text{ (Eq. 2),}$$

$$[\text{Mg}/\text{Fe}] = -0.04 + 0.017 \times \text{Age} \text{ with a } \sigma_{[\text{Fe}/\text{H}]} = 0.054 \text{ (Eq. 3).}$$

Although the $[\text{Fe}/\text{H}]$ (upper panel) and the $[\text{Y}/\text{H}]$ abundances (middle panel) clearly present negative slopes, both of them present an important dispersion with stellar age (0.23 dex

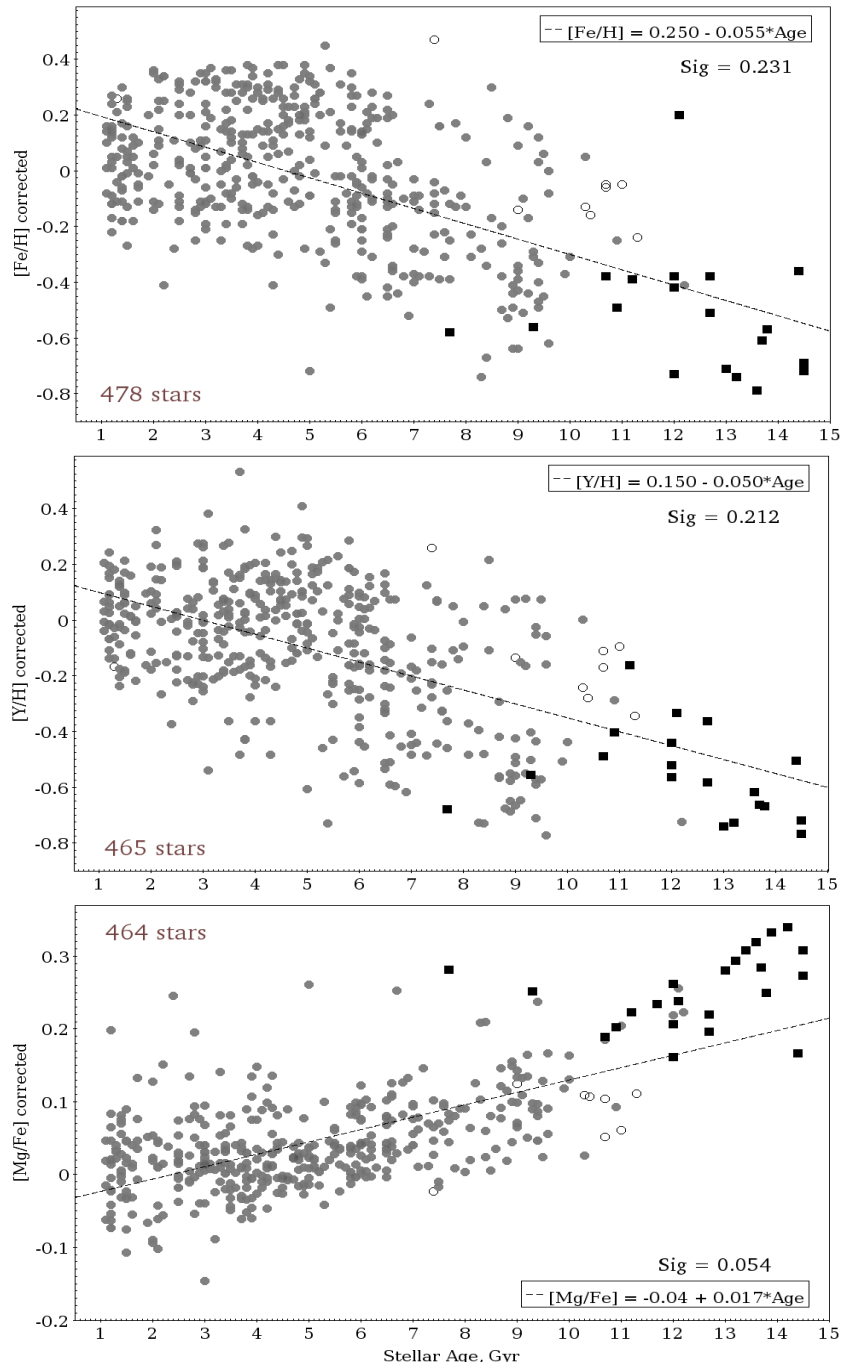


Figure 6.2: Trends of the [Fe/H], [Y/H] and [Mg/Fe] abundances with age for the complete turn-off sample of AMBRE HARPS data. Number of stars, coefficients of the fit and total dispersion of the fit are given on each panel. Thin disk stars are plotted as filled circles, while thick disk stars are represented as filled squares. Opened circles are high-alpha metal-rich objects, following the chemical classification of Mikolaitis et al. (2017).

and 0.21 dex respectively); the [Mg/Fe] abundance ratio (lower panel) presents a better correlation, with a dispersion of 0.054 dex, that makes the [Mg/Fe] ratio a rather good proxy of the age (Nissen (2015), Tucci Maia et al. (2016)). However, two different regimes seem to exist – for stars younger and older than ~ 10 Gyrs (top panel of Figure 6.3). As shown in previous studies (Haywood et al. (2013), Hayden et al. (2017)), the trend of the [Mg/Fe] ratio with stellar age seems to be steeper for thick disk stars (black squares) than for thin disk stars (grey circles). Thus the [Mg/Fe] abundance can not be chosen as a robust age indicator for the thin disk population.

6.3 Exploring the age dependence of the [Y/Mg]

Figure 6.3 shows the [Y/Mg] abundance ratio as a function of stellar age for three different sub-samples of turn-off stars, color-coded with stellar metallicity. The abundance error constraints are increasing progressively. The upper panel presents the stars with the errors under the level of 0.10 dex for [Mg/Fe] and 0.20 dex for [Y/H], the middle panel presents the stars with the errors under the level of 0.05 dex for [Mg/Fe] and 0.10 dex for [Y/H], and the bottom panel presents the thin disk stars with the errors under the level of 0.05 dex for [Mg/Fe] and 0.05 dex for [Y/H]. The linear fit of each panel corresponds to the presented thin disk population with ages younger than 10 Gyrs. The correlation slightly decreases to -0.29 dex due to smaller dispersion around the thin disk points. Although the dispersion of the results is still considerable, a trend with age is already clear. With respect to thin disk population (circles) the thick disk stars (squares), older than 10 – 11 Gyrs, seem to be shifted to the thin disk population, although presenting an anti-correlation (-0.82 dex) with stellar age. The thin disk vs. thick disk differences will be studied more in detail in the next section.

It should be noted, that many of the young and intermediate age thin disk stars are metal-rich objects with very crowded spectra. Therefore, a final selection of a limited sample of stars hotter than 5700 K and having [M/H] less than 0.0 dex has been performed. This selection avoids problems of blending and continuum placement that could affect the spectral analysis. In addition, only stars with errors lower than 0.05 dex both in the [Mg/Fe] abundance and the [Y/H] one were chosen. This high precision sample is shown in the lower panel of Figure 6.3. Clearly, a clean anti-correlation appears down to 9 Gyrs. The final fit of this correlation is:

$$[Y/Mg]_{\text{thin disk}} = (0.036 \pm 0.005) - (0.029 \pm 0.0015) \times \text{Age}. \quad (\text{Eq. 4})$$

This fit approaches the one of Nissen (2015) and Tucci Maia et al. (2016) for solar twins within a slightly lower value of the slope. Reducing the parameter space covered by the data set helps to reduce the internal error spread, including internal biases from one type of star to the other.

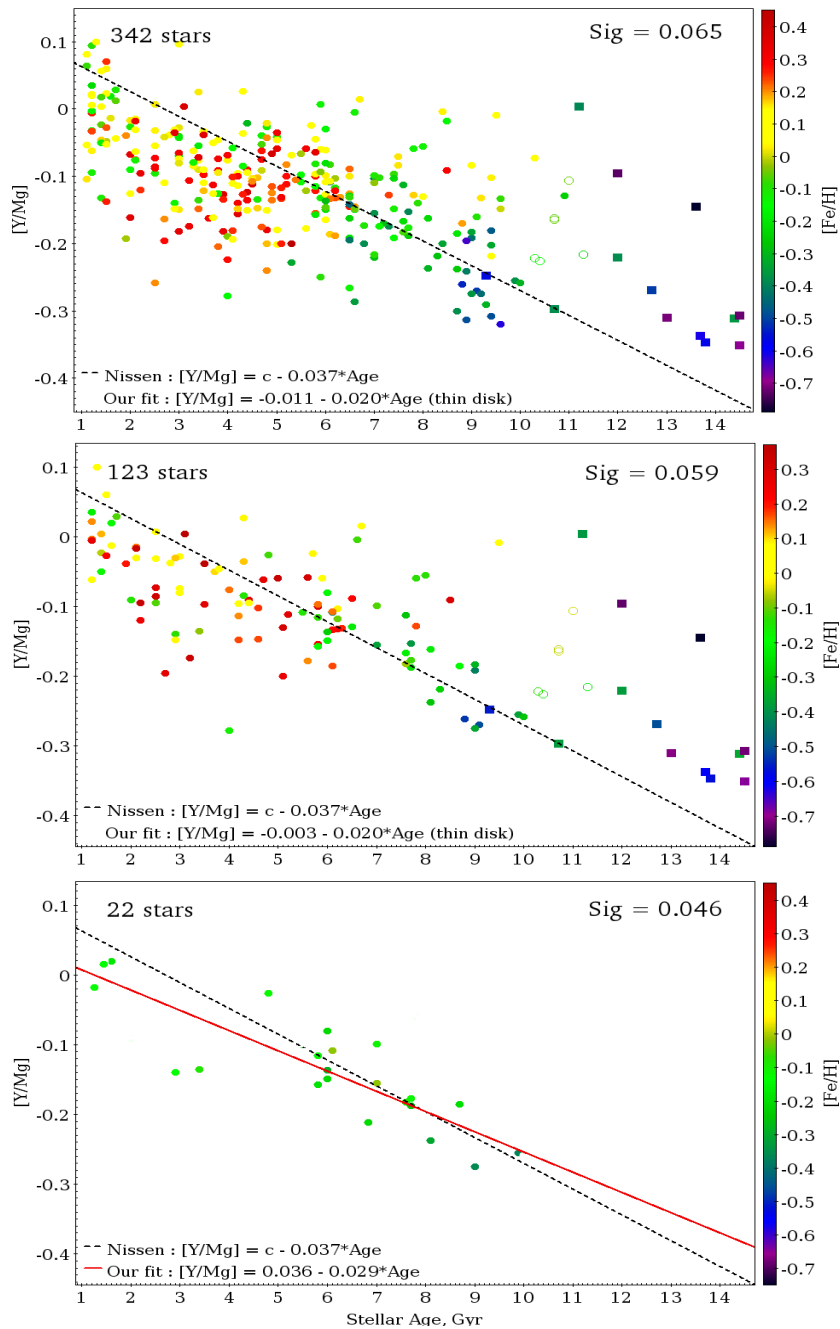


Figure 6.3: $[Y/Mg]$ versus stellar age dependence. Top panel: 342 stars with $\sigma_{YII} < 0.2$ dex and $\sigma_{MgI} < 0.1$ dex; middle panel: 123 turn-off stars with $\sigma_{YII} < 0.1$ dex and $\sigma_{MgI} < 0.05$ dex; bottom panel: 22 turn-off thin disk stars with $\sigma_{YII} < 0.05$ dex and $\sigma_{MgI} < 0.05$. The symbols are those of Fig. 6.2, but including a colour code for the stellar metallicity. The dotted line shows the [Nissen \(2015\)](#) fit for solar type stars (here $c = 0.1$ dex), the red solid line (on the bottom) is the fit for the high precision sample of thin disk stars.

6.4 The chemical clock: inverting the [Y/Mg]-Age relation

The clean [Y/Mg]-Age relation derived in Sect. 6.3 can be used to estimate stellar ages for thin disk stars, replacing isochrone fitting outside the ranges of applicability (for instance, main sequence stars outside the turn-off, etc...). The precision in the derived age can be estimated by propagating the errors in Equation 4. As an example, for a star with the value $[Y/Mg] = (-0.1 \pm 0.05)$ dex the estimation of error in age is around 2 Gyr.

To test this chemical clock, Equation 4 was inverted for the sample of 45 AMBRE HARPS main sequence and sub-giant branch stars slightly outside the conditions of turn-off definition, given in the section 6.1, considered. Isochrone fitting ages were derived for those stars, that were not used in the analysis of Sect. 6.3, following the procedure of Hayden et al. (2018, submitted). In parallel [Y/Mg] based ages were derived. Figure 6.4 shows the comparison of both sets of ages. A good correlation appears, with a standard deviation of the difference equal to 2.4 Gyrs. The zero point of the difference seems to be within the error for stars younger than 10 Gyrs, like those of the thin disk used to derive the relation. In conclusion, the [Y/Mg] abundance ratio can well be used as an age proxy for the thin disk stars with a reasonable precision, and they can replace more precise age estimations when the last are not available.

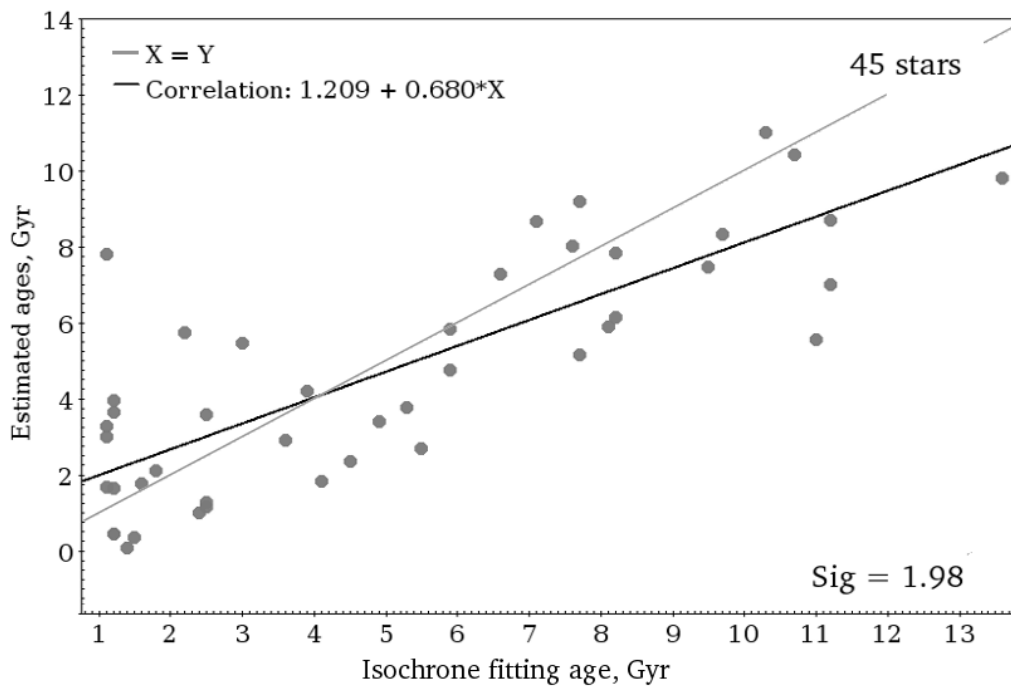


Figure 6.4: Comparison of stellar ages derived from the [Y/Mg] ratio with isochrone fitting ages, for a sample of stars not used to infer the [Y/Mg]-Age relation.

6.5 Differences between the thin and the thick disk

The dependence of $[Y/Mg]$ with stellar age is based on the chemical evolution of the analysed population, so different galactic components could present different trends with age, depending, among other things, on their star formation history. The previous sections were focussed on the analysis of thin disk stars, that represent the majority of the AMBRE HARPS turn-off data.

However, in Sect. 6.3 it was pointed out that the shift, that thick disk stars seem to present with respect to the thin disk, is causing a discontinuity in the $[Y/Mg]$ correlation with age. Figure 6.5 shows the high precision thin disk data set together with the thick disk set, but relaxing the errors to 0.1 dex in $[Mg/Fe]$ and 0.20 dex in $[Y/H]$, that allows to include more metal-poor stars in the sample. A trend of the $[Y/Mg]$ abundance ratio with age seems to exist for the thick and thin disks both (Delgado Mena et al., 2018). The trend seems to be steeper for the thick disk than for the thin one. A similar difference between thick and thin disk appears in the evolution of the $[Mg/Fe]$ ratio with time in the studies of Haywood et al. (2013) and Hayden et al. (2017), highlighting differences in the chemical evolution of these two populations, with the thick disk probably presenting a higher star formation rate. The final derived trends for the thin and the thick disk populations are summarized in Table 6.1.

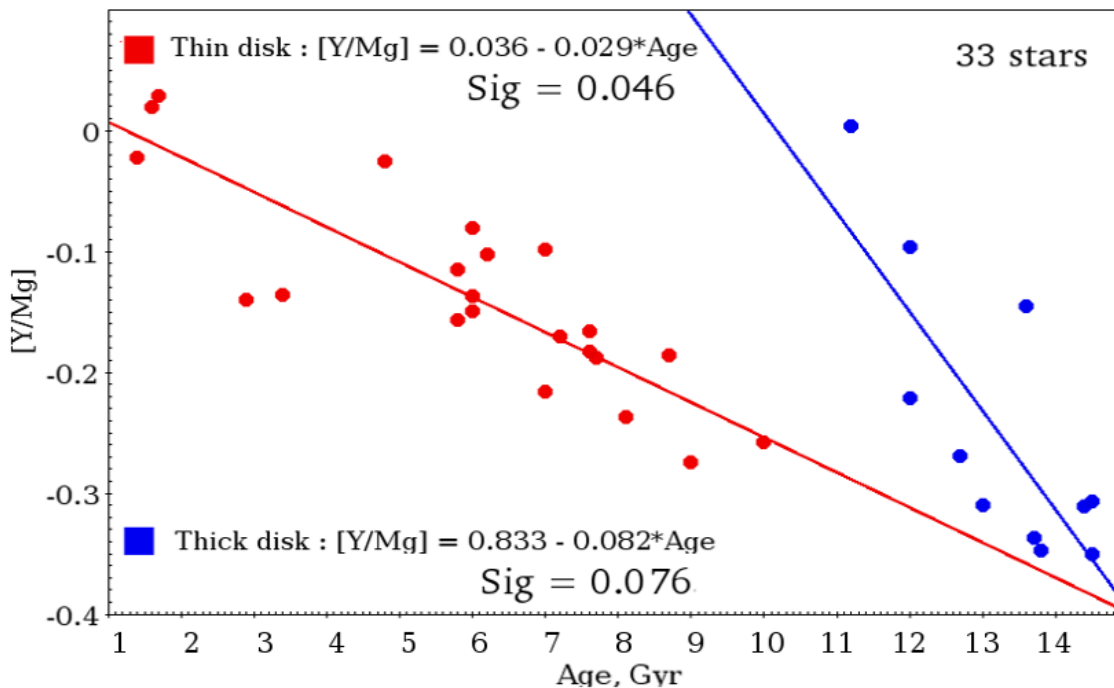


Figure 6.5: $[Y/Mg]$ versus age fit for thin and thick disk stars.

6.6 Summary

The presented analysis confirms the sensitivity of the [Y/Mg] abundance ratio to stellar age. Thanks to a sample with a high precision of chemical abundances and isochrone ages, the correlation of the [Y/Mg] abundance with stellar age has been evaluated for thin disk and thick disk stars in the solar neighbourhood.

First, it should be mentioned the importance of reducing the relative errors in the abundances, by selecting i) stellar types that are reliable to analyse (less crowded spectra, easier continuum estimation,...) and ii) reduced parameter space of the studied samples to minimize internal biases.

Second, a clear correlation between [Y/Mg] and age has been found, with a trend similar to those found in previous studies for solar type stars (Nissen (2015), Tucci Maia et al. (2016)). For the thin disk stars, no particular trend with metallicity seems to exist. The obtained ratio was tested for stellar age dating through the use of the [Y/Mg] chemical diagnostic, and a precision of around 2 Gyrs, in comparison with existing data, was achieved.

Finally, for the first time, a difference between the thin disk and the thick disk population in the [Y/Mg] dependence with age was detected. As expected from the different chemical evolution history for these two populations, different trends of the [Y/Mg] abundance with age seem to exist. A threshold around 10 Gyrs appears in the sample, revealing a chemical discontinuity between the thick and the thin disk. The population of thick disk stars seems to have a steeper trend with age. To clarify this, more investigations on the thick disk population are needed.

fit	A	B × Age	σ_{fit}
[Y/Mg] _{thin}	0.036 ± 0.005	-0.029 ± 0.0015	0.046
[Y/Mg] _{thick}	0.833 ± 0.005	-0.082 ± 0.0015	0.076

Table 6.1: Resulting coefficients of the fitting [Y/Mg] with stellar age for thin and thick disk components.

General conclusions

7.1 Summary

Many questions, intimately linked to our understanding of the formation and evolution of disk galaxies, remain still open (Rix and Bovy, 2013). In fact, the observational constraints at our disposal have been insufficient until now. In particular, before the advent of the Gaia mission, three-dimensional distributions and 3D stellar velocities were only available for relatively small samples, mostly in the solar neighbourhood. In addition, stellar ages were, in practice, impossible to derive for most of the survey targets, due to imprecise distance estimations. As a consequence, the temporal dimension, so crucial to the understanding of the Milky Way history and for comparison with model predictions, was not available.

Fortunately, Gaia data has opened the path to stellar age estimations for large samples of stars, mainly thanks to isochrone fitting methods. In addition, Gaia precise distances allow to develop indirect age estimations based on the chemical evolution clock. This thesis has been focussed on the use of a particular chemical clock, the [Y/Mg] abundance. To this purpose, the following results have been achieved:

- 1. The object identification of the AMBRE high resolution spectroscopic data base has been implemented.** The AMBRE catalogue, based on the ESO archive data from the HARPS, UVES and FEROS instruments, contains the parametrisation of 200160 spectra, and 112027 spectra of them (about 56%) have estimations of the effective temperature T_{eff} . The first part of this thesis has been dedicated to the improvement of the existing catalogue thanks to a homogeneous object identification, capable to overcome the complexity of a data base build up from archive data. In particular, the analysis of the stellar coordinates, reported in the ESO archive, was held. A coordinate cross-match with the 2MASS catalogue has resulted in the identification of 6776 individual stars, corresponding to 10976 spectra from the AMBRE catalogue (parametrised at least with the effective temperature). In other words, the 98% of the parametrised spectra, that exist in the AMBRE catalogue, have associated coordinates from the 2MASS catalogue. Additionally, the stars in common between the different individual AMBRE catalogues were analysed. It leads to 456 stars between FEROS and HARPS, 240 stars between HARPS and UVES and 262 stars between FEROS and UVES. Moreover, 97 objects are in common for all the three instruments. The AMBRE catalogue has also an important overlap with the Tycho-Gaia astrometric solution (TGAS), the full-sky five parameters astrometric solution, provided in the first Gaia data release. The cross-match

between the final AMBRE sample and TGAS covers 1919 stars from the HARPS dataset, 1567 stars from FEROS, and 750 stars from UVES. A complete description of the procedure and obtained results are presented in Chapter 3.

2. The adaptation and optimization of the GAUGUIN method, developed to the automatic estimation of individual chemical abundances for the Gaia GSP-Spec module, was performed. The multi-linear interpolation on an irregular synthetic grid of $[\alpha/\text{Fe}]$ vs. metallicity distribution was studied and optimized. In addition, continuum normalisation issues were fixed, testing a consistent method, based on sigma-clipping with different parameters. Finally, a visualisation option was implemented. The results are summarised in Chapter 4.

The final version of the method was integrated to the Gaia DPAC APSIS pipeline, in order to perform automatic determination of the individual abundances of chemical elements for the RVS spectra. **The module is applied to real satellite data since September 2017 for validation cycles 2&3 within Gaia DPAC.**

3. The Mg and Y abundances from the AMBRE-HARPS spectra have been estimated and calibrated using the GAUGUIN. In particular, individual abundances from 8 spectral lines of YII and 5 spectral lines of MgI were obtained for the sample of 4355 high-resolution HARPS spectra of FGK stars in the wavelength range 4124–6319 Å was analysed. The selection by the standard deviation value, calculated from the median of all lines and all spectra for each star, leads to a sample of 2050 stars with estimated yttrium abundances and 1795 stars with estimated magnesium abundances. From this total database a sub-sample of 342 turn-off stars has both YII and MgI abundance estimations. The results are summarised in Chapter 5.

4. The sensitivity of the $[\text{Y}/\text{Mg}]$ abundance ratio to stellar age was analysed, based on a sample of main sequence turn-off stars with a high precision of chemical abundances and isochrone ages. The correlation of the $[\text{Y}/\text{Mg}]$ abundance, obtained in Chapter 5, with stellar age has been evaluated for thin disk and thick disk stars in the solar neighbourhood (Nissen (2015), Tucci Maia et al. (2016)). The analysis shows the importance of reducing the relative errors in the abundances, by selecting i) stellar types that are reliable to analyse (less crowded spectra, easier continuum estimation,...) and ii) reduced parameter space of the studied samples to minimize internal biases, in order to find a clear correlation between $[\text{Y}/\text{Mg}]$ and age.

5. The obtained trend of the $[\text{Y}/\text{Mg}]$ abundance ratio to stellar age is similar to those found in previous studies for solar type stars. For the thin disk stars, no particular trend with metallicity seems to exist.

6. The obtained ratio was tested for stellar age dating through the use of the [Y/Mg] chemical diagnostic, and a precision of around 2 Gyrs, in comparison with existing data, was estimated.

7. For the first time, a difference between the thin disk and the thick disk population in the [Y/Mg] dependence with age was detected. As expected from the different chemical evolution history for these two populations, different trends of the [Y/Mg] abundance with age seem to exist. A threshold around 10 Gyrs appears in the sample, revealing a chemical discontinuity between the thick and the thin disk. The population of thick disk stars seems to have a steeper trend with age. The analysis, concerning the [Y/Mg] with stellar age relation, is described in details in Chapter 6 and in Titarenko et al. 2018, A&A, submitted.

Tycho and HIPPARCOS

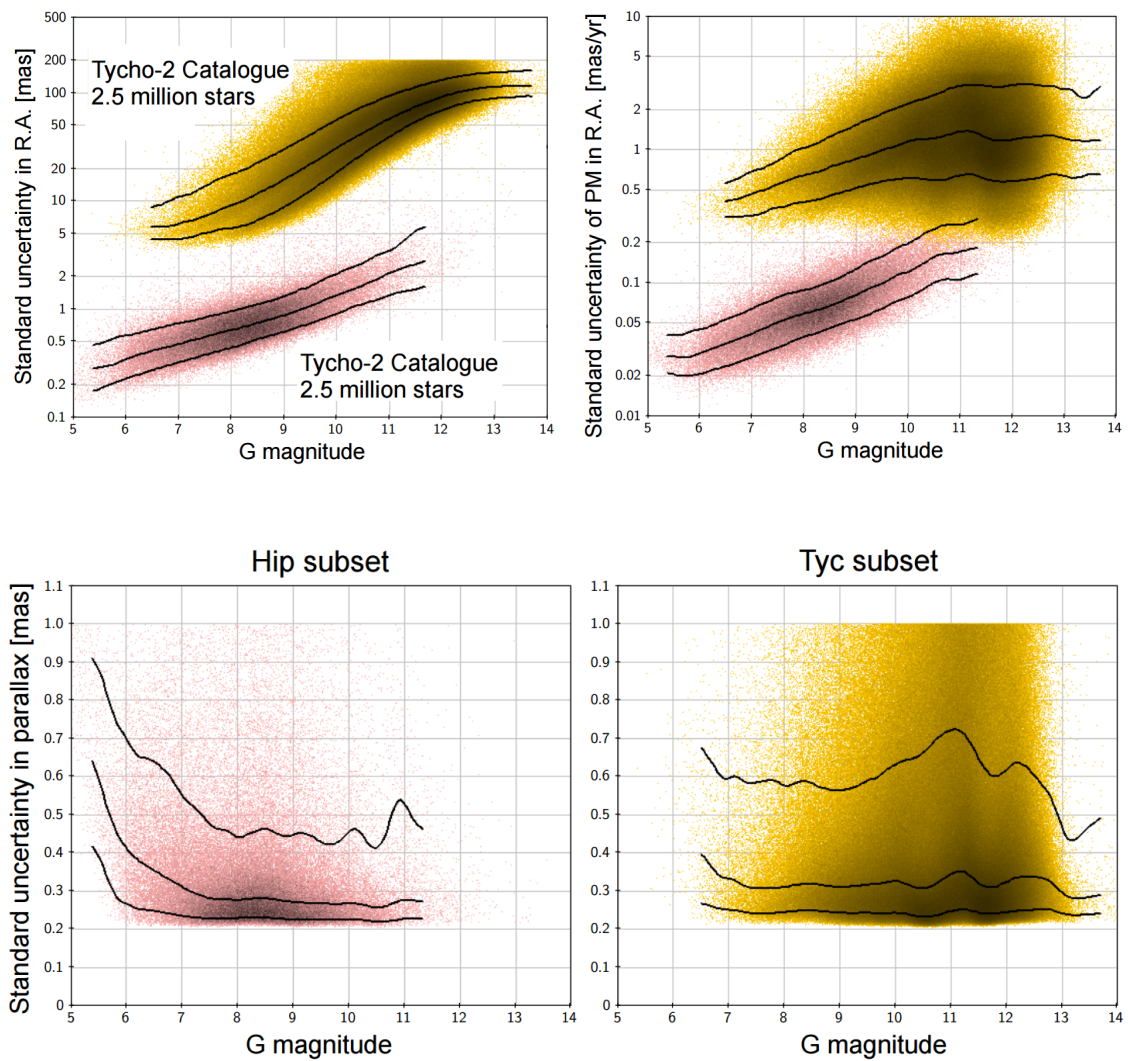


Figure 8.1: On the top: Positional errors at 1991.25 for Hipparcos and Tycho-2. On the bottom: standard uncertainty in proper motion versus magnitude for the Tycho-2 and HIPPARCOS subsets. Credit: Lennart Lindegren, IAUS 330: Astrometry and Astrophysics in the Gaia sky. 24-28 April 2017, Nice, France.

Problems with non-adapted GAUGUIN-java version

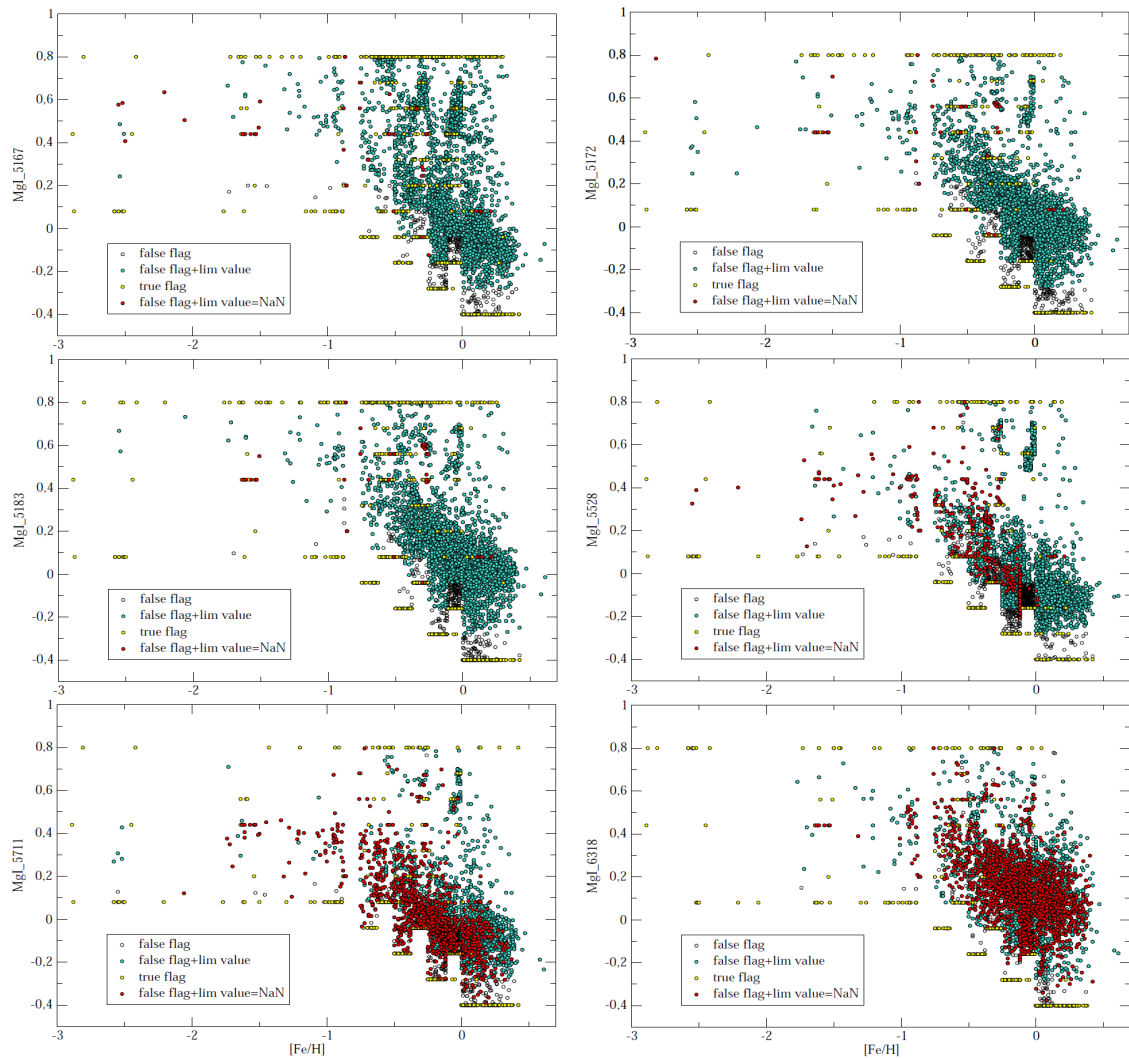


Figure 9.1: $[\text{Mg}/\text{Fe}]$ versus $[\text{Fe}/\text{H}]$ distribution for non-verified GAUGUIN version. Many side effects on the borders of the synthetic grid can be observed (yellow circles). The limit value of chemical abundance is calculated for each entry (open and green circles), otherwise the limit value is flagged as NaN (red circles).

List of Figures

1.1	The ESO 3.6-metre telescope at La Silla, during observations. Credit: ESO / S. Brunier	2
1.2	Schematic representation of components of our Galaxy.	4
1.3	Abundance ratios $[\alpha/\text{Fe}]$ vs. $[\text{Fe}/\text{H}]$. On the left: the blue triangles refer to the thick disk, red circles to the thin disk, magenta squares to the halo, the green asterisks and the black crosses to the transition stars between thin-thick and thick-halo, respectively. The black dashed curve separates the stars with high/low α content. Credit: Adibekyan et al. (2012). On the right: Same as the left panel but colour coded by age (the larger implies older). Credit: Haywood et al. (2015).	5
1.4	The HR diagram for the synthetic sample of 2968 stars (on the left) and the location of two hypothetical observation (on the right), the lines represent the set of isochrones of different ages. The example shows the critical case when the isochrone fitting gives a multiple solution for the same object. On the left: isochrones are for 0, 1, 2, ..., 8, 10, 12 and 15 Gyr. On the right: the symbols along isochrones show where initial mass is a multiple of $0.01 M_{\text{sun}}$. Credit: Jørgensen and Lindegren (2005)	8
1.5	Hertzsprung-Russell diagramm. Within the same sequence, there are smooth transitions of the parameters of the stars (mass, age, diameter, luminosity, temperature and other parameters.). Stars are classified according to the spectrum.	11
1.6	The curve of growth for the chemical elements as a function of its abundance. Three possible regimes – linear 1, saturation and strong lines 2 – are represented on the left panel, and their correspondence in the line profile (weak 1 and strong 2) on the right panel. Credit: (Gray, 2005).	12
2.1	Artist representation of the Gaia spacecraft mapping the stars in the Milky Way galaxy. Credit: ESA/ATG medialab/ESO/S. Brunier	16
2.2	Gaia focal plane. 106 CCDs correspond to 938 million pixels and covers 2800 cm^2 . Credit: ESA, Alexander Short	17
2.3	On the left: transmission for different Gaia instruments (BP with blue line, RP with red line, and RVS with orange line). On the right: the main lines available with Gaia RVS (from A3 supergiants to M2 type stars). Credit: http://gaia.obspm.fr/le-satellite/article/le-spectrographe	18
2.4	Coordinate Units separation in Gaia mission, more information can be found on the web-page http://www.mpia.de/gaia/about/cus	19

2.5	Component modules in Apsis and their interdependency. The module names are defined on the right panel. The arrows indicate a dependency on the output of the preceding module. The coloured bars underneath each module indicate which data it uses. Most of the modules additionally use the photometry and some also the Galactic coordinates. Credit: Bailer-Jones et al. (2013)	19
2.6	The poster of IAUS 330, "Astrometry and Astrophysics in the Gaia sky". Graphic credit: A. Titarenko. Concept: Y. Beletsky & OCA Communication service.	21
2.7	Diagrammatic representation of the outputs of the Gaia and AMBRE databases, showing how they are complementary. Adapted from: Gilmore et al. (2012)	24
3.1	The distribution of the number of unique matches within a search radius area for the HARPS data.	29
3.2	On the left: the histogram of the difference between the coordinates from 2MASS and AMBRE HARPS. The blue dotted line indicates the difference in DEC, the solid black one indicates the difference in RA. On the right: the histogram of the difference between the RA-coordinates from 2MASS and AMBRE HARPS for the result of a 5 arcsec. The histogram is fitted by a normal distribution (solid line) with a value of $\sigma = 0.36$ arcsec.	29
3.3	AMBRE HARPS. On the left: the histogram (20K bin) of the photometric temperature errors, the maximum is around 130 K. On the right: the distribution (100 K bin) of ΔT_{eff} . The dotted lines indicate the 2σ threshold used for the quality label1.	30
3.4	AMBRE HARPS. On the left: the distribution of the differences between the photometric temperatures of giants and dwarfs ($T_{\text{giants}} - T_{\text{dwarfs}}$), width of the bin is 20 K. On the right: the dependence between this difference and the surface gravity $\log(g)$	30
4.1	The representation of the major steps in GAUGUIN procedure for the stellar α -element abundances determination (Guiglion (2015) , adapted). In case if A_X is not an α -element, the initial synthetic grid contains 5 parameters. . .	48
4.2	The example of the 3D-vector $p=(a, b, c)$ (red circle), where their coordinates can take a positive values up to 1 dex. In this case $2^N = 8$ grid points (black circles) are required to define the vector p	49
4.3	Example of atmosphere parameters for the grid GES (see also de Laverny et al. (2012)), used by the GAUGUIN method. On the left: $\log(g)$ with T_{eff} dependence, on the right: $[M/H]$ with T_{eff} dependence. Source of the grid: great.ast.cam.ac.uk/GESwiki/GESHome	50

- 4.4 Example of atmosphere parameters for the grid GES (see also [de Laverny et al. \(2012\)](#)), used by the GAUGUIN method. On the left: $[M/H]$ with $\log(g)$ dependence, on the right: $[\alpha/Fe]$ with $[M/H]$ dependence. Red points show the area where the distribution of the grid point for $[\alpha/Fe]$ with metallicity $[Fe/H]$ has an irregular character. Source: great.ast.cam.ac.uk/GESwiki/GESHome 50
- 4.5 The example of the specific grid points of GES-grid (black circles), $[\alpha/Fe]$ with $[Fe/H]$ dependence. On the left: the choice of the "zero"-point during the interpolation. Coloured circles represent different observed values P_i . Dashed lines limit the space of the interpolation, black arrows indicate the "zero"-point for selected set of observed parameters. On the right: separation of the grid point into two categories, based on their values of $[\alpha/Fe]$ and $[Fe/H]$. The "odd" points (red circles) were ignored while interpolating the observed parameters, when the "even" points (black circles) were used. . . . 51
- 4.6 Example of the $[\alpha/Fe]$ vs. metallicity distribution, obtained by the GAUGUIN method. On the left: algorithm version, non-adapted to the issues on irregular synthetic parameter grid. Different colors represent flagged points: open circles are accepted values, yellow are rejected border grid values, turquoise are rejected values with overestimated abundance, red represents rejected values with no estimation of abundance limit. On the right: final version of the algorithm with implemented corrections (See Sect. 4.4). Grey circles show giant stellar population ($\log(g) < 3.5$), yellow circles show dwarf stellar population ($\log(g) > 3.5$). 51
- 4.7 An example of the iteration, running in interpolation-normalisation mode with synthetic spectrum. 53
- 4.8 Example of the visualisation tool of GAUGUIN for MgI ($\lambda_{\text{core}} = 5528.4 \text{ \AA}$) spectral line for three different spectra. Different lines represent calculated synthetic grid, rhombus symbols are the points of the observed spectrum, cross-symbols are the GAUGUIN solution. The closest value from calculated grid given as "min", the final abundance is "gn solution" value. 55
- 4.9 On the left: the spectrum of HD 59984 ($T_{\text{eff}} = 5960 \pm 100$, $\log(g) = 3.9 \pm 0.26$, $[Fe/H] = -0.85 \pm 0.08$, $[\alpha/Fe] = 0.13 \pm 0.04$). On the right: the spectrum of HD 74000 ($T_{\text{eff}} = 6200 \pm 100$, $\log(g) = 3.95 \pm 0.26$, $[Fe/H] = -2.1 \pm 0.08$, $[\alpha/Fe] = 0.38 \pm 0.04$) 56
- 5.1 Distribution of the signal-to-noise ratio as a function of the lines standard deviation σ for $[Y/H]$ (on the left panel) and $[Mg/Fe]$ (on the right panel) for each spectrum. 58

- 5.2 On the left: The relation of $[Y_{\text{cor}}/Mg_{\text{non-cor}}]$ vs $[Y_{\text{cor}}/Mg_{\text{Mikolaitis}}]$ for 260 turn-off stars. "Corrected" here means that abundances of Y and Mg were corrected for solar values. Polynomial fit of 3d degree was applied. The solid line represents the calibration, that was applied to calculated abundances, the dashed one is diagonal. On the right: The abundances of $[Mg/Fe]$ for sample of 660 stars with $\sigma < 0.1$ are color-coded with the σ value, the rest of the sample (~ 1140 stars) are presented with open circles. 60
- 5.3 On the left: the relation of the corrected abundances for $[Y/H]$ and the literature ones (Delgado Mena et al., 2017) for the same sample of objects, 920 stars in common. On the right: calibrated $[Y/H]$ abundances for 630 stars with standard deviation $\sigma_{[Y/H]} < 0.1$, color-coded with $\sigma_{[Y/H]}$ value, calculated as the standard deviation of the $[Y/H]$ abundance from 8 lines. 60
- 5.4 Distribution of standard deviation of $[Y/H]$ and $[Mg/Fe]$ abundances for HARPS stars repeated observations. The red color represents MgI distribution, blue represents YII, grey represents the common area for both. 61
- 5.5 The distribution of standard deviation for the determination of $[Y/H]$ and $[Mg/Fe]$ for HARPS spectra. On the left: distribution of the standard deviation of $[Mg/Fe]$ for each spectrum, calculated as median value by 5 spectral lines from Table 5.1. On the right: the same for $[Y/H]$ abundances, calculated by 8 spectral lines. 61
- 5.6 On the left: Distribution of the difference between $[Mg/Fe]$ abundances between AMBRE/HARPS and the results from Mikolaitis et al. (2017). On the right: Distribution of the difference between $[Y/H]$ abundances between AMBRE/HARPS and the results from Delgado Mena et al. (2017). 62
- 6.1 The characteristics of the catalog of stellar ages (Hayden et al., 2018, submitted) for the AMBRE HARPS data. The left panel represent the histogram of the stars by their ages, the right panel shows a trend of the metallicity with the stellar age. The sample of 502 turn-off stars is color-coded in dark blue (left panel) and yellow circles (right panel). 66
- 6.2 Trends of the $[Fe/H]$, $[Y/H]$ and $[Mg/Fe]$ abundances with age for the complete turn-off sample of AMBRE HARPS data. Number of stars, coefficients of the fit and total dispersion of the fit are given on each panel. Thin disk stars are plotted as filled circles, while thick disk stars are represented as filled squares. Opened circles are high-alpha metal-rich objects, following the chemical classification of Mikolaitis et al. (2017). 67

-
- 6.3 [Y/Mg] versus stellar age dependence. Top panel: 342 stars with $\sigma_{\text{YII}} < 0.2$ dex and $\sigma_{\text{MgI}} < 0.1$ dex; middle panel: 123 turn-off stars with $\sigma_{\text{YII}} < 0.1$ dex and $\sigma_{\text{MgI}} < 0.05$ dex; bottom panel: 22 turn-off thin disk stars with $\sigma_{\text{YII}} < 0.05$ dex and $\sigma_{\text{MgI}} < 0.05$. The symbols are those of Fig. 6.2, but including a colour code for the stellar metallicity. The dotted line shows the [Nissen \(2015\)](#) fit for solar type stars (here $c = 0.1$ dex), the red solid line (on the bottom) is the fit for the high precision sample of thin disk stars. 69
- 6.4 Comparison of stellar ages derived from the [Y/Mg] ratio with isochrone fitting ages, for a sample of stars not used to infer the [Y/Mg]-Age relation. 70
- 6.5 [Y/Mg] versus age fit for thin and thick disk stars. 71
- 8.1 On the top: Positional errors at 1991.25 for Hipparcos and Tycho-2. On the bottom: standard uncertainty in proper motion versus magnitude for the Tycho-2 and HIPPARCOS subsets. Credit: Lennart Lindegren, IAUS 330: Astrometry and Astrophysics in the Gaia sky. 24-28 April 2017, Nice, France. 77
- 9.1 [Mg/Fe] versus [Fe/H] distribution for non-verified GAUGUIN version. Many side effects on the borders of the synthetic grid can be observed (yellow circles). The limit value of chemical abundance is calculated for each entry (open and green circles), otherwise the limit value is flagged as NaN (red circles). 79

List of Tables

2.1	The list of the wavelengths of adopted MgI and YII lines. Left column represents the core wavelengths for each line, and the used for the abundance estimation wavelength ranges are included in other two columns.	20
5.1	The list of the wavelengths of adopted MgI and YII lines. Left column represents the core wavelengths for each line, and the used for the abundance estimation wavelength ranges are included in other two columns.	59
5.2	The details of the number of analysed stars, the single spectrum cases and the overlap with reference catalogues for the Y and Mg abundances.	63
6.1	Resulting coefficients of the fitting [Y/Mg] with stellar age for thin and thick disk components.	72

Bibliography

- Abadi, M. G., Navarro, J. F., Steinmetz, M., and Eke, V. R. (2003). Simulations of Galaxy Formation in a Λ Cold Dark Matter Universe. I. Dynamical and Photometric Properties of a Simulated Disk Galaxy. *ApJ*, 591:499–514. (Cited in page 6.)
- Adibekyan, V. Z., Figueira, P., Santos, N. C., Hakobyan, A. A., Sousa, S. G., Pace, G., Delgado Mena, E., Robin, A. C., Israelian, G., and González Hernández, J. I. (2013). Kinematics and chemical properties of the Galactic stellar populations. The HARPS FGK dwarfs sample. *A&A*, 554:A44. (Cited in page 5.)
- Adibekyan, V. Z., Sousa, S. G., Santos, N. C., Delgado Mena, E., González Hernández, J. I., Israelian, G., Mayor, M., and Khachatryan, G. (2012). Chemical abundances of 1111 FGK stars from the HARPS GTO planet search program. Galactic stellar populations and planets. *A&A*, 545:A32. (Cited in pages 5, 9 and 81.)
- Allende Prieto, C., Beers, T. C., Wilhelm, R., Newberg, H. J., Rockosi, C. M., Yanny, B., and Lee, Y. S. (2006). A Spectroscopic Study of the Ancient Milky Way: F- and G-Type Stars in the Third Data Release of the Sloan Digital Sky Survey. *ApJ*, 636:804–820. (Cited in page 47.)
- Alonso, A., Arribas, S., and Martínez-Roger, C. (1996a). The empirical scale of temperatures of the low main sequence (F0V-K5V). *A&A*, 313:873–890. (Cited in page 13.)
- Alonso, A., Arribas, S., and Martínez-Roger, C. (1996b). The empirical scale of temperatures of the low main sequence (F0V-K5V). *A&A*, 313:873–890. (Cited in page 27.)
- Anders, F., Chiappini, C., Santiago, B. X., Matijević, G., Queiroz, A. B., and Steinmetz, M. (2018). Dissecting stellar chemical abundance space with t-SNE. *ArXiv e-prints*. (Cited in page 9.)
- Andreasen, D. T., Sousa, S. G., Tsantaki, M., Teixeira, G. D. C., Mortier, A., Santos, N. C., Suárez-Andrés, L., Delgado-Mena, E., and Ferreira, A. C. S. (2017). SWEET-Cat update and FASMA. A new minimization procedure for stellar parameters using high-quality spectra. *A&A*, 600:A69. (Cited in page 47.)
- Baade, W. (1946). A Search For the Nucleus of Our Galaxy. *PASP*, 58:249–252. (Cited in page 3.)
- Bailer-Jones, C. A. L., Andrae, R., Arcay, B., Astraatmadja, T., Bellas-Velidis, I., Berihuete, A., Bijaoui, A., Carrión, C., Dafonte, C., Damerджи, Y., Dapergolas, A., de Laverny, P., Delchambre, L., Drazinos, P., Drimmel, R., Frémat, Y., Fustes, D., García-Torres, M., Guédé, C., Heiter, U., Janotto, A.-M., Karampelas, A., Kim, D.-W., Knude, J., Kolka,

- I., Kontizas, E., Kontizas, M., Korn, A. J., Lanzafame, A. C., Lebreton, Y., Lindstrøm, H., Liu, C., Livanou, E., Lobel, A., Manteiga, M., Martayan, C., Ordenovic, C., Pichon, B., Recio-Blanco, A., Rocca-Volmerange, B., Sarro, L. M., Smith, K., Sordo, R., Soubiran, C., Surdej, J., Thévenin, F., Tsalmantza, P., Vallenari, A., and Zorec, J. (2013). The Gaia astrophysical parameters inference system (Apsis). Pre-launch description. *A&A*, 559:A74. (Cited in pages 19, 20, 59 and 82.)
- Battistini, C. and Bensby, T. (2016). The origin and evolution of r- and s-process elements in the Milky Way stellar disk. *A&A*, 586:A49. (Cited in page 65.)
- Bedding, T. R., Mosser, B., Huber, D., Montalbán, J., Beck, P., Christensen-Dalsgaard, J., Elsworth, Y. P., García, R. A., Miglio, A., Stello, D., White, T. R., De Ridder, J., Hekker, S., Aerts, C., Barban, C., Belkacem, K., Broomhall, A.-M., Brown, T. M., Buzasi, D. L., Carrier, F., Chaplin, W. J., di Mauro, M. P., Dupret, M.-A., Frandsen, S., Gilliland, R. L., Goupil, M.-J., Jenkins, J. M., Kallinger, T., Kawaler, S., Kjeldsen, H., Mathur, S., Noels, A., Silva Aguirre, V., and Ventura, P. (2011). Gravity modes as a way to distinguish between hydrogen- and helium-burning red giant stars. *Nature*, 471:608–611. (Cited in page 6.)
- Bensby, T., Feltzing, S., and Lundström, I. (2003). Elemental abundance trends in the Galactic thin and thick disks as traced by nearby F and G dwarf stars. *A&A*, 410:527–551. (Cited in page 5.)
- Bijaoui, A. (2012). A global strategy for spectral inversion from a model library. In Starck, J.-L. and Surace, C., editors, *Seventh Conference on Astronomical Data Analysis*, page 2. (Cited in pages 45, 47 and 59.)
- Blanco-Cuaresma, S., Soubiran, C., Heiter, U., and Jofré, P. (2014). Determining stellar atmospheric parameters and chemical abundances of FGK stars with iSpec. *A&A*, 569:A111. (Cited in page 46.)
- Bland-Hawthorn, J. and Freeman, K. (2014). Near Field Cosmology: The Origin of the Galaxy and the Local Group. *The Origin of the Galaxy and Local Group, Saas-Fee Advanced Course, Volume 37. ISBN 978-3-642-41719-1. Springer-Verlag Berlin Heidelberg, 2014, p. 1, 37:1.* (Cited in pages 3 and 7.)
- Boeche, C., Siebert, A., Williams, M., de Jong, R. S., Steinmetz, M., Fulbright, J. P., Ruchti, G. R., Bienaymé, O., Bland-Hawthorn, J., Campbell, R., Freeman, K. C., Gibson, B. K., Gilmore, G., Grebel, E. K., Helmi, A., Munari, U., Navarro, J. F., Parker, Q. A., Reid, W., Seabroke, G. M., Siviero, A., Watson, F. G., Wyse, R. F. G., and Zwitter, T. (2011). The RAVE Catalog of Stellar Elemental Abundances: First Data Release. *AJ*, 142:193. (Cited in page 47.)

- Bournaud, F., Elmegreen, B. G., and Martig, M. (2009). The Thick Disks of Spiral Galaxies as Relics from Gas-rich, Turbulent, Clumpy Disks at High Redshift. *ApJ*, 707:L1–L5. (Cited in page 6.)
- Boyle, W. S. and Smith, G. E. (1970). Charge coupled semiconductor devices. *The Bell System Technical Journal*, 49(4):587–593. (Cited in page 16.)
- Brook, C., Richard, S., Kawata, D., Martel, H., and Gibson, B. K. (2007). Two Disk Components from a Gas-Rich Disk-Disk Merger. *ApJ*, 658:60–64. (Cited in page 6.)
- Brook, C. B., Kawata, D., Gibson, B. K., and Freeman, K. C. (2004). The Emergence of the Thick Disk in a Cold Dark Matter Universe. *ApJ*, 612:894–899. (Cited in page 6.)
- Brown, T. M., Christensen-Dalsgaard, J., Weibel-Mihalas, B., and Gilliland, R. L. (1994). The effectiveness of oscillation frequencies in constraining stellar model parameters. *ApJ*, 427:1013–1034. (Cited in page 6.)
- Butcher, H. (1987). Galactic chronology of thorium/neodymium. *Nature*, 330:704. (Cited in page 7.)
- Castelli, F. and Kurucz, R. L. (2003). New Grids of ATLAS9 Model Atmospheres. In Piskunov, N., Weiss, W. W., and Gray, D. F., editors, *Modelling of Stellar Atmospheres*, volume 210 of *IAU Symposium*, page A20. (Cited in page 47.)
- Crowther, P. (2012). Birth, life and death of massive stars. *Astronomy and Geophysics*, 53(4):4.30–4.36. (Cited in page 65.)
- da Silva, R., Porto de Mello, G. F., Milone, A. C., da Silva, L., Ribeiro, L. S., and Rocha-Pinto, H. J. (2012). Accurate and homogeneous abundance patterns in solar-type stars of the solar neighbourhood: a chemo-chronological analysis. *A&A*, 542:A84. (Cited in page 9.)
- de Laverny, P., Recio-Blanco, A., Worley, C. C., De Pascale, M., Hill, V., and Bijaoui, A. (2013). The AMBRE Project: Stellar Parameterisation of ESO Archived Spectra. *The Messenger*, 153:18–21. (Cited in pages 25 and 26.)
- de Laverny, P., Recio-Blanco, A., Worley, C. C., and Plez, B. (2012). The AMBRE project: A new synthetic grid of high-resolution FGKM stellar spectra. *A&A*, 544:A126. (Cited in pages 48, 50, 58, 82 and 83.)
- De Pascale, M., Worley, C. C., de Laverny, P., Recio-Blanco, A., Hill, V., and Bijaoui, A. (2014). The AMBRE project: Parameterisation of FGK-type stars from the ESO:HARPS archived spectra. *A&A*, 570:A68. (Cited in pages 26, 59 and 61.)

- Dekker, H., D’Odorico, S., Kaufer, A., Delabre, B., and Kotzlowski, H. (2000). Design, construction, and performance of UVES, the echelle spectrograph for the UT2 Kueyen Telescope at the ESO Paranal Observatory. In Iye, M. and Moorwood, A. F., editors, *Optical and IR Telescope Instrumentation and Detectors*, volume 4008 of Proc. SPIE, pages 534–545. (Cited in page 26.)
- Delgado Mena, E., Tsantaki, M., Adibekyan, V. Z., Sousa, S. G., Santos, N. C., González Hernández, J. I., and Israelian, G. (2017). Chemical abundances of 1111 FGK stars from the HARPS GTO planet search program. II. Cu, Zn, Sr, Y, Zr, Ba, Ce, Nd, and Eu. *A&A*, 606:A94. (Cited in pages 60, 62, 63 and 84.)
- Delgado Mena, E., Tsantaki, M., Zh. Adibekyan, V., Sousa, S. G., Santos, N. C., González Hernández, J. I., and Israelian, G. (2018). Abundance ratios ages of stellar populations in HARPS-GTO sample. In Recio-Blanco, A., de Laverny, P., Brown, A. G. A., and Prusti, T., editors, *IAU Symposium*, volume 330 of *IAU Symposium*, pages 156–159. (Cited in page 71.)
- Dotter, A., Chaboyer, B., Jevremović, D., Kostov, V., Baron, E., and Ferguson, J. W. (2008). The Dartmouth Stellar Evolution Database. *ApJS*, 178:89–101. (Cited in page 65.)
- Eggen, O. J., Lynden-Bell, D., and Sandage, A. R. (1962). Evidence from the motions of old stars that the Galaxy collapsed. *ApJ*, 136:748. (Cited in page 4.)
- Feltzing, S., Howes, L. M., McMillan, P. J., and Stonkutė, E. (2017). On the metallicity dependence of the [Y/Mg]-age relation for solar-type stars. *MNRAS*, 465:L109–L113. (Cited in page 9.)
- Freeman, K. and Bland-Hawthorn, J. (2002). The New Galaxy: Signatures of Its Formation. *ARA&A*, 40:487–537. (Cited in page 3.)
- Fuhrmann, K. (1998). Nearby stars of the Galactic disk and halo. *A&A*, 338:161–183. (Cited in page 5.)
- Gaia Collaboration, Babusiaux, C., van Leeuwen, F., Barstow, M. A., Jordi, C., Vallenari, A., Bossini, D., Bressan, A., Cantat-Gaudin, T., van Leeuwen, M., and et al. (2018a). Gaia Data Release 2: Observational Hertzsprung-Russell diagrams. *ArXiv e-prints*. (Cited in page 23.)
- Gaia Collaboration, Brown, A. G. A., Vallenari, A., Prusti, T., de Bruijne, J. H. J., Babusiaux, C., and Bailer-Jones, C. A. L. (2018b). Gaia Data Release 2. Summary of the contents and survey properties. *ArXiv e-prints*. (Cited in page 23.)
- Gaia Collaboration, Brown, A. G. A., Vallenari, A., Prusti, T., de Bruijne, J. H. J., Mignard, F., Drimmel, R., Babusiaux, C., Bailer-Jones, C. A. L., Bastian, U., and et al. (2016a).

- Gaia Data Release 1. Summary of the astrometric, photometric, and survey properties. *A&A*, 595:A2. (Cited in page 45.)
- Gaia Collaboration, Helmi, A., van Leeuwen, F., McMillan, P. J., Massari, D., Antoja, T., Robin, A., Lindegren, L., Bastian, U., and co-authors, . (2018c). Gaia Data Release 2: Kinematics of globular clusters and dwarf galaxies around the Milky Way. *ArXiv e-prints*. (Cited in page 23.)
- Gaia Collaboration, Katz, D., Antoja, T., Romero-Gómez, M., Drimmel, R., Reylé, C., Seabroke, G. M., Soubiran, C., Babusiaux, C., Di Matteo, P., Figueras, F., Poggio, E., Robin, A. C., Evans, D. W., and DPAC co-authors, . (2018d). Gaia Data Release 2: Mapping the Milky Way disc kinematics. *ArXiv e-prints*. (Cited in page 23.)
- Gaia Collaboration, Prusti, T., de Bruijne, J. H. J., Brown, A. G. A., Vallenari, A., Babusiaux, C., Bailer-Jones, C. A. L., Bastian, U., Biermann, M., Evans, D. W., and et al. (2016b). The Gaia mission. *A&A*, 595:A1. (Cited in page 45.)
- Gaia Collaboration, Spoto, F., Tanga, P., Mignard, F., Berthier, J., Carry, B., and Cellino, A. (2018e). Gaia Data Release 2: Observations of solar system objects. *ArXiv e-prints*. (Cited in page 23.)
- Gautschy, A. and Saio, H. (1995). Stellar Pulsations Across The HR Diagram: Part 1. *ARA&A*, 33:75–114. (Cited in page 6.)
- Gautschy, A. and Saio, H. (1996). Stellar Pulsations Across the HR Diagram: Part 2. *ARA&A*, 34:551–606. (Cited in page 6.)
- Gilmore, G. (2012). Evolution of the Milky Way: Some Open Issues for Gaia. In Aoki, W., Ishigaki, M., Suda, T., Tsujimoto, T., and Arimoto, N., editors, *Galactic Archaeology: Near-Field Cosmology and the Formation of the Milky Way*, volume 458 of *Astronomical Society of the Pacific Conference Series*, page 147. (Cited in page 24.)
- Gilmore, G., Randich, S., Asplund, M., Binney, J., Bonifacio, P., Drew, J., Feltzing, S., Ferguson, A., Jeffries, R., Micela, G., and et al. (2012). The Gaia-ESO Public Spectroscopic Survey. *The Messenger*, 147:25–31. (Cited in pages 24 and 82.)
- Gilmore, G. and Reid, N. (1983). New light on faint stars. III - Galactic structure towards the South Pole and the Galactic thick disc. *MNRAS*, 202:1025–1047. (Cited in page 5.)
- González Hernández, J. I. and Bonifacio, P. (2009). A new implementation of the infrared flux method using the 2MASS catalogue. *A&A*, 497:497–509. (Cited in page 27.)
- Gray, D. F. (2005). *The Observation and Analysis of Stellar Photospheres*. (Cited in pages 12 and 81.)

- Gray, R. O. (1999). SPECTRUM: A stellar spectral synthesis program. Astrophysics Source Code Library. (Cited in page 46.)
- Guiglion, G. (2015). *Étude du disque galactique par marquage chimique de ses populations stellaires*. PhD thesis, Université Nice Sophia Antipolis. (Cited in pages 45, 47, 48, 49, 58 and 82.)
- Guiglion, G., de Laverny, P., Recio-Blanco, A., and Worley, C. C. (2018). The AMBRE Project: r-process element abundances in the Milky Way thin and thick discs. In Recio-Blanco, A., de Laverny, P., Brown, A. G. A., and Prusti, T., editors, *IAU Symposium*, volume 330 of *IAU Symposium*, pages 216–217. (Cited in page 58.)
- Guiglion, G., de Laverny, P., Recio-Blanco, A., Worley, C. C., De Pascale, M., Masseron, T., Prantzos, N., and Mikolaitis, Š. (2016). The AMBRE project: Constraining the lithium evolution in the Milky Way. *A&A*, 595:A18. (Cited in pages 45, 47 and 59.)
- Gustafsson, B., Edvardsson, B., Eriksson, K., Jørgensen, U. G., Nordlund, Å., and Plez, B. (2008). A grid of MARCS model atmospheres for late-type stars. I. Methods and general properties. *A&A*, 486:951–970. (Cited in pages 13, 26, 46, 47 and 57.)
- Guzik, J. A., Kaye, A. B., Bradley, P. A., Cox, A. N., and Neuforge, C. (2000). Driving the Gravity-Mode Pulsations in γ Doradus Variables. *ApJ*, 542:L57–L60. (Cited in page 3.)
- Hannaford, P., Lowe, R. M., Grevesse, N., Biemont, E., and Whaling, W. (1982). Oscillator strengths for Y I and Y II and the solar abundance of yttrium. *ApJ*, 261:736–746. (Cited in page 58.)
- Hayden, M. R., Recio-Blanco, A., de Laverny, P., Mikolaitis, S., Guiglion, G., Hill, V., Gilmore, G., Randich, S., Bayo, A., Bensby, T., Bergemann, M., Bragaglia, A., Casey, A., Costado, M., Feltzing, S., Franciosini, E., Hourihane, A., Jofre, P., Koposov, S., Kor-dopatis, G., Lanzafame, A., Lardo, C., Lewis, J., Lind, K., Magrini, L., Monaco, L., Morbidelli, L., Pancino, E., Sacco, G., Stonkute, E., Worley, C. C., and Zwitter, T. (2017). The Gaia-ESO Survey: Churning through the Milky Way. *ArXiv e-prints*. (Cited in pages 9, 68 and 71.)
- Haywood, M., Di Matteo, P., Lehnert, M. D., Katz, D., and Gómez, A. (2013). The age structure of stellar populations in the solar vicinity. Clues of a two-phase formation history of the Milky Way disk. *A&A*, 560:A109. (Cited in pages 9, 68 and 71.)
- Haywood, M., Di Matteo, P., Snaith, O., and Lehnert, M. D. (2015). Clues to the formation of the Milky Way’s thick disk. *A&A*, 579:A5. (Cited in pages 5 and 81.)
- Hill, V., Plez, B., Cayrel, R., Beers, T. C., Nordström, B., Andersen, J., Spite, M., Spite, F., Barbuy, B., Bonifacio, P., Depagne, E., François, P., and Primas, F. (2002). First stars.

- I. The extreme r-element rich, iron-poor halo giant CS 31082-001. Implications for the r-process site(s) and radioactive cosmochronology. *A&A*, 387:560–579. (Cited in page 7.)
- Høg, E., Fabricius, C., Makarov, V. V., Urban, S., Corbin, T., Wycoff, G., Bastian, U., Schwekendiek, P., and Wicenec, A. (2000). The Tycho-2 catalogue of the 2.5 million brightest stars. *A&A*, 355:L27–L30. (Cited in pages 21 and 43.)
- Houdek, G., Balmforth, N. J., Christensen-Dalsgaard, J., and Gough, D. O. (1999). Amplitudes of stochastically excited oscillations in main-sequence stars. *A&A*, 351:582–596. (Cited in page 6.)
- Hoyle, F. and Fowler, W. A. (1960). Nucleosynthesis in Supernovae. *ApJ*, 132:565. (Cited in pages 3 and 7.)
- Iben, Jr., I. (1965). Stellar Evolution. II. The Evolution of a $3 M_{\odot}$ Star from the Main Sequence Through Core Helium Burning. *ApJ*, 142:1447. (Cited in page 9.)
- Jones, B. J. T. and Wyse, R. F. G. (1983). The evolution of adiabatic fluctuations through the period of recombination. *MNRAS*, 205:983–1007. (Cited in page 6.)
- Jørgensen, B. R. and Lindegren, L. (2005). Determination of stellar ages from isochrones: Bayesian estimation versus isochrone fitting. *A&A*, 436:127–143. (Cited in pages 7, 8, 66 and 81.)
- Jurić, M., Ivezić, Ž., Brooks, A., Lupton, R. H., Schlegel, D., Finkbeiner, D., Padmanabhan, N., Bond, N., Sesar, B., Rockosi, C. M., Knapp, G. R., Gunn, J. E., Sumi, T., Schneider, D. P., Barentine, J. C., Brewington, H. J., Brinkmann, J., Fukugita, M., Harvanek, M., Kleinman, S. J., Krzesinski, J., Long, D., Neilsen, Jr., E. H., Nitta, A., Snedden, S. A., and York, D. G. (2008). The Milky Way Tomography with SDSS. I. Stellar Number Density Distribution. *ApJ*, 673:864–914. (Cited in page 5.)
- Katz, D., Munari, U., Cropper, M., Zwitter, T., Thévenin, F., David, M., Viala, Y., Crifo, F., Gomboc, A., Royer, F., Arenou, F., Marrese, P., Sordo, R., Wilkinson, M., Vallenari, A., Turon, C., Helmi, A., Bono, G., Perryman, M., Gómez, A., Tomasella, L., Boschi, F., Morin, D., Haywood, M., Soubiran, C., Castelli, F., Bijaoui, A., Bertelli, G., Prsa, A., Mignot, S., Sellier, A., Baylac, M.-O., Lebreton, Y., Jauregi, U., Siviero, A., Bingham, R., Chemla, F., Coker, J., Dibbens, T., Hancock, B., Holland, A., Horville, D., Huet, J.-M., Laporte, P., Melse, T., Sayède, F., Stevenson, T.-J., Vola, P., Walton, D., and Winter, B. (2004). Spectroscopic survey of the Galaxy with Gaia- I. Design and performance of the Radial Velocity Spectrometer. *MNRAS*, 354:1223–1238. (Cited in page 17.)
- Kaufer, A., Stahl, O., Tubbesing, S., Nørregaard, P., Avila, G., Francois, P., Pasquini, L., and Pizzella, A. (1999). Commissioning FEROS, the new high-resolution spectrograph at La-Silla. *The Messenger*, 95:8–12. (Cited in page 26.)

- Kordopatis, G., Recio-Blanco, A., de Laverny, P., Gilmore, G., Hill, V., Wyse, R. F. G., Helmi, A., Bijaoui, A., Zoccali, M., and Bienaymé, O. (2011). A spectroscopic survey of thick disc stars outside the solar neighbourhood. *A&A*, 535:A107. (Cited in page 4.)
- Kormendy, J. and Kennicutt, Jr., R. C. (2004). Secular Evolution and the Formation of Pseudobulges in Disk Galaxies. *ARA&A*, 42:603–683. (Cited in page 4.)
- Kurucz, R. L. (2005). ATLAS12, SYNTHE, ATLAS9, WIDTH9, et cetera. *Memorie della Societa Astronomica Italiana Supplementi*, 8:14. (Cited in page 47.)
- Lindegren, L., Lammers, U., Bastian, U., Hernández, J., Klioner, S., Hobbs, D., Bombrun, A., Michalik, D., Ramos-Lerate, M., Butkevich, A., Comoretto, G., Joliet, E., Holl, B., Hutton, A., Parsons, P., Steidelmüller, H., Abbas, U., Altmann, M., Andrei, A., Anton, S., Bach, N., Barache, C., Becciani, U., Berthier, J., Bianchi, L., Biermann, M., Bouquillon, S., Bourda, G., Brüsemeister, T., Bucciarelli, B., Busonero, D., Carlucci, T., Castañeda, J., Charlot, P., Clotet, M., Crosta, M., Davidson, M., de Felice, F., Drimmel, R., Fabricius, C., Fienga, A., Figueras, F., Fraile, E., Gai, M., Garralda, N., Geyer, R., González-Vidal, J. J., Guerra, R., Hambly, N. C., Hauser, M., Jordan, S., Lattanzi, M. G., Lenhardt, H., Liao, S., Löffler, W., McMillan, P. J., Mignard, F., Mora, A., Morbidelli, R., Portell, J., Riva, A., Sarasso, M., Serraller, I., Siddiqui, H., Smart, R., Spagna, A., Stampa, U., Steele, I., Taris, F., Torra, J., van Reeven, W., Vecchiato, A., Zschocke, S., de Bruijne, J., Gracia, G., Raison, F., Lister, T., Marchant, J., Messineo, R., Soffel, M., Osorio, J., de Torres, A., and O’Mullane, W. (2016). Gaia Data Release 1. Astrometry: one billion positions, two million proper motions and parallaxes. *A&A*, 595:A4. (Cited in pages 21 and 43.)
- Loebman, S. R., Roškar, R., Debattista, V. P., Ivezić, Ž., Quinn, T. R., and Wadsley, J. (2011). The Genesis of the Milky Way’s Thick Disk Via Stellar Migration. *ApJ*, 737:8. (Cited in page 6.)
- Luri, X., Torra, J., and Figueras, F. (1992). The proximity parameter. *A&A*, 259:382–385. (Cited in page 3.)
- Martig, M., Fouesneau, M., Rix, H.-W., Ness, M., Mészáros, S., García-Hernández, D. A., Pinsonneault, M., Serenelli, A., Silva Aguirre, V., and Zamora, O. (2016). Red giant masses and ages derived from carbon and nitrogen abundances. *MNRAS*, 456:3655–3670. (Cited in page 9.)
- Masseron, T. and Gilmore, G. (2015). Carbon, nitrogen and α -element abundances determine the formation sequence of the Galactic thick and thin discs. *MNRAS*, 453:1855–1866. (Cited in pages 5 and 9.)
- Mayor, M., Pepe, F., Queloz, D., Bouchy, F., Rupprecht, G., Lo Curto, G., Avila, G., Benz, W., Bertaux, J.-L., Bonfils, X., Dall, T., Dekker, H., Delabre, B., Eckert, W., Fleury, M., Gilliotte, A., Gojak, D., Guzman, J. C., Kohler, D., Lizon, J.-L., Longinotti, A., Lovis,

- C., Megevand, D., Pasquini, L., Reyes, J., Sivan, J.-P., Sosnowska, D., Soto, R., Udry, S., van Kesteren, A., Weber, L., and Weilenmann, U. (2003). Setting New Standards with HARPS. *The Messenger*, 114:20–24. (Cited in page 26.)
- McWilliam, A., Wallerstein, G., and Mottini, M. (2013). Chemistry of the Sagittarius Dwarf Galaxy: A Top-light Initial Mass Function, Outflows, and the R-process. *ApJ*, 778:149. (Cited in page 58.)
- Michalik, D., Lindegren, L., and Hobbs, D. (2015). The Tycho-Gaia astrometric solution . How to get 2.5 million parallaxes with less than one year of Gaia data. *A&A*, 574:A115. (Cited in pages 21, 26 and 43.)
- Michalik, D., Lindegren, L., Hobbs, D., and Lammers, U. (2014). Joint astrometric solution of HIPPARCOS and Gaia. A recipe for the Hundred Thousand Proper Motions project. *A&A*, 571:A85. (Cited in page 21.)
- Mignard, F. (2009). Space Astrometry Science with Gaia. In *American Astronomical Society Meeting Abstracts #214*, volume 214 of *American Astronomical Society Meeting Abstracts*, page 742. (Cited in page 21.)
- Mignard, F., Klioner, S., Lindegren, L., Hernandez, J., Bastian, U., and Bombrun, A. (2018). Gaia Data Release 2: The Celestial reference frame (Gaia-CRF2). *ArXiv e-prints*. (Cited in page 23.)
- Mikolaitis, Š., de Laverny, P., Recio-Blanco, A., Hill, V., Worley, C. C., and de Pascale, M. (2017). The AMBRE project: Iron-peak elements in the solar neighbourhood. *A&A*, 600:A22. (Cited in pages 58, 62, 63, 65, 67 and 84.)
- Mikolaitis, Š., Hill, V., Recio-Blanco, A., de Laverny, P., Allende Prieto, C., Kordopatis, G., Tautvaišiene, G., Romano, D., Gilmore, G., Randich, S., Feltzing, S., Micela, G., Vallenari, A., Alfaro, E. J., Bensby, T., Bragaglia, A., Flaccomio, E., Lanzafame, A. C., Pancino, E., Smiljanic, R., Bergemann, M., Carraro, G., Costado, M. T., Damiani, F., Hourihane, A., Jofré, P., Lardo, C., Magrini, L., Maiorca, E., Morbidelli, L., Sbordone, L., Sousa, S. G., Worley, C. C., and Zaggia, S. (2014). The Gaia-ESO Survey: the chemical structure of the Galactic discs from the first internal data release. *A&A*, 572:A33. (Cited in pages 47 and 62.)
- Minchev, I. and Famaey, B. (2010). A New Mechanism for Radial Migration in Galactic Disks: Spiral-Bar Resonance Overlap. *ApJ*, 722:112–121. (Cited in page 6.)
- Minchev, I., Famaey, B., Quillen, A. C., Dehnen, W., Martig, M., and Siebert, A. (2012). Radial migration does little for Galactic disc thickening. *A&A*, 548:A127. (Cited in page 6.)

- Mucciarelli, A., Pancino, E., Lovisi, L., Ferraro, F. R., and Lapenna, E. (2013). GALA: An Automatic Tool for the Abundance Analysis of Stellar Spectra. *ApJ*, 766:78. (Cited in page 47.)
- Nissen, P. E. (2015). High-precision abundances of elements in solar twin stars. Trends with stellar age and elemental condensation temperature. *A&A*, 579:A52. (Cited in pages 9, 68, 69, 72, 74 and 85.)
- Perryman, M. A. C., de Boer, K. S., Gilmore, G., Høg, E., Lattanzi, M. G., Lindegren, L., Luri, X., Mignard, F., Pace, O., and de Zeeuw, P. T. (2001). GAIA: Composition, formation and evolution of the Galaxy. *A&A*, 369:339–363. (Cited in page 15.)
- Perryman, M. A. C., Guyenne, T. D., Høg, E., Jaschek, C., and Lacroute, P., editors (1982). *The scientific aspects of the HIPPARCOS space astrometry mission*, volume 177 of *ESA Special Publication*. (Cited in page 21.)
- Pesnell, W. D. (1987). A new driving mechanism for stellar pulsations. *ApJ*, 314:598–604. (Cited in pages 3 and 6.)
- Piskunov, N. E. (1992). SYNTH - a code for rapid spectral synthesis. In Glagolevskij, Y. V. and Romanyuk, I. I., editors, *Physics and Evolution of Stars: Stellar Magnetism*, page 92. (Cited in page 46.)
- Plez, B. (2012). Turbospectrum: Code for spectral synthesis. *Astrophysics Source Code Library*. (Cited in pages 46 and 47.)
- Posbic, H., Katz, D., Caffau, E., Bonifacio, P., Gómez, A., Sbordone, L., and Arenou, F. (2012). SPADES: a stellar parameters determination software. *A&A*, 544:A154. (Cited in page 47.)
- Quinn, P. J., Hernquist, L., and Fullagar, D. P. (1993). Heating of galactic disks by mergers. *ApJ*, 403:74–93. (Cited in page 6.)
- Recio-Blanco, A., Bijaoui, A., and de Laverny, P. (2006). Automated derivation of stellar atmospheric parameters and chemical abundances: the MATISSE algorithm. *MNRAS*, 370:141–150. (Cited in pages 15, 26, 47 and 59.)
- Recio-Blanco, A., de Laverny, P., Allende Prieto, C., Fustes, D., Manteiga, M., Arcay, B., Bijaoui, A., Dafonte, C., Ordenovic, C., and Ordoñez Blanco, D. (2016). Stellar parametrization from Gaia RVS spectra. *A&A*, 585:A93. (Cited in pages 20, 45 and 59.)
- Recio-Blanco, A., de Laverny, P., Kordopatis, G., Helmi, A., Hill, V., Gilmore, G., Wyse, R., Adibekyan, V., Randich, S., Asplund, M., Feltzing, S., Jeffries, R., Micela, G., Vallenari, A., Alfaro, E., Allende Prieto, C., Bensby, T., Bragaglia, A., Flaccomio, E., Koposov, S. E., Korn, A., Lanzafame, A., Pancino, E., Smiljanic, R., Jackson, R., Lewis, J., Magrini,

- L., Morbidelli, L., Prisinzano, L., Sacco, G., Worley, C. C., Hourihane, A., Bergemann, M., Costado, M. T., Heiter, U., Joffe, P., Lardo, C., Lind, K., and Maiorca, E. (2014). The Gaia-ESO Survey: the Galactic thick to thin disc transition. *A&A*, 567:A5. (Cited in pages 5 and 9.)
- Rix, H.-W. and Bovy, J. (2013). The Milky Way's stellar disk. Mapping and modeling the Galactic disk. *A&A Rev.*, 21:61. (Cited in page 73.)
- Salaris, M. and Cassisi, S. (2005). *Evolution of Stars and Stellar Populations*. (Cited in page 9.)
- Samadi, R. and Goupil, M.-J. (2001). Excitation of stellar p-modes by turbulent convection. I. Theoretical formulation. *A&A*, 370:136–146. (Cited in page 6.)
- Samadi, R., Goupil, M.-J., and Lebreton, Y. (2001). Excitation of stellar p-modes by turbulent convection. II. The Sun. *A&A*, 370:147–156. (Cited in page 6.)
- Sbordone, L., Caffau, E., Bonifacio, P., and Duffau, S. (2014). MyGIsFOS: an automated code for parameter determination and detailed abundance analysis in cool stars. *A&A*, 564:A109. (Cited in page 47.)
- Schaltenbrand, R. A. (1974). Three-colour photometry of SA 94 in the RGU system. *A&AS*, 18:27. (Cited in pages 3 and 7.)
- Schönrich, R. and Binney, J. (2009). Chemical evolution with radial mixing. *MNRAS*, 396:203–222. (Cited in page 6.)
- Searle, L. and Zinn, R. (1978). Compositions of halo clusters and the formation of the galactic halo. *ApJ*, 225:357–379. (Cited in page 4.)
- Skrutskie, M. F., Cutri, R. M., Stiening, R., Weinberg, M. D., Schneider, S., Carpenter, J. M., Beichman, C., Capps, R., Chester, T., Elias, J., Huchra, J., Liebert, J., Lonsdale, C., Monet, D. G., Price, S., Seitzer, P., Jarrett, T., Kirkpatrick, J. D., Gizis, J. E., Howard, E., Evans, T., Fowler, J., Fullmer, L., Hurt, R., Light, R., Kopan, E. L., Marsh, K. A., McCallon, H. L., Tam, R., Van Dyk, S., and Wheelock, S. (2006). The Two Micron All Sky Survey (2MASS). *AJ*, 131:1163–1183. (Cited in page 26.)
- Slumstrup, D., Grundahl, F., Brogaard, K., Thygesen, A. O., Nissen, P. E., Jessen-Hansen, J., Van Eylen, V., and Pedersen, M. G. (2017). The $[Y/Mg]$ clock works for evolved solar metallicity stars. *A&A*, 604:L8. (Cited in page 9.)
- Snedden, C. A. (1973). *Carbon and Nitrogen Abundances in Metal-Poor Stars*. PhD thesis, THE UNIVERSITY OF TEXAS AT AUSTIN. (Cited in pages 46 and 47.)

- Sousa, S. G., Santos, N. C., Israelian, G., Mayor, M., and Monteiro, M. J. P. F. G. (2007). A new code for automatic determination of equivalent widths: Automatic Routine for line Equivalent widths in stellar Spectra (ARES). *A&A*, 469:783–791. (Cited in page 47.)
- Spina, L., Meléndez, J., Karakas, A. I., Ramírez, I., Monroe, T. R., Asplund, M., and Yong, D. (2016). Nucleosynthetic history of elements in the Galactic disk. [X/Fe]-age relations from high-precision spectroscopy. *A&A*, 593:A125. (Cited in page 9.)
- Statler, T. S. (1988). Orbital decay in aspherical galaxies. I - Oblate systems. *ApJ*, 331:71–101. (Cited in page 6.)
- Stetson, P. B. and Pancino, E. (2008). DAOSPEC: An Automatic Code for Measuring Equivalent Widths in High-Resolution Stellar Spectra. *PASP*, 120:1332. (Cited in page 47.)
- Toomre, A. (1977). Mergers and Some Consequences. In Tinsley, B. M. and Larson, D. Campbell, R. B. G., editors, *Evolution of Galaxies and Stellar Populations*, page 401. (Cited in page 4.)
- Tucci Maia, M., Ramírez, I., Meléndez, J., Bedell, M., Bean, J. L., and Asplund, M. (2016). The Solar Twin Planet Search. III. The [Y/Mg] clock: estimating stellar ages of solar-type stars. *A&A*, 590:A32. (Cited in pages 9, 68, 72 and 74.)
- Valenti, J. A. and Piskunov, N. (1996). Spectroscopy made easy: A new tool for fitting observations with synthetic spectra. *A&AS*, 118:595–603. (Cited in page 46.)
- Valls-Gabaud, D. (2014). Bayesian isochrone fitting and stellar ages. In *EAS Publications Series*, volume 65 of *EAS Publications Series*, pages 225–265. (Cited in pages 3 and 7.)
- Van der Swaelmen, M., Hill, V., Primas, F., and Cole, A. A. (2013). Chemical abundances in LMC stellar populations. II. The bar sample. *A&A*, 560:A44. (Cited in page 47.)
- van Leeuwen, F. (2007). Validation of the new Hipparcos reduction. *A&A*, 474:653–664. (Cited in page 21.)
- Villalobos, Á. and Helmi, A. (2008). Simulations of minor mergers - I. General properties of thick discs. *MNRAS*, 391:1806–1827. (Cited in page 6.)
- W. Marquardt, D. (1963). An algorithm for least square estimation of non-linear parameters. 11:431–441. (Cited in page 46.)
- Wilkinson, M. I., Vallenari, A., Turon, C., Munari, U., Katz, D., Bono, G., Cropper, M., Helmi, A., Robichon, N., Thévenin, F., Vidrih, S., Zwitter, T., Arenou, F., Baylac, M.-O., Bertelli, G., Bijaoui, A., Boschi, F., Castelli, F., Crifo, F., David, M., Gomboc, A., Gómez, A., Haywood, M., Jauregi, U., de Laverny, P., Lebreton, Y., Marrese, P., Marsh, T., Mignot, S., Morin, D., Pasetto, S., Perryman, M., Prša, A., Recio-Blanco, A., Royer,

- F., Sellier, A., Siviero, A., Sordo, R., Soubiran, C., Tomasella, L., and Viala, Y. (2005). Spectroscopic survey of the Galaxy with Gaia- II. The expected science yield from the Radial Velocity Spectrometer. *MNRAS*, 359:1306–1335. (Cited in pages 15 and 17.)
- Worley, C. C., de Laverny, P., Recio-Blanco, A., Hill, V., and Bijaoui, A. (2016). The AMBRE Project: Stellar parameterisation of the ESO:UVES archived spectra. *A&A*, 591:A81. (Cited in page 26.)
- Worley, C. C., de Laverny, P., Recio-Blanco, A., Hill, V., Bijaoui, A., and Ordenovic, C. (2012). The AMBRE Project: Stellar parameterisation of the ESO:FEROS archived spectra. *A&A*, 542:A48. (Cited in page 26.)
- Yoshii, Y. (1982). Density Distribution of Faint Stars in the Direction of the North Galactic Pole. *PASJ*, 34:365. (Cited in page 5.)